High Resolution Characterisation of Gold Nanoparticle Coronae by Differential Centrifugal Sedimentation

Thesis submitted in accordance with the requirements of the University of Liverpool for the degree of Doctor in Philosophy

By
Adam Michael Davidson

October 2017

Dedicated in memoriam to

David Keith Rayner

1936 - 2017

A loving Grandfather,

An avid believer in science,

And a stalwart advocate of education.

Acknowledgements

First and foremost, I would like to thank my supervisors Prof Mathias Brust and Dr Martin Volk for the opportunity and their continued help and assistance throughout the entire project. A special thank you goes to every member of the Copenhagen University team that helped with the plant work during my time there, particularly Prof Poul-Erik Jensen, Dr Kasper Nørregard, Dr Agnieszka Zygadlo Nielsen and Dr Silas Busck Mellor for their help and continued friendship. I would also like to specifically thank Dr Volk for his assistance and hard work on the analysis of the BSA data and his help with making our paper ready for publication as well as repeated help with analysis and mentoring throughout the years.

My thanks go to every member of the Brust group, past and present, for their advice and practical and emotional support during my entire PhD. Special thanks to: Dr Casper Kunstmann for his refereeing, continued motivation and help with editing this thesis; Dr Domagoj Belić and Alison Beckett for their help and mentoring with respect to all things EM based; Dr Samantha Chadwick, for all those years of correcting my 'wheres' and being a brilliant friend and mentor. Special thanks also to my friends and colleagues, Mike Craven, Faye Hern, Chris Thomas, Bob Smith, Malte Strozyk, Alex Hill and Stephen Danks, for being my emotional support and reminding me that life is good in the difficult moments.

Thanks to my family, the Davidsons, Rayners, Hatchs and Winstanleys, for all the food, love, consolation, and support. Particularly to my grandfather for instilling in me a love of all things science.

Finally, to my loving wife, thank you for being there every evening (on some days, what little there was) to cheer me up and enjoying life with me; and also for helping to proof-read my thesis despite having just written your own.

To the neighbours, thanks for being patient with the erratic hours and the garden/jungle.

Abstract

The University of Liverpool

Doctor of Philiosophy

High Resolution Characterisation of Gold Nanoparticle Coronae by Differential Centrifugal Sedimentation

Adam Michael Davidson

Differential Centrifugal Sedimentation is a form of Analytical Ultracentrifugation that determines the size of a sample by measuring the time taken to sediment through a density gradient using a modified version of the Stokes law. This technique has been used to measure the ligand shell size of various ligands on the surface of gold nanoparticles.

This project utilises this technique to measure a variety of coronae that form around spherical gold nanoparticles: the electrochemical double layer; peptide coating packing densities; the protein corona and the formation of nanoparticle-photosystem hybrids. Preliminary findings for the electrochemical double layer indicate this process can be observed, but requires quantitative analysis and complementary techniques. We also show that the technique can observe changes in packing density as subtle as 0.07nm, which we verified using Fourier Transform Infra-Red spectroscopy.

We demonstrated that the technique can be used to accurately follow the formation of a chemisorbed protein corona around differently capped nanoparticles. Also, with addition of protein to the density gradient, to maintain the equilibrium of the sample, the physisorbed corona can also be observed. This is information not readily obtainable using other established techniques, without more complex setups or addition of probes to the particles.

Due to the complex nature of the nanoparticle-photosystem hybrids created in this project, the differential centrifugal sedimentation technique could only provide qualitative information about the systems. However, using this information and a variety of other techniques such as; UV-Vis spectroscopy and a range of electron microscopies, the systems were characterised further.

Preliminary work using the afore mentioned systems attempted to create photo-electrodes, by coating gold slides with these hybrids, as well as functionalisation of nanoparticles with a chloroplast specific transit peptide for the internalisation of gold nanoparticles into isolated chloroplasts. The transit peptide was successfully purified and was used to functionalise stable nanoparticle dispersions. Initial findings suggest the transit peptide can be used to localise the particles to the chloroplast import machinery, but no import was observed.

In this project we demonstrate the versatility of the differential centrifugal sedimentation technique both as a stand-alone or complementary method.

Table of Contents

Acknowledgements **3**

Abstract **4**

Table of Contents **5**

Abbreviations **10**

Chapter 1 ..... **12**

1 - Introduction **12**

1.1 – General Principles 14

1.1.2 – Synthesis, Stabilisation and Functionalisation of Gold Nanoparticles 14

1.1.3 – Electrochemical Double Layer 20

1.1.4 – Protein 'Corona' 25

1.2 – Characterisation Methods 29

1.2.1 – UV-Vis Spectroscopy 29

1.2.2 - Dynamic Light Scattering 33

1.2.3 - Differential Centrifugal Sedimentation 34

1.2.4 - Fourier Transform Infra-Red Spectroscopy 45

1.2.5 - Electron Microscopies 50

1.3 – Biological Principles 53

1.3.1 – Photosystem 1 53

1.3.2 – Plant Cell Physiology and Molecular Import 56

Chapter 2..... 60

2 – Methods: 60

2.1 - Chemicals for Nanoparticle Synthesis..... 60

2.1.1 – Synthesis of 13-15 nm Spherical Citrate Stabilised Gold Nanoparticle 61

2.1.2 – Synthesis of 9-11 nm Spherical Citrate Stabilised Gold Nanoparticle 62

2.1.3 – Synthesis ~5 nm Spherical Citrate and Tannic Acid Stabilised Gold Nanoparticle..... 62

2.2 – Chemicals for Nanoparticle Functionalisation 63

2.2.1 – Gold Nanoparticle Functionalisation with PEG's 64

2.2.2 – Gold Nanoparticle Functionalisation with CALNN and CALNN-TAT Peptides 65

2.2.3 – Gold Nanoparticle Functionalisation with Chloroplast Transit Peptide 66

2.2.4 – Gold Nanoparticle Functionalisation with Mercapto-phenol..... 67

2.2.5 – Gold Nanoparticle Functionalisation with Photosystem 1 68

2.3 – UV-Vis Measurements..... 68

2.4 - Centrifugal Particle Sizer Standard Setup 69

2.4.1 – Centrifugal Particle Sizer Electrolyte Gradient..... 72

2.4.2 – Centrifugal Particle Sizer Protein Gradient 73

2.5 – Electron Microscopy..... 73

2.5.1 – Nanoparticle Preparation for Electron Microscopy..... 74

2.5.2 – Negative staining of sample for Transmission Electron Microscopy 74

2.5.3 – Fixation and staining of Chloroplast samples for Transmission Electron Microscopy 75

2.5.4 – Resin block cutting and preparation for Transmission Electron Microscopy 78

2.5.5 – Sample preparation for Cryo - TEM 79

2.6 - Fourier Transform Infra-Red sample preparation and measurement..... 79

2.7.1 - Solid Medium Cell Culture Plates..... 81

2.7.2 - Transit Peptide Transfection into *Escherichia Coli* 82

2.8.1 - Transit Peptide Expression..... 84

2.8.2 - Transit Peptide Purification 86

2.9 - Bradford Assay 87

2.10 - Gel Electrophoresis 88

2.11 - Western Blot 89

2.12 - *Pisum Sativum* Growth and Chloroplast Extraction and Import..... 91

2.13 - Gold Slide Coating with Particles and Photosystem 1 95

Chapter 3..... 96

3 – Differential Centrifugal Analysis of Electrochemical Double Layer 97

Chapter 4.....113

4 – Differential Centrifugal Analysis of Protein "Corona" 113

4.1 – DCS Measurement of the Packing Density of a Short Chain Peptide Bound to a GNPs Surface 114

4.2 – DCS Measurement of Protein Corona Formation of the Capping Layer of GNPs 119

Chapter 5 141

5.1 – Gold Nanoparticle – Photosystem 1 Hybrids 142

5.2 – Gold Nanoparticles for Import into Chloroplasts 156

5.2.1 – Production and Purification of Transit Peptide 156

5.2.2 – Chloroplast Extraction and Nanoparticle Import 165

6 – Conclusions and Future Work 175

6.1 – DCS as a Method for Analysing the EDL 175

6.2.1 – DCS as a Method for Analysing Ligand Capping Densities 176

6.2.2 – DCS as a Method for Analysing Protein Corona Formation 176

6.3.1 – DCS as a Method for Analysing more Complex Protein Systems & GNP-PS1 hybrids 177

6.3.2 – GNPs Import into Chloroplasts 178

6.4 – Final Conclusions 178

References 180

Appendix 191

Appendix 1 – List of Figures 191

Appendix 2 – List of Equations 200

Appendix 3 – List of Tables..... 201

Abbreviations

DCS – Differential Centrifugal Sedimentation

GNPs – Gold Nanoparticles

EDL – Electrochemical Double Layer

IHP – Inner Helmholtz Plane

OHP – Outer Helmholtz Plane

DL – Debye Length

BSA – Bovine Serum Albumin

UV-Vis – Ultra Violet – Visible

SPR – Surface Plasmon Resonance

DLS – Dynamic Light Scattering

TEM – Transmission Electron Microscopy

SEM – Scanning Electron Microscopy

AUC – Analytical Ultra-centrifugation

PVC – Poly vinyl chloride

PS1 – Photosystem 1

PEG – Polyethylene Glycol

FT-IR – Fourier Transform Infra-Red

MQ- Milli-Q

LB – Lysogeny Broth

PCR – Polymer Chain Reaction

dNTPs – Deoxy Nucleotide Triphosphates

EDTA – Ethylenediaminetetraacetic aicd

TAE - Tris base, Acetic Acid and EDTA

OD – Optical Density

IPTG – Isopropyl β-D-1- Thiogalactopyranoside

GMO – Genetically Modified Organism

DTT – Dithiothreitol

PBS – Phosphate Buffered Saline

MES – 2-N-Morpholino Ethanesulfonic acid

SDS – Sodium Dodecyl (lauryl) Sulfate

TGS – Tris Glycine SDS

MgATP – Magnesium Adenosine Triphosphate

HS – Hepes and Sorbitol

Chapter 1

1 - Introduction

The main focus of this thesis was to explore the capabilities of a technique called differential centrifugal sedimentation (DCS) to investigate possible surface phenomenon that form on particles when exposed to biological media; such as, proteins and electrolytes found in the cells or their culture fluids. The secondary focus of this thesis was to create and characterise metal-bio hybrids of gold nanoparticles with a mutated version of photosystem one, isolated for binding from (*Synechococcus sp. PCC 7002*)[1], and also to determine if these particles could be imported into chloroplasts as a proof of concept for a long-term aim of setting up light harnessing systems in situ for renewable energy.

This chapter will introduce the background to the different effects that we will attempted to measure using DCS; a brief discussion of characterisation techniques used and a discussion of some of their pros and cons; and finally, a brief introduction to plant science, chloroplast and the photosynthetic apparatus; that are required to understand this body of work.

In the past few decades, gold nanoparticles (GNPs) have become more common in a wide variety of biological applications. This is most likely due to their lack of cytotoxicity and ease of functionalisation with a huge array of functionalities: from antibodies for immuno-gold assays and biomarkers tests; to biological tracers and

components that promote cellular uptake for cancer therapies[2–8]. With this increasing interest, the understanding of GNPs mechanisms and exact surface reactivity once exposed to biological systems, has come in to question, particularly where cellular uptake is concerned.

It is well established that once introduced into biological media, on the GNP surface a layer forms consisting of, either covalently or weak intramolecular bound proteins that can possibly mask or entirely change the surface chemistry of the particles[9–13]. This layer is commonly known as the protein 'corona'. This effect is poorly understood and difficult to observe in situ/ or in equilibrium conditions due to its dynamic nature. The unknown role of this protein 'corona' in functions such as cellular uptake and the GNPs activity once internalised, makes it a 'hotly' debated topic within the field[14–19]. Another effect that is better understood but difficult to observe directly as a physical measurement, is the electrochemical double layer (EDL)[20]. This EDL forms when charged end groups come into contact with an electrolyte, which are widely abundant in biological media.

1.1 – General Principles

1.1.2 – Synthesis, Stabilisation and Functionalisation of Gold Nanoparticles

The properties of nanomaterials stem from their larger ratio of surface atoms to bulk. There is a wide range of evidence from the fields of surface science and electrochemistry showing the importance and unique chemistry of surface, edge and defect atoms[21]. These atoms have an incomplete electron configuration, leading them to be highly reactive, so under normal circumstances they do not exist for very long due to the large entropic drive to limit the number of atoms in a system with an incomplete electron configuration. This entropic drive is usually resolved by the smaller nuclei merging to form larger and larger particles, until they become large enough to remain stable and essentially resemble the properties of bulk gold, this process is termed aggregation (Figure 1)[22].

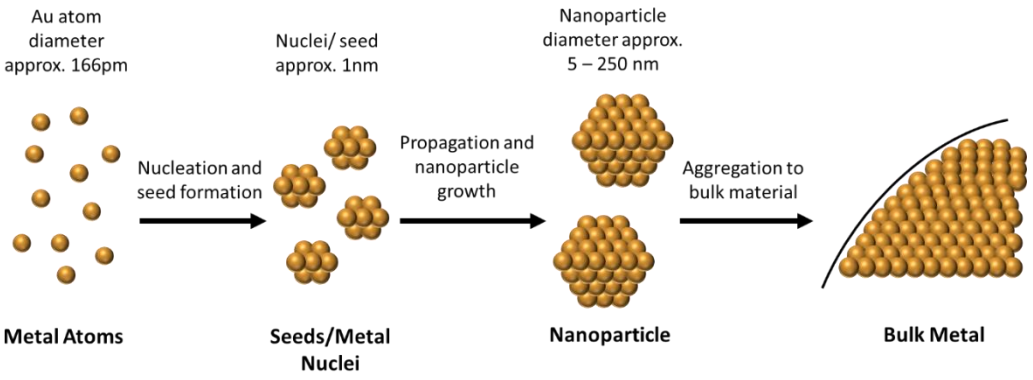

Figure 1: Schematic of aggregation of atoms into bulk material to limit the number of high energy surface atoms[22].

To enable nanoparticles to maintain their small size and therefore their properties, this aggregation process must be prevented, this can be achieved in one of three ways; encapsulation[23,24], charge stabilisation[25] and steric/ligand stabilisation[24].

Encapsulation is a method where the particles are trapped in a solid medium of some form to prevent them from coming into contact with each other and thus sterically preventing aggregation (Figure 2, A). Some examples of encapsulation would be, classic red stained glass in church windows (this was less common post 19th century due to availability of cheaper options), or in polymer gels[24,26].

Ligand stabilisation is chemical binding of a compound to the surface of the GNP, thus creating a physical shell around the particles preventing them from coming into close enough contact to each other to aggregate. Another form of this stabilisation is fixing the particles to a surface using a rigid connecting ligand, preventing the particles from getting close enough to aggregate, while not entirely encapsulating them (Figure 2, B). This method is very common due to the ability to affix a wide range of end groups and therefore functionalities to the opposite end of the ligand attached to the GNPs.

Multiple functional groups can be used to bind to the gold surface, some of the possibilities are an alcohol or amine group but the most common and strongest is the gold-thiol bond. With an average enthalpy of formation (ΔH_f) for a gold- thiol bond being approximately 418 $KJmol^{-1}$ and the next strongest bond to gold being gold-boron (368 $KJmol^{-1}$)[27,28], thiols will readily replace other ligands on a particles surface very rapidly and form a self-assembled mono-layer[29]. There are many examples of different ligands being bound to a particle's surface in this way, including long chain poly-ethylene glycol[6,30], peptides[6,31] and anti-bodies[4] to name a few.

Finally, charge stabilisation is a method were a charged compound is either covalently bound to the GNP surface, such as citrate is in the Turkevich synthesis method[32,33], or covalently bound to the end of a ligand stabilising shell with a charged end group, this charged surface causes the GNPs to repel each other preventing them from aggregating (Figure 2, C). The encapsulation method is not used in this body of work and therefore will not be discussed further.

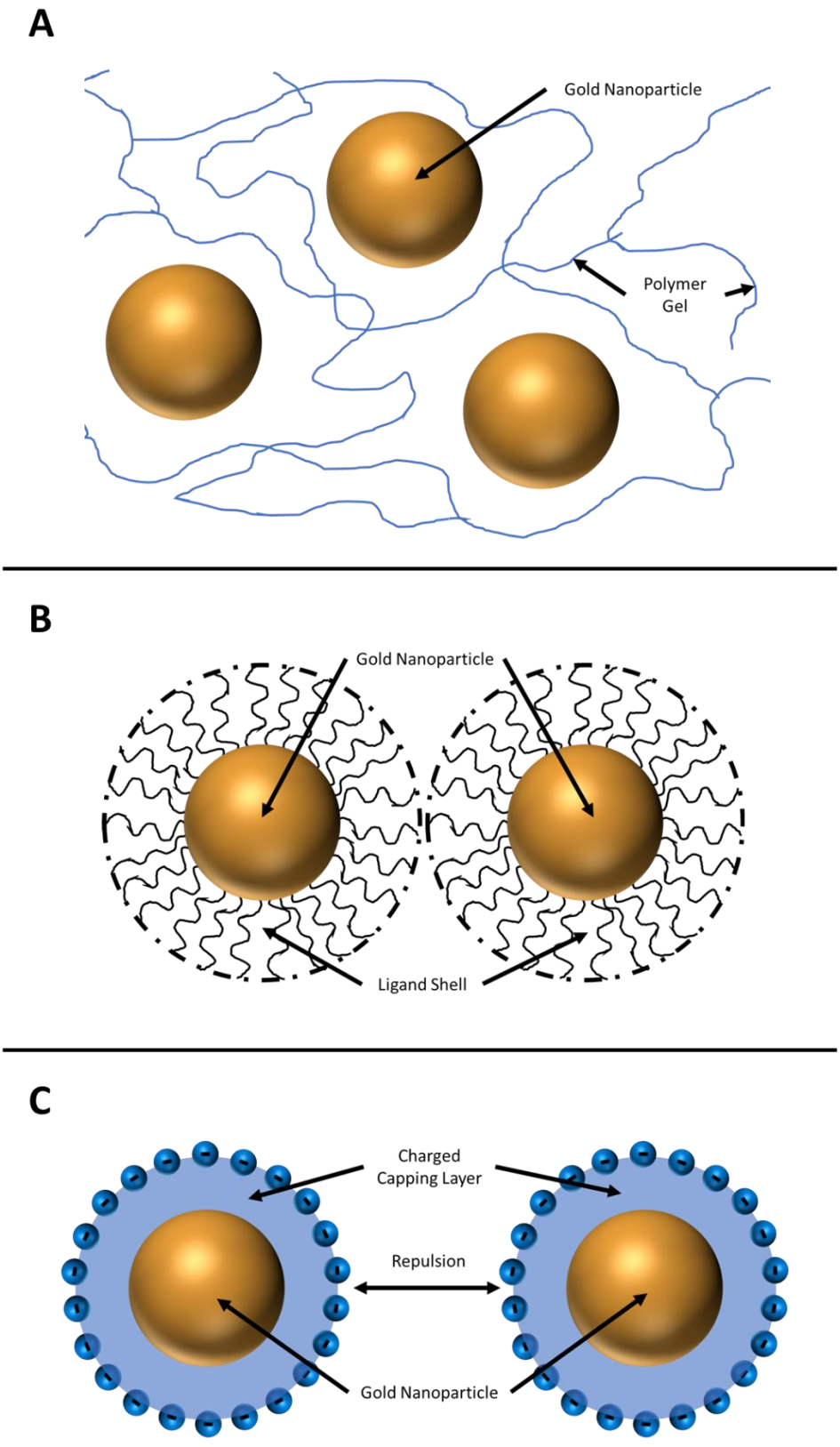

Figure 2: Schematic of the three forms of nanoparticle stabilisation: A Encapsulation stabilisation, B Steric/Ligand stabilisation, C Charge stabilisation.

Gold nanoparticle synthesis can be achieved in a whole multitude of ways, however, for biological applications the synthesis and all the starting products need to be either non-toxic or easy to remove post-synthesis if toxic. The most common synthesis, due to its lack of toxicity and production of highly controlled mono-disperse samples, is the Turkevich synthesis or modifications thereof[32,33]. The source of the gold in this method is the tetrachloroaurate complex where the gold is in oxidation state III and the reducing agent is citrate, which is also the stabilising agent once it has been reduced to its ketone form (Figure 3) (in other methods the reducing agent and stabilising agent can be different chemicals)[34].

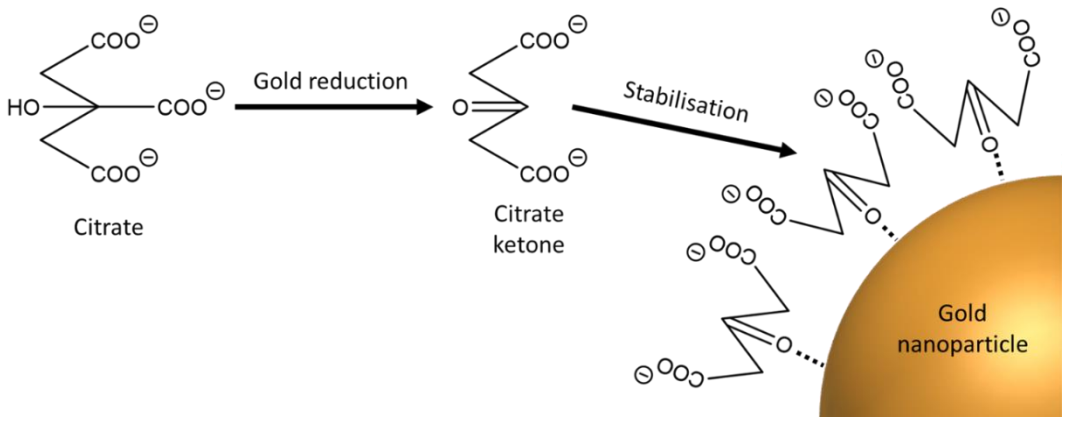

Figure 3: Schematic of citrate stabilisation of gold nanoparticle.

Three electrons are required to fully reduce the gold enabling it to become part of the nanoparticle, but each citrate can only provide two electrons (Figure 4) so the ratio between the citrate and the gold needs to be 3:2 or the citrate can be used at higher concentrations.

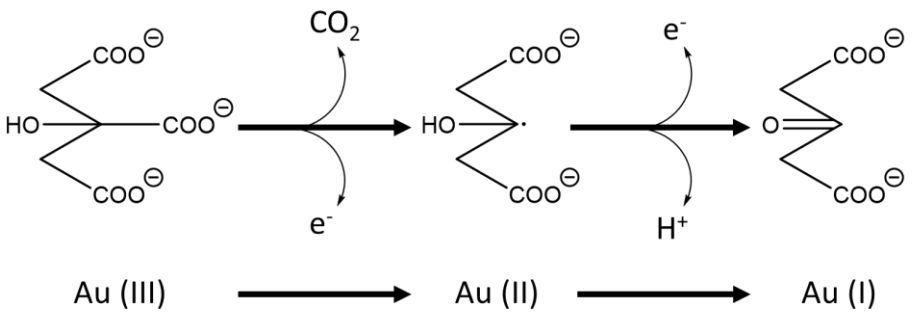

Figure 4: Approximate gold reduction equation[34].

Other important factors that have been shown to contribute to the synthesis process are; consistent temperature, consistent mixing and pH. The temperature and mixing are kept consistent during the synthesis by a magnetic stirrer bar and any additions are pre-heated to prevent temperature eddies. The pH in all the synthesis experiments was kept between 6-7 to cause no significant deviation in particle synthesis.

The key steps in a synthesis are fast nucleation, i.e. all seeds/nucleation points formed simultaneously; followed by slow propagation so the nanoparticles grow into as mono-disperse a sample of spherical gold nanoparticles as possible. This is achieved in the Turkevich method by heating the gold up above the reacting temperature (in reverse-Turkevich[35] and other variations the reducing agent citrate is pre-heated to the reacting temperature first) and then adding pre-warmed reducing agent quickly to the rapidly stirred solution to prevent small fluctuations in temperature during the initial nucleation step. By ensuring the citrate remains above the previously mentioned 3:2 ratio this enables the rapid reduction of all the gold salt in this initial step (at least to gold I oxidation state). Then the slow propagation is

maintained by the quantity of stabilising agent present in the solution (which in this method is citrate).

Some modifications to the method such as the addition of tannic acid, can aid greatly in the initial kinetics of the reduction whilst also providing a bulkier stabilising ligand than citrate does. The bulkier tannic acid allows the formation of smaller mono-disperse samples that are stabilised by citrate[35]. GNPs stabilised by citrate also provide a very easy platform to change the stabilising ligand (as discussed previously in this section) as well as providing a non-toxic sample essential for biological experiments.

1.1.3 – Electrochemical Double Layer

Functional end groups are usually chosen for a specific purpose such as; cellular uptake[6], fluorophore[36], drug release[26] or peptide binding[6]. However, once these end groups are introduced into biological media they can interact differently and form surface layers which may change their chemistry at the GNP surface or block the desired functionality[14–17]. One such effect that we attempt to study in this body of work is the electrochemical double layer (EDL).

End groups of the stabilising layer can often be charged or can become charged when introduced to a complex media, like in biological systems, this can even be the aim as it can induce or aid the cellular uptake of GNPs[37–39]. In biological media these particles are often exposed to large concentrations of electrolytes (some typical values in

mammalian cells both intra and extracelluar are: sodium 5-15/145mM; potassium 140/5mM; chlorine 5-15/110mM[40]), which then leads to the formation of an EDL.

The EDL (sometimes just referred to as the double layer) is a structure that is dominated by electrostatic forces whose behaviour was originally modelled mathematically by Coulomb and found to obey the below law (Equation 1). Where Z_1 and Z_2 are points of charge (C), r^2 the distance between the charges (m), ε_0 is the vacuum permittivity ($C^2J^{-1}m^{-1}$) and ε_r is the relative permittivity of the medium (unitless)[41,42].

$$F = \frac{Z_1 Z_2}{4\pi\varepsilon_0\varepsilon_r} . \frac{1}{r^2}$$

Equation 1: Coulomb's Law[41,42].

As can be seen in Coulombs Law (Equation 1) this force is highly dependent on distance and decreases rapidly with separation, so it should have very little effect on atoms that are further than a few nanometers from the charge. The original model of the EDL structure was created by Helmholtz under the assumption that the charges form two ordered plates like a capacitor, however, this model did not account for the weaker Coulombic interactions in the surrounding bulk solution and the experimental results for capacitance variation against applied potential were found to vary greatly from the predictions (Figure 5). The experimental data presented below is taken from Electrochemistry Principles, Methods and Applications by Brett.C.M.A & Brett.A.M

pages 43-51, and the experimental data shows the variation of the capacitance differential of sodium fluroide at mercury with respect to the potential.

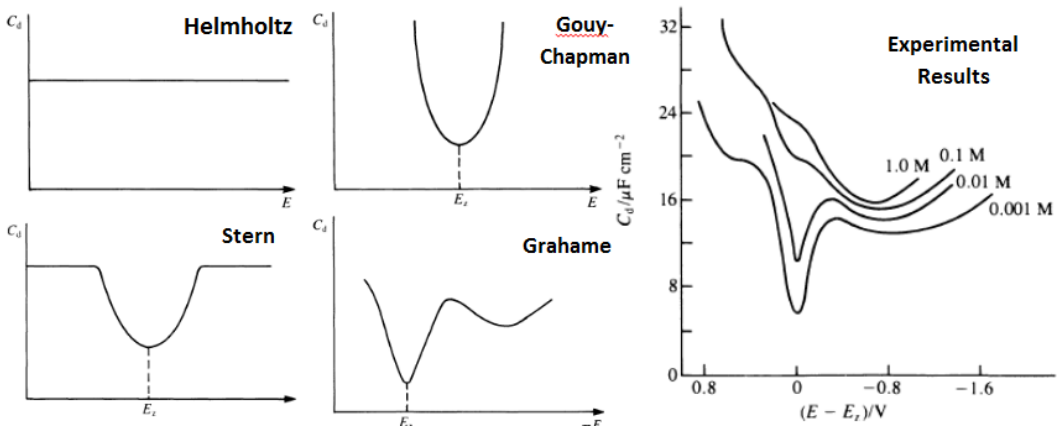

Figure 5: Comparison of the double layer mathematical models with the experimental data (taken from Electrochemistry Principles, Methods and Applications by Brett.C.M.A & Brett.A.M pages 43-51)[42]

Gouy and Chapman modelled the diffuse/ slipping layer of charge further from this initial ordered layer causing it to be less strongly bound and ordered, but still subject to Coulombic forces. This model more accurately accounted for the surrounding solution but on it's own was still not adequate as this predicted the capacitance could approach infinity which is not possible due to the physical limitations of atoms can't occupy the same space. However the combination of the model with the Helmholtz model by Stern gave predictions much closer to the experimental results. This model has been improved again by Grahame, to include an adsorbed layer absent of a solvent cage, referred to as the Inner Helmholtz Plain (IHP), before the original fixed plane of charge Helmholtz modelled, referred to as the Outer Helmholtz Plain (OHP) (Figure 6).

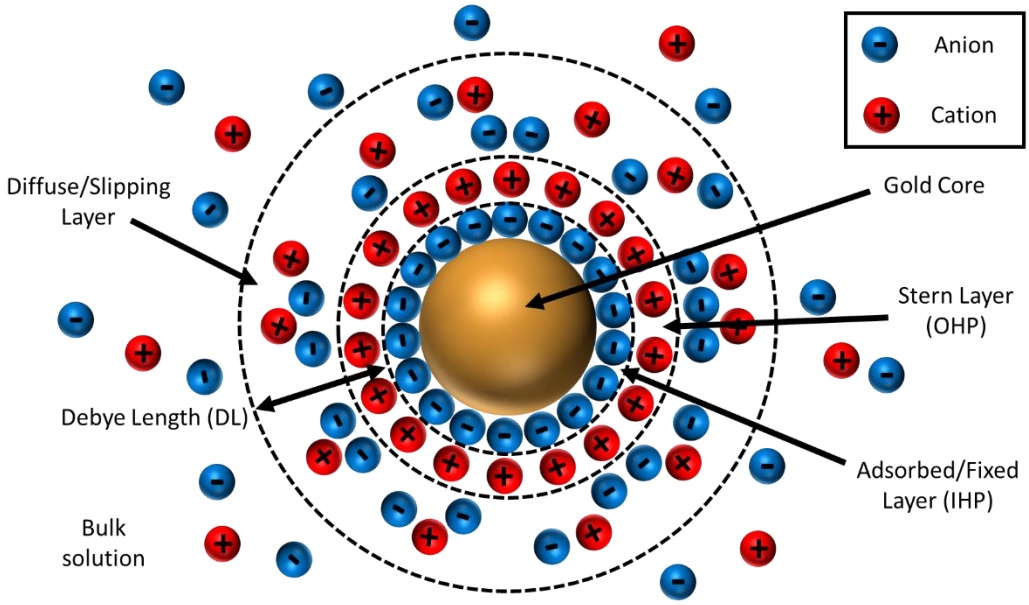

Figure 6: Schematic of Electrochemical Double Layer formation on a gold nanoparticle surface[20].

An important parameter in defining the EDL is the Debye Length (marked in Figure 6) which is usually calculated theoretically using Debye-Hückel theory. The formula for calculating this is given below (Equation 2); where ε_r, ε_0 and Z are defined as before (Equation 1); K_B is the Boltzmann constant (JK^{-1}); T is the temperature (K); e the elementary charge (C) and n_i^0 is the concentration of the ions in the bulk solution ($moldm^{-3}$)[42,43].

$$\chi_{DL} = \left(\frac{\varepsilon_0 \varepsilon_r K_B T}{2 n_i^0 Z^2 e^2} \right)^{0.5}$$

Equation 2: Debye length related to ionic strength formula[42,43].

The Debye length is usually on the order of a few nm at its largest, so it is hypothesised that this could be directly measured, using a novel centrifugation technique, discussed later in the introduction (differential centrifugal sedimentation). This technique will lead to the particles moving in a given direction under centrifugal force, however, the particle and the slipping layer of the EDL will move at different speeds causing a retardation force to be experienced by the particle in the opposite direction (Figure 7). This phenomenon is also observed in electrophoresis experiments and is called the electrophoretic effect; this will need accounting for at the analytical stages of data processing.

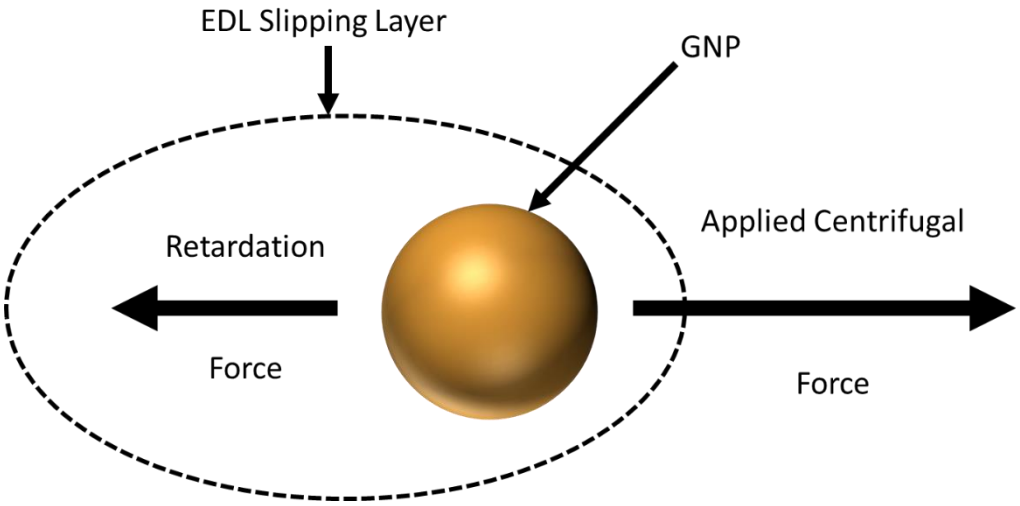

Figure 7: Electrophoretic effect[41]

1.1.4 – Protein 'Corona'

As previously mentioned, surface functional groups on nanoparticles can also interact with proteins in a variety of ways, similar to how functional groups, within the protein itself aid in folding, such as hydrogen bonds, disulphide bridges and ionic interactions with charged protein side groups[40]. It has been known for quite some time that once introduced into biological media gold nanoparticles will adsorb proteins to their surface[44], some of which will be loosely bound and some firmly chemically bound to the surface or the ligands. This additional layer has the potential to change the GNPs surface reactivity and their functionality. There are competing theories as to whether the protein 'coronae' changes reactivity by dampening intended functions of designed nanoparticles[14–17], or whether this 'corona' is the actual cause of internalisation and some of the observed effects attributed to nanoparticles in situ[15,17–19]; or even possibly a cause for worry as the new reactivity could have completely unforeseen and potentially dangerous effects within the cells. However, all theories are in agreement that a greater understanding of the process of binding, the degree and strength of the binding are all greatly important, which has spurred interest in this research area over the past few years.

Biological growth media and the cell cytosol consists of a huge range of proteins and the corona formed around the GNPs after internalisation could consist of a varied combination of proteins. Very little is understood about the construction and material in the 'corona' due to this huge complexity[45] and to determine this would require a wide range or techniques and a timescale beyond the scope of the project.

To simplify the problem, a singular model protein was chosen, in this case Bovine Serum Albumin (BSA), as serum albumins are the most abundant protein family in biological systems (approximately 35-50 g/L or 0.53-0.75mM[40,46]) the bovine analogue was chosen due to its relatively cheap cost, availability and its well-known structure (Figure 8)[47].

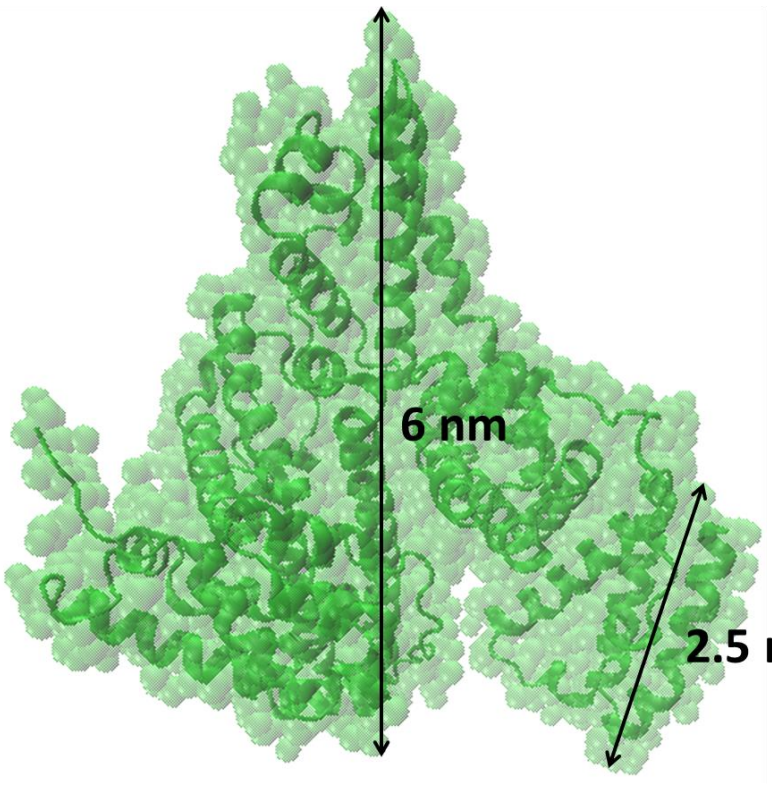

Figure 8: Structure of Bovine Serum Albumin (created fromDOI: 10.2210/pdb4f5s/pdb, 4F5S PDB file using VMD software) with approximate measurements taken from the structure[47].

The protein corona itself has weakly and strongly bound peptides and is an equilibrium process where the proteins are constantly exchanging making it a difficult process to follow and analyse (Figure 9). The proteins are bound to the GNPs by the side groups accessible in their folded state, such as the ones discussed briefly before,

but in theory it is also possible they could form hydrophobic/philic interactions in an unfolded or altered state which would, in turn, expose other groups. Due to this complexity this project will focus on how quickly the protein corona forms, whether it is monolayer or multilayer and if the kinetics for this process can be determined instead of how it is bound.

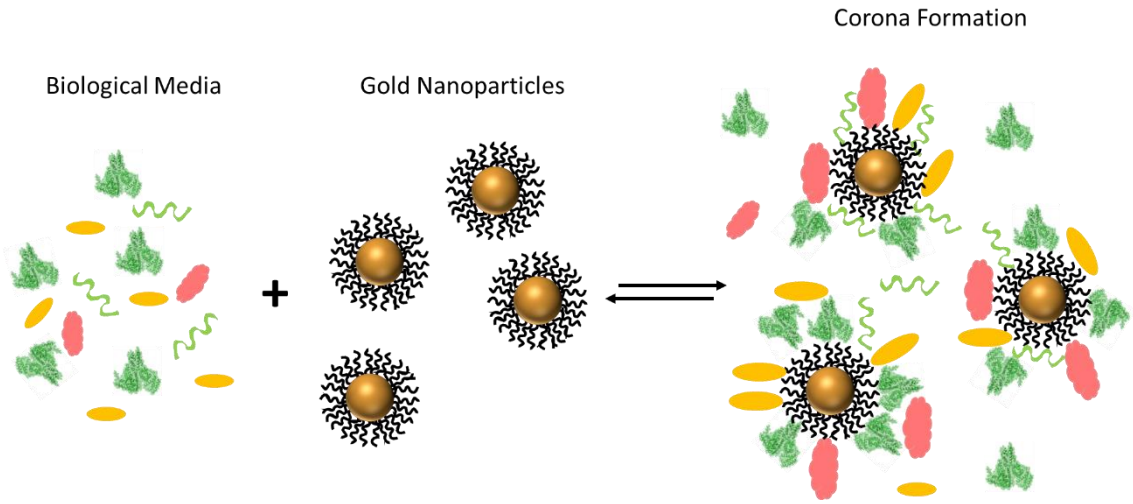

Figure 9: Schematic of corona formation in complex biological media. The biological medium is hypothesised to bind to GNPs in a random array of various proteins competing for adsorption sites[10,48,49].

Previous studies of the protein corona have utilised techniques such as, fluorescence correlation spectroscopy[50–54], transferrin binding and dynamic light scattering[13,55–59] the merits and drawbacks of which will be discussed in more detail in the related chapters discussion section (4 – Differential Centrifugal Analysis of Protein "Corona"). The growth of the corona with respect to the concentration of the protein in the surroundings, has been found to follow a similar pattern to the Langmuir isotherm; or more appropriately the Hill model, which is the Langmuir isotherm for a disperse

colloidal surface[60–62]. The mathematical model is shown below (Equation 3), were K'_D is the equilibrium dissociation coefficient, [P] is the concentration of free protein ($moldm^{-3}$), N is the number of protein adsorbed on the particle, N_{MAX} is the maximum number of protein that can adsorb on the particle and n is the Hill coefficient.

$$N = N_{MAX} \frac{1}{1 + (K'_D/[P])^n}$$

Equation 3: Hill equation for modelling the dependence of N on [P][51,60–62]

If the Hill coefficient, which is a measurement of how co-operative (>1) or 'anti' co-operative (<1) the protein binding to the surface is, is equal to 1, i.e. no preferential or competitive binding, then the model collapses into just the Langmuir isotherm. This model is the one most often used in the field so is used for our data to allow for direct comparison, however there are other possible models suitabile for different binding regimes that are discussed in more detail in the relevant chapters analysis sections (4 – Differential Centrifugal Analysis of Protein "Corona").

1.2 – Characterisation Methods

1.2.1 – UV-Vis Spectroscopy

Due to the small size of nanoparticles and their high surface to bulk atom ratio they have unique optical properties that can be used to characterise aspects of these particles. Here I will discuss in brief, two of these effects and the way in which they are used for characterisation.

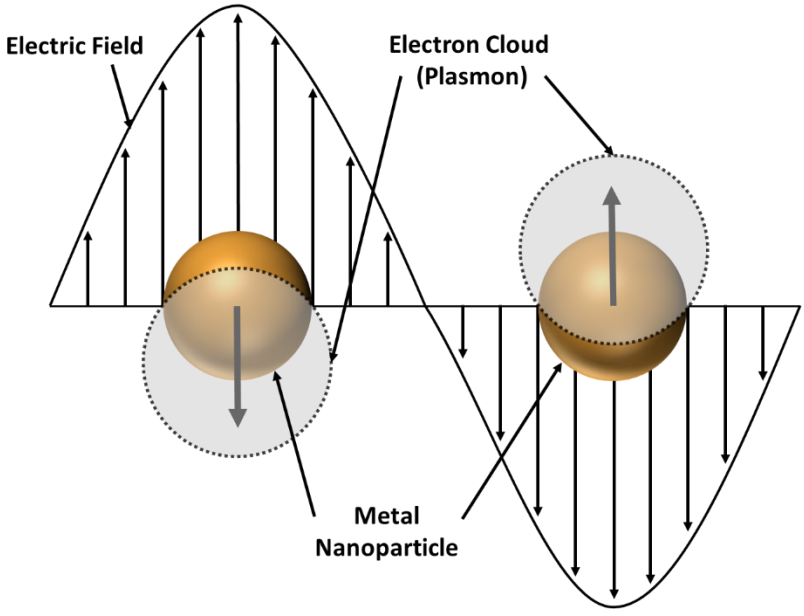

Figure 10:Schematic of surface plasmon's interaction of metal nanoparticle with an electromagnetic field.[43]

Gold has the following electronic configuration [Xe] 4f14 5d10 6s1; on the surface of the nanoparticle the 6s1 valence electrons are delocalised in the conduction band, forming a cloud that is referred to as a surface plasmon. When particles with a surface plasmon are smaller than the wavelength of the electric component of an electromagnetic field, at certain frequencies this causes the plasmon to oscillate in the opposite direction (Figure 10); this affect is called surface plasmon resonance (SPR). The SPR causes enhancement of the absorption and scattering of the light frequency that causes the oscillation, which can be observed spectroscopically using UV-Vis absorption spectroscopy (Figure 11) or physically by the distinctive colour of the solution (Figure 11 inset)[2,43,63].

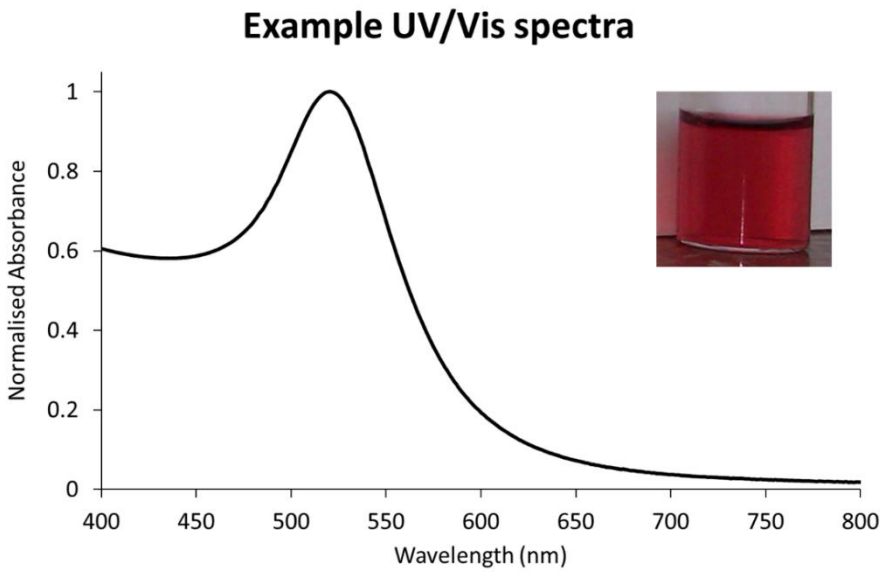

Figure 11: A representative spectra of citrate stabilised gold nanoparticles with an inset image of the sample (spectrum has been cropped to show the relevant data). The peak in the image being the SPR band in absorbance.

This surface plasmon and its frequency is highly dependent on many variables such as; the material, the size, the shape, the protective coating and the suspension media (these two are collective referred to as surrounding dielectric medium). Therefore UV-Vis spectroscopy is quick and inexpensive tool for qualitative and quantitative characterisation of a range of properties. Following the method laid out by Haiss et.al[64,65] the approximate size and concentration of a nanoparticle sample can be very quickly determined. In brief Haiss et. al modelled theoretically, using Mie's solutions to the Maxwell electromagnetic equations', the relationship between the size of spherical gold nanoparticles and the amount of scattering and absorption expected; using a wide size range of nanoparticles the model was confirmed experimentally. Given these results and the model a correlation between the ratio of the absorbance value at the SPR (A_{SPR}) and the absorbance at 450nm (A_{450}) was noted and the below relationship derived where B1 and B2 are constants taken from the experimental fitting.

$$d = \exp\left(B_1 \frac{A_{SPR}}{A_{450}} - B_2\right)$$

Equation 4: Haiss formula for approximate diameter of particles from absorbance values.[64,65]

Using the two absorbance values (A_{SPR}/A_{450}) and the list of ratios provided in the supplementary information for the Haiss et al the approximate size of the GNPs coated in citrate in aqueous solution can be quickly determined. The supplementary information of this paper also contains a list of calculated extinction coefficients for each size of nanoparticle, which can then be entered into the Beer-Lambert law[66]

(Equation 5) with the A_{SPR} to give the estimated concentration of nanoparticles. Where the A is the absorbance, C is concentration (M), l is the path length (cm) and ε (M^{-1} cm^{-1})[46] is the molar absorption coefficient.

$$A_{SPR} = \varepsilon C l$$

Equation 5: The Beer-Lambert law[66].

As previously mentioned when the protective coating/capping ligand is exchanged then the exact frequency of the SPR changes (usually by at least a couple of nanometres), allowing for a quick qualitative way to verify successful ligand exchange has occurred (Figure 12).

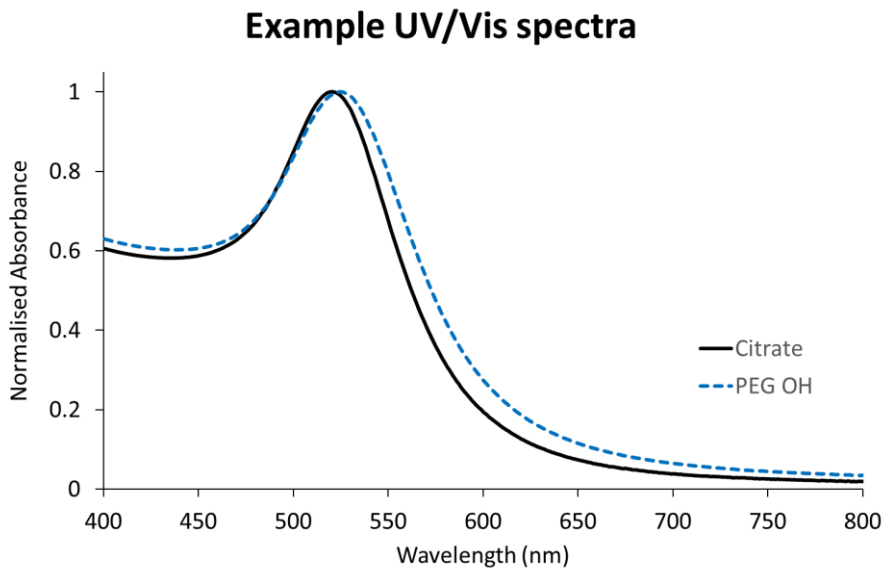

Figure 12: A representative UV-Vis spectrum showing the comparison of gold nanoparticles stabilised with citrate or with a short chain PEG OH (the PEG OH has 11 carbon units and 4 ethyl units, the spectrum has been cropped to show the relevant data). A clear shift can be seen with the two different capping ligands.

1.2.2 - Dynamic Light Scattering

Dynamic light scattering (DLS) is a very common method of sizing nanoparticle samples. DLS works by directing a polarised light source at the sample and measuring the resultant diffracted light pattern. By pulsing the light source and using an autocorrelation function to analyse the scattering, allows for dynamic data of even relatively small particles in complex solutions. The scattering however is dependent on the optical cross section of the particle, so it is highly size dependent[67]. This essentially means that larger particles will contribute much more to the scattering signal than their smaller counter parts; so, a sample measured by DLS is always skewed greatly towards larger particles present in the sample. The data can be deconvoluted mathematically but there are also practical solutions which are taken advantage of by other methods discussed below[31].

This project used this technique sparingly and only as a quick comparison to measurements done using DCS; so a more in depth understanding is not required.

1.2.3 - Differential Centrifugal Sedimentation

Differential Centrifugal Sedimentation (DCS) is a form of Analytical Ultracentrifugation (AUC), that is a less commonly used method of sizing particles. The machine we used to perform these measurements is called the Centrifugal Particle Sizer (CPS model DC24000, provided by CPS instruments Figure 13) and its method of detection for particles is the same in principle as the DLS, however, the benefit of this machine is that the sample is separated out by size before it reaches the detector. It is also important to note that with the CPS machine size calculations are not derived from the resultant scattering as is the case with DLS. It instead calculates the size based on sedimentation time which is discussed in greater detail later.

Figure 13: Image of the CPS machine.

Centrifugation works by applying centrifugal force (usually denoted by the unit g) to objects inside the centrifuge, which usually consists of a spinning component of a known path-length or radius (r), which conventionally can be used to concentrate down a sample or clean or separate a mixed sample.

Small particles require very large g forces, to overcome their intramolecular interactions and Brownian motion, and precipitate over a reasonable time frame. These requirements led to a subcategory of centrifuges being developed, capable of achieving very large g forces, called ultra-centrifuges. Early analytical centrifuges (1920s Svedberg et. Al)[68] were developed with the specific intention of obtaining size distributions of gold colloids and were so successful that they rapidly expanded in to the field of macromolecules and biophysics where it remains a standard characterisation method.

Traditional centrifugation causes samples to be separated out by density, i.e. samples with the same density, for example different sized particles of the same material, will all precipitate at the same time, this phenomenon is called “streaming or sedimentation instability”[68]. This occurs just as a homogeneous liquid sample of differing densities would settle out on mass to limit surface interactions. By setting up a density gradient within the centrifugal medium the effect of “streaming” can be removed as the net density (or average density of the fluid plus that of the particles) increases as the particle passes through the gradient ensuring it is always higher in the next step, this removes any driving force for mass sedimentation of the sample. This effect is described by the sedimentation stability formula below (Equation 6),

where $\delta\rho_{net}$ is the net density of the fluid and δR is the distance from the centre of rotation.

$$\frac{\delta\rho_{net}}{\delta R} \geq 0$$

Equation 6: Condition for sedimentation stability.

The required gradient is dependent on the net density of the solution including the sample's density. So, if a sample is highly concentrated or has a high density like gold nanoparticles, the range of the gradient must be larger than for other samples to ensure stability during sedimentation. A density gradient with a fluid height of less than $0.01 gml^{-1}$ is usually sufficient to provide stability and the greater the height the more separation is achieved. The denser the gradient the longer the sample will take to pass through the gradient, so a compromise is required (the CPS instrument used in this thesis had optimised density gradient suggestions for gold nanoparticles that were used throughout). The creation of density gradients in centrifugation to allow for high resolution separation of molecules with small differences in mass and similar densities has been used in biology for years to separate out and observe mutations of as little as one or two amino acids within the same proteins[69].

The CPS takes advantage of the high speeds of ultracentrifugation and the principle of density gradients during centrifugation to allow for highly accurate sizing of particle size distributions between the ranges of 0.003-60 µm. Below is a schematic

of exactly how the CPS is built (Figure 14). The CPS consists of a reinforced plastic ring (the reinforcement is to allow for the high speeds needed for ultra-centrifugation, 12.5cm in diameter), a disc closure (to allow the disc to be cleaned and to prevent spillages outside of the ring during use), an injection point allows for the construction of the gradient as the centrifuge is running and the addition of the sample afterwards, the CPS also contains a light source (405nm wavelength) and a detector[70–72].

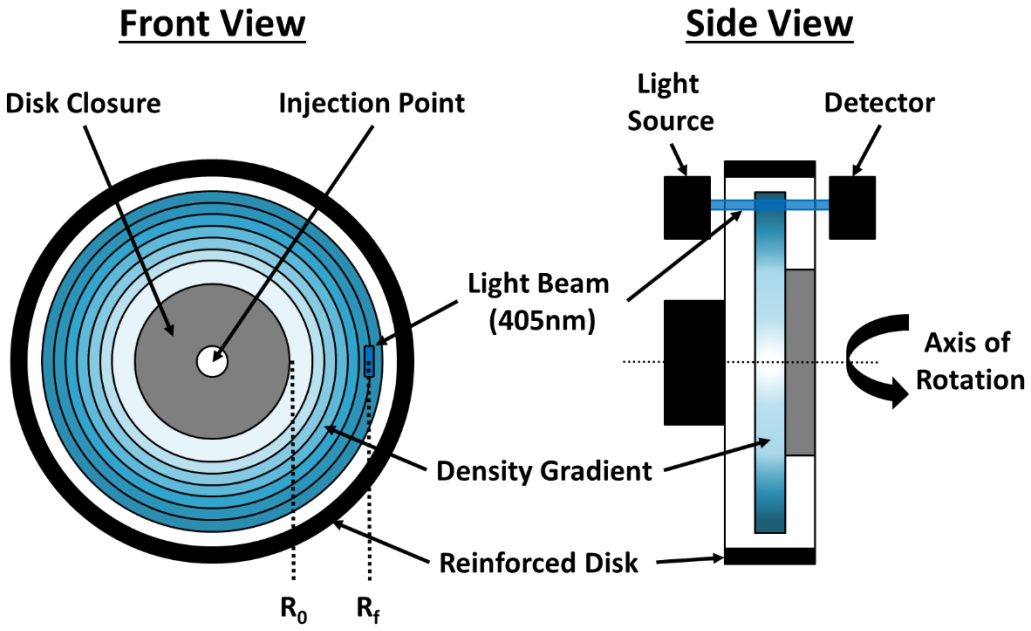

Figure 14: Schematic of the CPS machine's internal structure[70–72].

The gradient is built up by injecting various concentrations of sucrose into the ring, starting with the highest concentration (and therefore most dense) of sucrose on the outer edge of the ring incrementally lower sucrose concentrations, to the last injection of the least concentrated (and therefore least dense) step on the inner most edge of the ring. The gradient is then allowed to blend under centrifugation for at least 15 minutes allowing the injections at the step edge to merge and form a smooth

linear gradient. The densities of the sucrose solutions used to build the gradient can be adjusted depending on the sample run; i.e. lower density samples require a less severe gradient (2-4% sucrose) and the high density samples can require a more severe gradient (8-36% sucrose); as long as it meets the gradient stability requirements previously discussed, the samples will sediment well enough to be analysed. Also, as previously mentioned, for all samples measured in this thesis the density gradient suggested by CPS instruments, as the optimum balance between timing of sample measurement and accuracy, was used. This gradient runs from 8% w/w of sucrose at the inner most edge to 24% w/w of sucrose at the outer most edge (the exact methodology of the method and the additions is listed in the experimental section, 2.4 - Centrifugal Particle Sizer Standard Setup). After the gradient has been added to the CPS system, a final injection of 0.5mL of dodecane is added after the gradient to prevent the solution from evaporating over the course of sample measurements.

The heavier particles (i.e. more mass) travel through the gradient faster than the smaller ones and thus are separated as they pass through the gradient, the particles then pass through the light source, causing scattering which is detected and their time and absorbance is noted. Below is a rough schematic (Figure 15) of how, the particles are separated as they move through the sucrose gradient and then detected creating the readout.

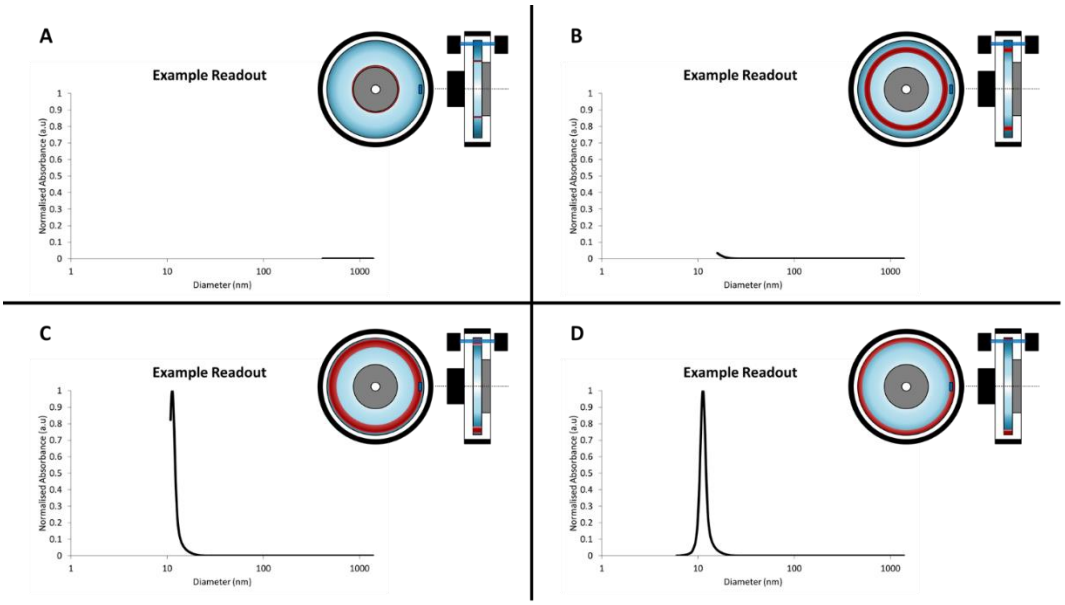

Figure 15: Schematic of particle separation and readout over time.

The particles precipitate under the applied centrifugal force following the dependence on time modelled by Stokes Law modified for particles of low Reynolds numbers. Below is the equation to show the relationship between D the diameter (µm) of nanoparticles with relation to t, which is the time taken for the particles to sediment from R_0 to R_f (s); where η is the fluid viscosity (Pa.s), R_f is the final radius rotation (cm), R_0 is the initial radius rotation (cm), ρ_p is the density of the particle (g.mL^{-1}), ρ_f is the density of the fluid (g.mL^{-1}), and ω is the rotational velocity (rad.s^{-1}).

$$D = \left\{\left(18\eta ln\left(R_f/R_0\right)\right)/\left(\left(\rho_p - \rho_f\right)\omega^2 t\right)\right\}^{0.5}$$

Equation 7: Stokes - Einstein equation arranged to solve for diameter[31,70–72].

Reynolds number is a prediction of how long a spherical particle will take to go from laminar flow through a system to turbulent flow. Turbulent flow is a term referring to a regime where the particle moving through the flow (or the flow moving around the particle) is more dominated by the inertial forces causing eddies and vortexes. Laminar flow is a term referring to a regime where a particle has linear parallel flows to the movement of the particle and is dominated by viscosity forces. Laminar flow is the flow required during this CPS method as it causes minimal damage to the density gradient with each sample; or at least for the distance of the disc. For particles within the machine's stated range, the Reynolds number is low enough.

By running a polyvinyl chloride (PVC) spherical bead standard of a known size through the system before each sample, all of the variables except time are fixed. These known values allow the samples size to be calculated using the time taken for the particle to sediment from point R_0 to R_f. Also, the PVC control runs counteract any changes in the gradient that might have been caused by any previous samples run through, essentially creating a new baseline before each new measurement.

The theoretical maximum resolution for this machine is quoted as full separation of the sample at 5% of the diameter or partial separation at 2%. This statement indicates that two perfectly narrow distributions with a difference of diameter of greater than 2% can be separated so that less than 5% of their distributions overlap. So, a 10nm sample could be separated completely from a 10.2nm sample. This level of resolution would in theory allow for analysis of very subtle differences in nanoparticles distributions. This resolution is calculated by the manufacturer to include; injection

effects, physical impact of the injection, sample thickness (which is calculated for a sample of 0.1ml) and Brownian motion[70–72].

Work done immediately prior to this project, by myself and other members of the Brust group demonstrated that DCS can be used to accurately determine the size of a nanoparticles core as well as the size of the ligand shell[31]. This work included measuring very subtle differences between PEG ligands with only a couple of carbons difference in length that led to the aim of this thesis, into the limits of what this method can measure.

The true density of particles and the associated ligand shell is usually unknown and too difficult or time consuming to determine to any level of accuracy so for DCS the particle density ρ_p is assumed to be that of gold 19.3 gcm^{-3}. This assumption can be reasonable when the particle is much larger, or the core is a large percentage of the totally density compared to the protecting ligand. However, for nanoparticles this is often not the case, for example in a nanoparticle of 10nm diameter with a medium sized PEG approximately 1nm then the gold core represents approximately only 58% of the particle (just using simple geometric reasoning). So, the further the particles are from the assumed density of gold, the greater the miscalculation of the diameter by the software.

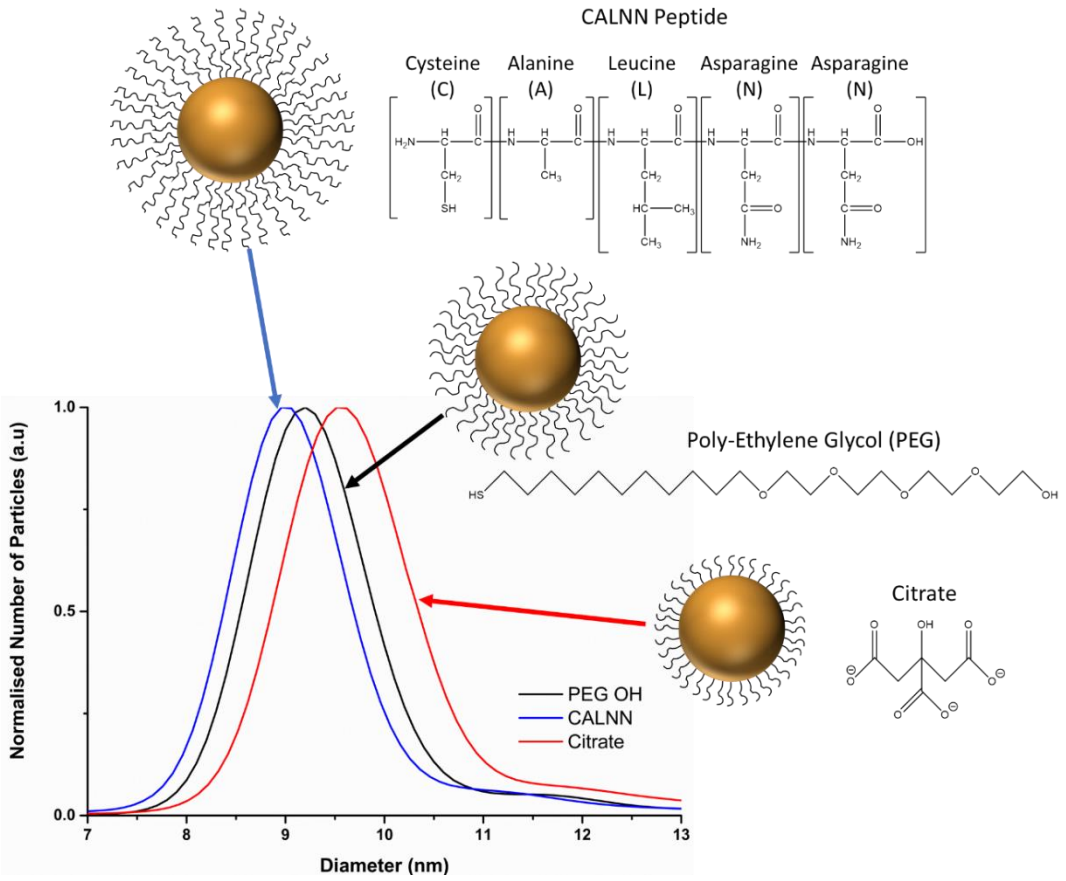

Figure 16: Example of different particle measurements and the shift values due to assumed density.

Figure 16 is an example of one batch of nanoparticles (i.e. the same sized gold core) stabilised in three different ways; citrate, short chain poly-ethylene glycol (PEG) (with 11 carbon units followed by 4 ethylene repeat units), and a short peptide chain with CALNN as the amino acid sequence (Figure 16). The paper published on our findings covers a wider variety of ligands and particle sizes[31] but for the purpose of an explanation these three will be sufficient. As can be seen from the image above despite the fact that the ligands progressively get longer the reported size of the particles is progressively smaller. This is due to the longer ligands representing a higher proportion of the GNP, thus the error caused by the density assumption is larger, causing the larger ligands to report a smaller GNP size compared to the smaller

ligands. We addressed this problem by first replacing ρ_p by a new term ρ_{eff} which is the effective density of the entire particle (Equation 8), which is a geometric separation of the density into the core's density and ligand's density.

$$\rho_{eff} = \frac{d_{core}^3 \rho_{core} + ((d_{core} + 2s)^3 - d_{core}^3)\rho_{shell}}{(d_{core} + 2s)^3}$$

Equation 8: Geometric splitting of particle density into core and ligand density.

The parameters in the above equation are as follows; d_{core} is the diameter of the core (µm), ρ_{core} is the density of the core (which in this case is gold, 19.3gcm^{-3}), s is the ligand length (µm), and ρ_{shell} is the density of the ligand shell (gcm^{-3}). This initially introduced too many unknown parameters, so by independently verifying the length of the CALNN peptide with a known density (1.4gcm^{-3}), it was possible to then calculate the core size. If the core size does not vary we could solve the equation for all future ligand coating sizes of approximate known density provided the nanoparticle batch was the same.

The CALNN peptide, following the preparation method used, had been determined to have a relative packing density of 2.4 peptides/nm^2 giving a densely packed shell. As the shell is very densely packed it was hypothesised to have the peptide in its most extended conformation making it a minimum thickness of 1.5nm and a maximum possible extension of 1.7nm (with a less packed layer allowing for more solvation). This extended conformation was confirmed using FTIR (this method of characterisation is discussed in more detail in the next section of the introduction)

analysis of the amide 1 band of the peptide once bound to the nanoparticles; a value of 1.6nm was used in our calculations, as the peptide was seen to be partially solvated using the FTIR data.

The short peptide is expensive and not reasonable to use as a permanent "ruler" system for every batch to calculate the core, so the value for citrate (1nm shell thickness) was used to calculate the core of each new batch of nanoparticles. This calculation accounted for the core and ligand shell thickness of all our functionalised nanoparticle systems prior to any experiments, an example of the recalculation of the example is shown in Figure 17 below.

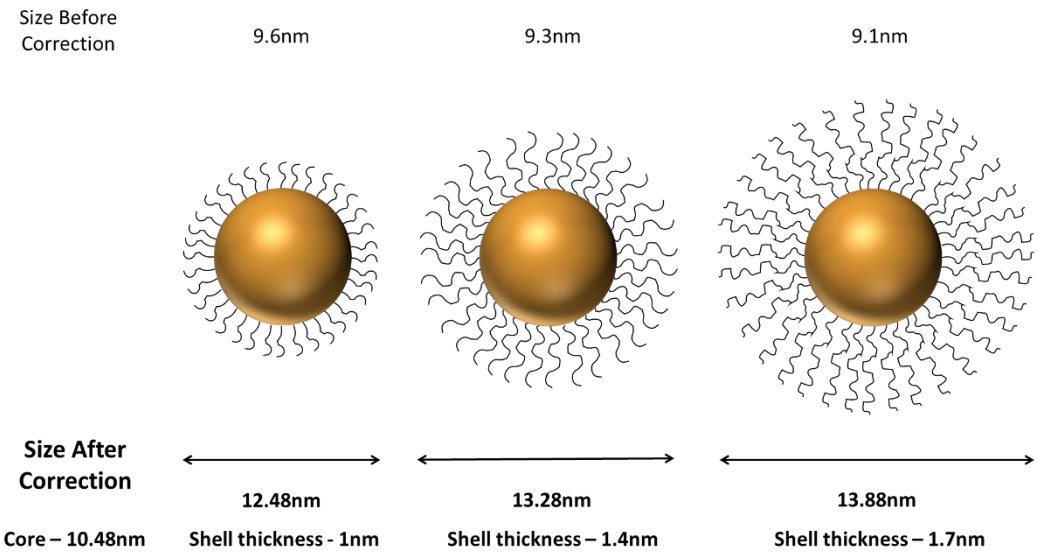

Figure 17: Schematic of the recalculation of data to provide actual size of the functionalised GNP and its core size (values shown are approximate).

1.2.4 - Fourier Transform Infra-Red Spectroscopy

Fourier Transform Infra-Red spectroscopy (FTIR) exposes a sample to a source of infra-red light and the absorption or emission spectrum is recorded and analysed. This technique can be used to determine the approximate concentration and surface coverage/packing density of molecules on the surface of a nanoparticle. FTIR can be particularly useful with peptide ligand shells as the FTIR spectra can give insight into the structure of the protein, which combined with the packing density can give additional information about the ligand shell thickness (an example of this was discussed previously in the DCS section of the introduction[31]).

Protein structure is traditionally broken down into four categories; primary, secondary, tertiary and quaternary structure (Figure 18)[40]. Primary structure, is the amino acid sequence, which is determined by the DNA sequence and transcription process. Secondary structure, is structuring such as; α-helixes, β – strands, sheets and turns; all of which are highly ordered structures controlled by hydrogen bonding between groups on the main chain of the peptide (not from the side groups). Tertiary structure, is the three-dimensional folding of a protein into its final structure, which is controlled by hydrophobic/hydrophilic regions within the protein and further stabilised by intra-molecular bonds such as; ionic bridges, hydrogen bonds (in the side groups of the amino acids), π-stacking and di-sulfide bridges. Finally, quaternary structure is the structuring of at least two proteins coming together to make much larger complexes, some common examples of this are haemoglobin (made from two,

matching, pairs of proteins) and collagen (helical peptides that come together in threes to form triple helix structures).

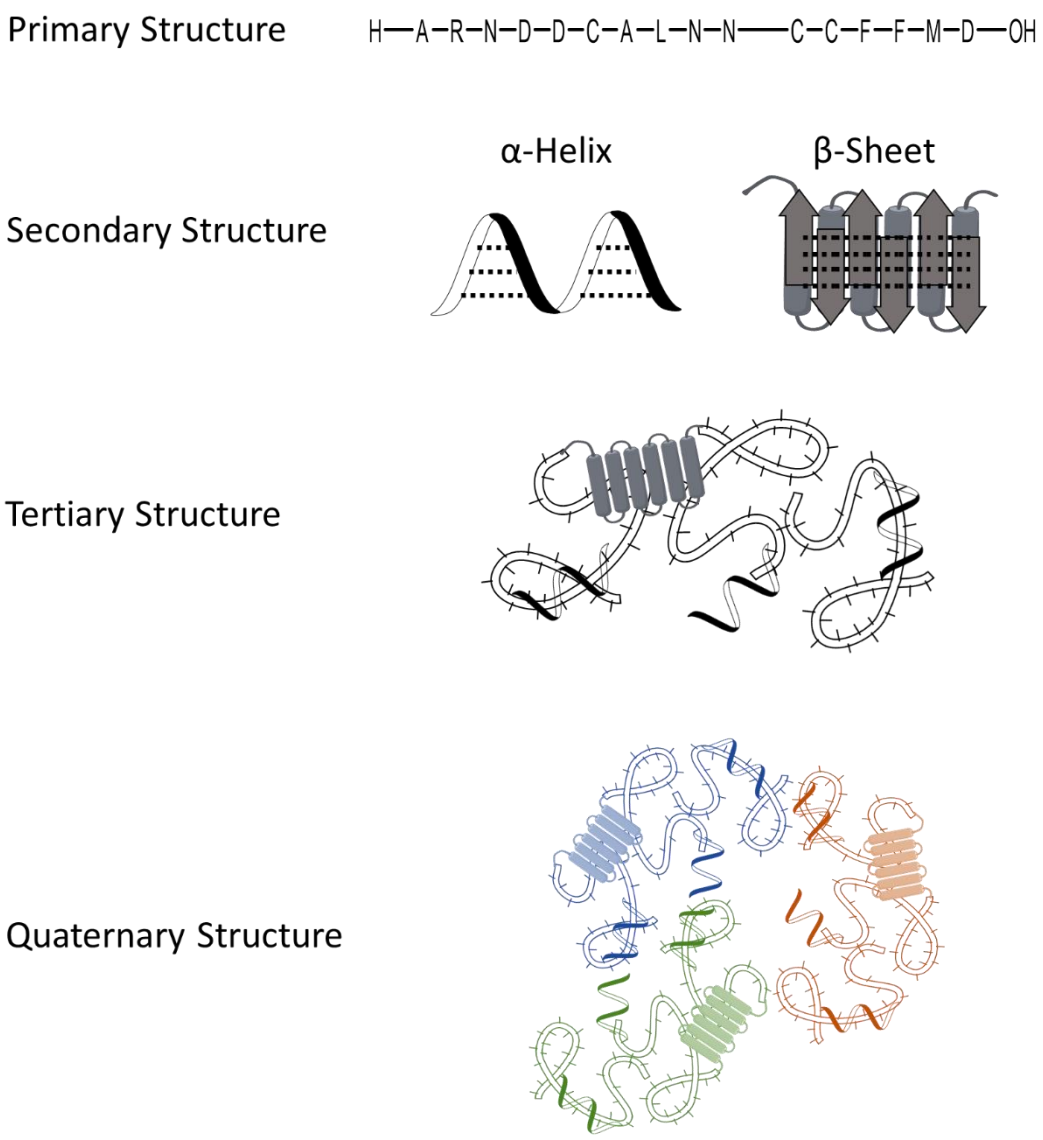

Figure 18: Schematic of protein structuring hierachy[40].

The key peptide stretch that can be observed with FTIR is referred to as the amide 1 stretch, which is the carbon to nitrogen (or amide bond) between the individual amino acids in the main peptide chain (Figure 19). This band in the absorption

spectra, is a combination of multiple stretches and bends, specifically the C=O (~70-80% contribution) and C-N stretch and the N-H bend this measurement can shift in energy depending on the type of secondary structure the peptide has adopted. The hydrogen bonds one amino acid to another depends on the secondary structure, giving different strains and angles, which in turn affects the stretch of the amide bonds stretch. The stretches frequencies appear at 1648-1655cm^{-1} for an alpha helix, 1630-1636 or, 1690-1693cm^{-1} for a parallel beta sheet, 1630 or, 1645cm^{-1} for an anti-parallel beta sheet and 1656-1660cm^{-1} for a random coil formation. This allows for observation of any changes that occur to the peptide structure once attached to the gold nanoparticles[73–75].

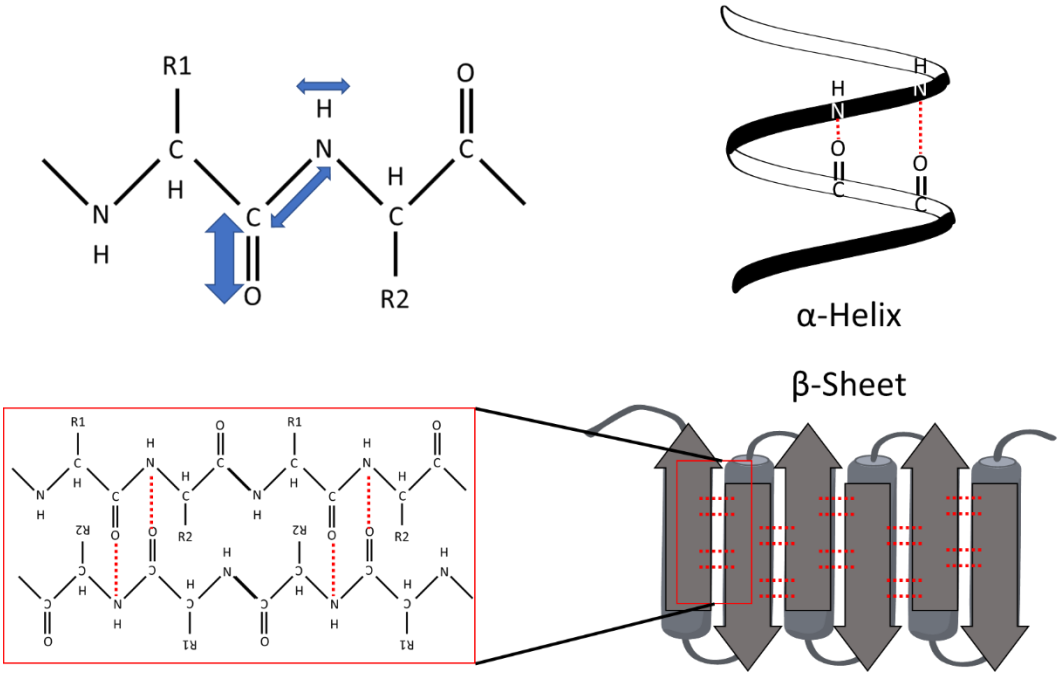

Figure 19: Schematic of the amide 1 band and the stretches and bends that contribute.

Measuring the frequencies of the peptide when attached to gold nanoparticles in solution can be problematic as they are at a relatively low concentration so their spectra tends to be dominated by the particles frequencies instead. Fourier transformation of the spectra is used to overcome this as it has a much larger signal to noise ratio (S: N). This is because of two improvements to the non-transformed Infra-Red spectrometers, firstly the Michelson Interferometer which allows for all frequencies to be measured simultaneously. Simultaneous measurements, eliminates the need for a resolution slit, allowing the full beam to pass through the sample at once thus, improving the S: N by reducing measurement times and allows for multiple scans which when averaged also improves the S: N. Secondly, a mathematical algorithm that uses the complex Fourier series is used to analyse all the data points and separate out the frequencies and average the scans, which greatly increases the S: N[73].

Another issue with determining protein structure using FT-IR spectroscopy is that proteins in their natural state are in the aqueous phase. Water is a very strong absorber with a large absorption band, due to the H-O-H bending mode (1645cm^{-1}), this in the same region as the aforementioned amide 1 band frequencies and as it is more abundant (water being the solvent and the nanoparticles tending to be present in nM concentrations) it dominates the spectra. Although measurements can be taken on a dried sample this usually causes changes to the structure and can even cause complete unfolding to occur. This issue can be addressed by re-dissolving the sample in deuterated water (D_2O), after lyophilisation, to replace all the protons; this will shift the water frequencies (as the D-O-D bending mode is 1215cm^{-1}) so is no longer in the same region as the peptides allowing them to be observed (Table 1).

Secondary structure conformation	H2O solution frequencies (cm-1)	D2O solution frequencies (cm-1)
α-Helix	1653 (s)	1650 (s)
Parallel β-Sheet	1632 (s), 1690 (w)	1632 (s), 1675 (w)
Anti-parallel β-Sheet	1630 (s), 1645 (w)	1632 (s), 1648 (w)
Random Coil (Unordered)	1656 (m, br)	1643 (m, br)

Table 1: Comparison of IR frequencies in different solvents. () are band descriptors, s is strong, w is weak, m is medium and br is broad[76].

The packing density can be calculated using the FT-IR spectra; this is done by first performing a line fit for the amide 1 band to determine its area. This area is then compared to fits done by Chirgadze et.al (1973)[76] that give packing densities for given peptide structures. Finally using the extinction coefficient determined from the UV-Vis spectra of the particles the packing density can be calculated as peptides per nanoparticle. The fitting process was done by Martin Volk and more details are given in our publication[31,77].

1.2.5 - Electron Microscopies

Electron microscopies work on the principle of either passing an electron beam through a sample (transmission) or deflecting it off a sample (scanning) and collating the scattering information and any changes in energy to create an image of the sample.

Theoretical maximum resolution is only ever half the wavelength of the photons used for imaging; so traditional light microscopy can only reach a set resolution, due to the limited and relatively large wavelength of visible light. Below is the equation that shows the relationship between the maximum resolution (d), the wavelength of the photons (λ); and the refractive index (*n*) and maximum half cone (α) of the lens used.

$$d = \frac{\lambda}{2n\sin\alpha}$$

Equation 9: Maximum resolution of light microscopes depend on the wavelength of the photons used.

To increase the resolution of images, electron microscopies were invented as electrons also have wave-like properties where their wavelength is inversely dependent on the kinetic energy of the electron instead; so, the higher energy the electron the more resolution can be obtained. Below is the equation that shows the approximate relationship between the wavelength of the electron (λ_e) and the energy

(E) of the electron; the equation also includes the resting mass of the electron (m_0); the speed of light (c) and Planck's constant (*h*).

$$\lambda_e \approx \frac{h}{\sqrt{2m_0E\left(1+\frac{E}{2m_0c^2}\right)}}$$

Equation 10: The de Broglie wavelength relationship between the wavelength of an electron and the kinetic energy of the same electron[78].

The electron beam is usually created using a traditional tungsten filament (in the case of the SEM it is field emission type) and is focused using magnetic "lenses" towards the sample, down a column, that is under high vacuum; because the electrons can be deflected or absorbed by water molecules within the air before reaching the sample hence decreasing the resolution. When the electron reaches the sample it either passes through a thin section of sample or is deflected and the resultant beam is detected and contains information on the electron density, periodicity and phase allowing an image to be created.

The main benefit of electron microscopies is the greatly increased resolution, high-end microscopes can even resolve individual atoms. Some other benefits are that combining EM with fixing techniques can allow the visualisation of snap shots of in situ situations, although this is only a representation of the in-situ measurement. Newer techniques such as 3-view systematically slices and images the sample allowing for 3-dimensional imaging of an entire sample. Figure 20 are images of

chloroplasts taken with a light microscopy (left) and an electron microscopy (right) and scale bars are given for comparison.

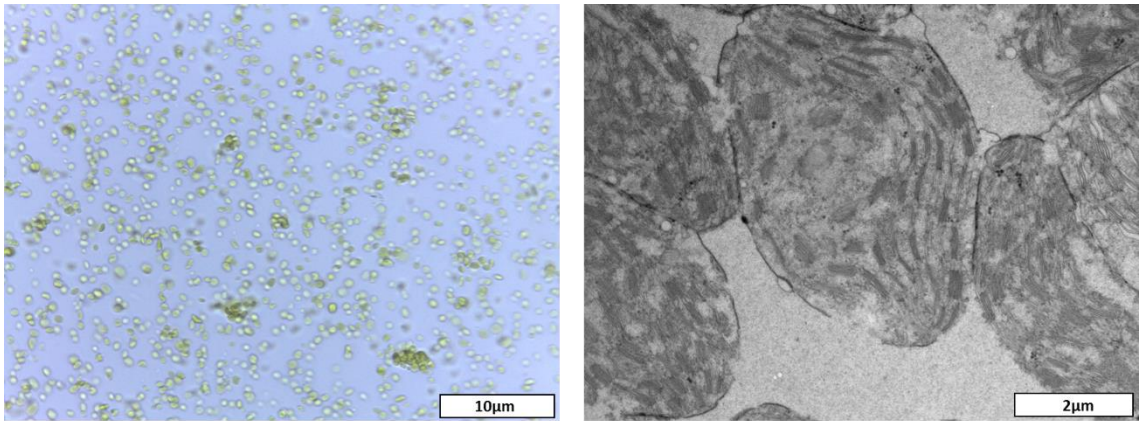

Figure 20: Chloroplast image comparison for light vs electron microscopy.

There are a few drawbacks to using this method as a characterisation technique, most of which are due to the fact that the electron beam can only penetrate through a certain amount of material before a large proportion of the beam is lost, and it is impossible to recover any information from it. Also, atoms with low electron density cannot be imaged with high resolution. Atoms with higher electron density have a greater scattering effect and hence, more information can be obtained. Post staining can aid in increasing the resolution of images of samples with lower electron density. For example, atoms such as carbon, sulfur and nitrogen, which compose most of the biological world, are close in electron density so there is very poor contrast and resolution, especially as grids are often coated in hydrocarbon films. Another problem with this technique, that is shared among microscopies, is that even with

many images of a sample, this is only a narrow selection of the samples distribution and not necessarily a representation of the sample as a whole.

Gold has a large electron density, so EM techniques can achieve high resolution images of nanoparticles. However, their coating layers are either not resolved, or even after post staining, resolved poorly. These images are also not a true measurement of the coating layers as the staining and high vacuum conditions can remove a solvent shell.

1.3 – Biological Principles

As previously stated the second part of the project was to test the DCS on a more practical and complex situation where GNPs are bound to isolated PS1. Then to continue with these systems to build up potential photo-electrodes.

Whilst in parallel particles where functionalised with a chloroplast specific transit peptide with the aim of potentially 'wiring' the chloroplasts for energy generation.

1.3.1 – Photosystem 1

Plant cells, unlike mammalian cells, gain their energy by harnessing the electromagnetic radiation from the sun, this process is performed by chloroplasts and is known as photosynthesis. A chloroplast (Figure 21) consists of a bi layered outer

membrane with internal structures referred to as thylakoids that form stacks. These thylakoid membranes are filled with photosynthetic apparatus that collect and harness solar energy for energy storage.

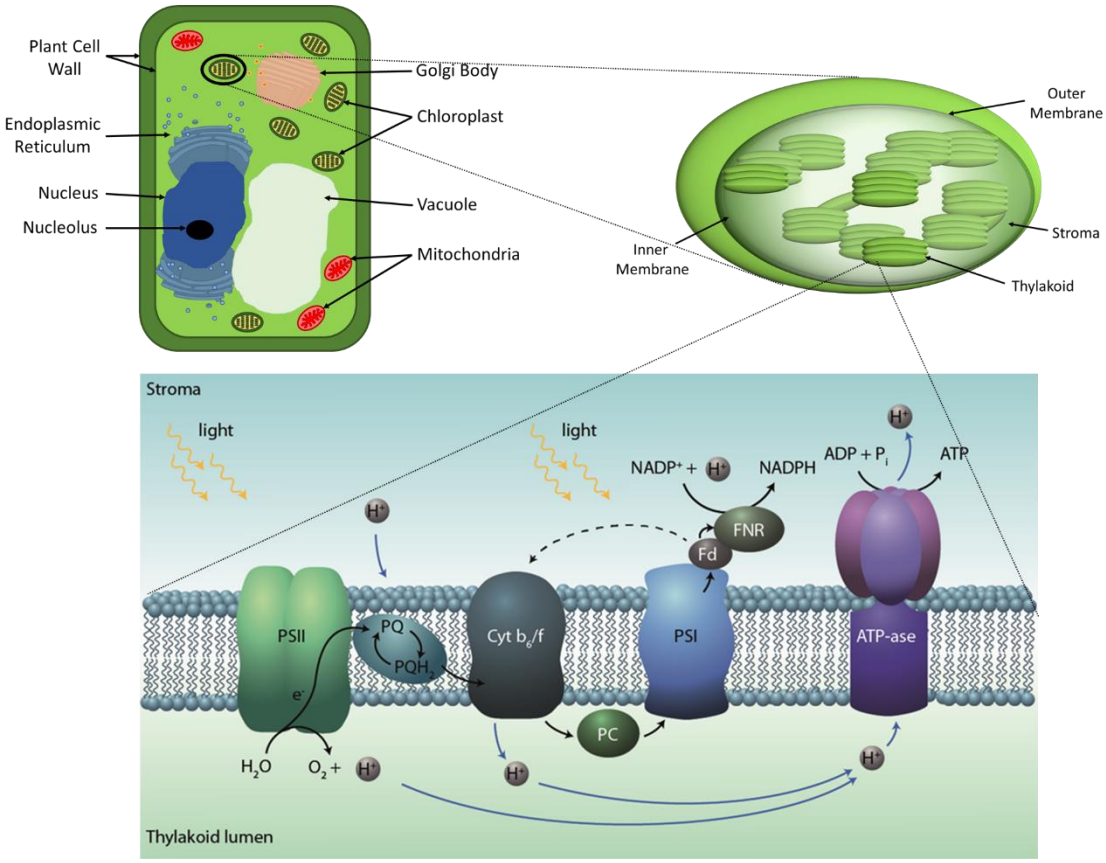

Figure 21: Diagram showing the breakdown of plant cells, to chloroplasts and then the photosythetic apparatus. The Photosynthetic apparatus from left to right is; Photosystem 2 (PSII), Plasto-Quinone (PQ), Cytochrome b6-F complex (Cyt B6F), Plastocyanin (PC), Photosystem 1 (PSI), Ferrodoxin (Fd), Ferrodoxin NADP redtuctase (FNR) and ATP synthase.

This photosynthetic apparatus consists of several components, the first of which is photosystem two (PS2) which begins the photosynthesis process by splitting water to produce oxygen, hydrogen cations and electrons. The electrons produced are then excited by light photons to a higher energy electron state. This then drops in energy

slightly to an electron carrier called plasto-quinone which shuttles the electron through the membrane, to two more shuttles, cytochrome b_6F complex and Plastocyanin, dropping in energy slightly each time. The electron then arrives at the special electron pair, known as P700 (discussed in more detail below) in photosystem 1 (PS1) where it is excited by a second photon. The electron is then given to ferrodoxin, docked in the PS1 which carries the electron to ferrodoxin NADP reductase. This is where the electron is used to reduce NADP to NADPH, for use by ATP synthase to create ATP energy, which is the main source of energy in all biological life[40]. Below is the electron energy diagram for the systems mentioned previously (Figure 22).

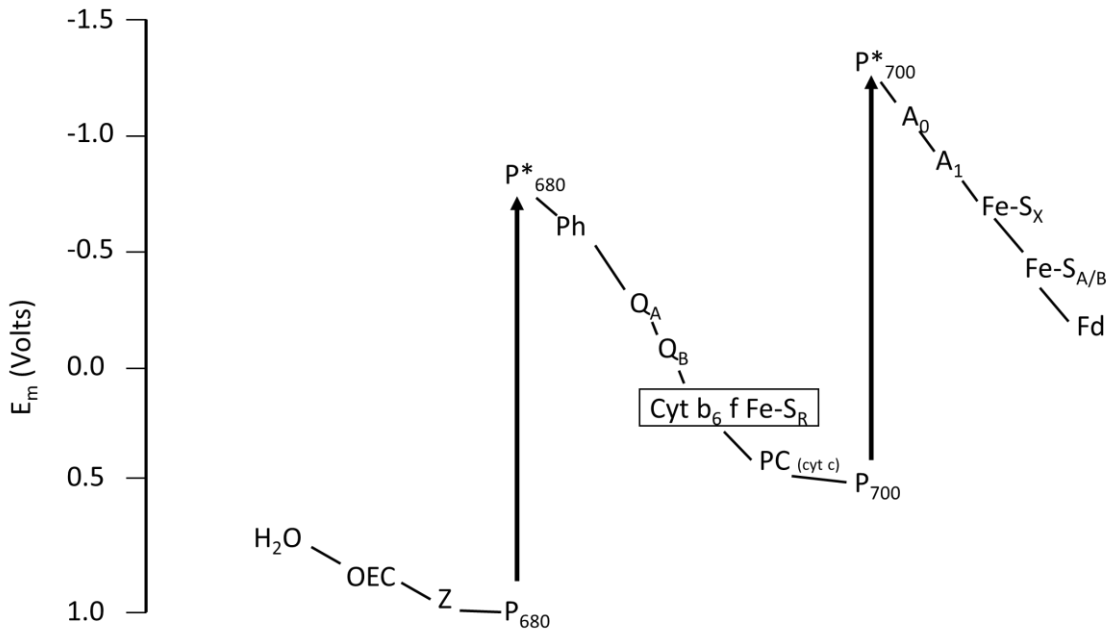

Figure 22: Electron energy diagram for the photosynthetic apparatus. Adapted from R. E. Blankenship 1992[79].

PS1 has a nearly 100% quantum yield due to its ability to separate electrons rapidly over a photo-potential of ~-1V[80]. This is mainly due to the structure providing rapid forward kinetics (~203 pico seconds) with the reverse process being orders of magnitude slower (~ 100 micro seconds)[81]. It has also been shown to have a robust structure, which is maintained even once isolated from the membrane, that is still viable even in dry conditions[82,83]. All these factors make PS1 an interesting structure in the field of photo-electrodes and there has been a wide variety of work and simulations done showing its potential[2,63,84–92].

We propose to use mutated PS1 with the aim of creating ordered multilayers of alternating GNPs and PS1 on top of an electrode to get an enhanced current.

1.3.2 – Plant Cell Physiology and Molecular Import

Part of this project aimed to transport GNPs into the chloroplasts in order to bring them into close contact with PS1, which could be used in further experiments, to investigate whether the GNPs can recreate the electron transport chain used in photosynthesis to artificially recreate this process.

There is a large body of work on the use of GNPs in mammalian systems for a wide range of applications, from labelling, tracking and imaging; to various treatments such as photothermal and photodynamic cancer therapies[4–7,51,93,94]. However, these principles have been little applied to the plant world, apart from some immune-gold assays and using plant reducing agents to produce “green” nanoparticle synthesis

methodologies[95–98]. Beyond the fact that nano-technologies have been applied to mammalian cells for much longer, due to the fact that they serve direct medical purposes; a deterrent to applying the work to plant cells is the different outer membrane making the same import methods unlikely to work.

Although chloroplasts have their own DNA and protein transcription centres, they still have genes and protein sequences that have migrated to the main nucleus making import into the chloroplast very important. Chloroplasts therefore have their own import mechanisms, the most common one being the TIC-TOC import mechanism[99]. This mechanism requires a very specific transport sequence to allow for import through the membrane, below is a diagram of the process (Figure 23).

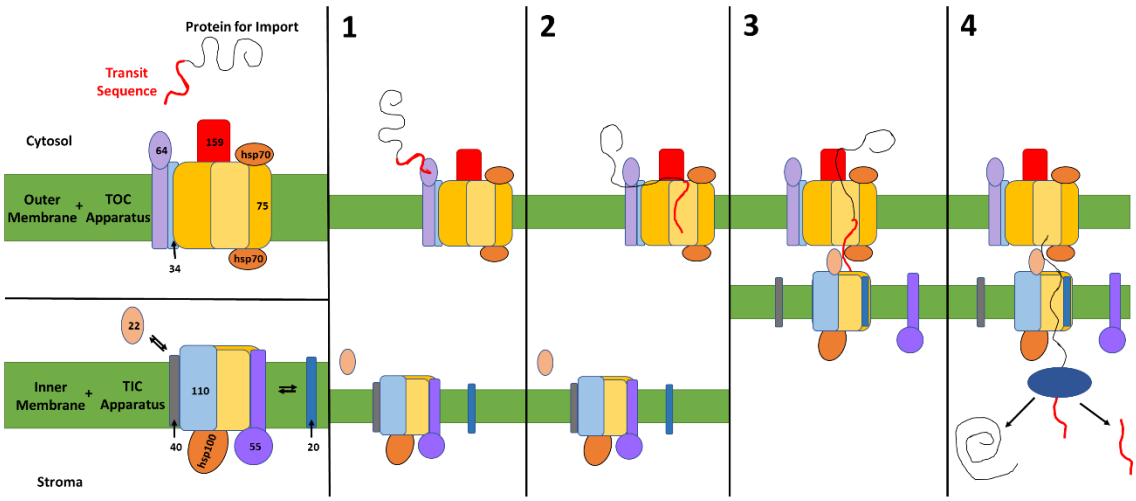

Figure 23:Image showing the TIC TOC mechanism in detail adapted from Image taken from, Toc, Tic, and chloroplast protein import by P.Jarvis, Et.al. 2001[99].

In brief, the Figure 23 above shows the individual TOC and TIC protein complexes (far left of Figure 23) which each contain many smaller proteins, TIC also has two outer

proteins in its complex (protein 40 and 55) that readily and reversible swap with two other membrane proteins (protein 22 and 20). Also shown on the far left of the figure is the protein desired to be imported from the plant cell cytosol, to the stroma inside the chloroplast, which is transcribed with a transit peptide sequence on the end. In step 1, the transit peptide sequence is recognised by protein 64 in the TOC complex. Step 2 shows the protein being unfolded and fed into the TOC channel through the outer membrane and into the inter-membranal space. Step 3, the TIC complex when protein 22 is bound instead of 40 binds to the transit sequence now in the inter-membranal space recognising the sequence; also, the protein 55 has been replace by 20, opening the TIC membrane channel. Finally, in step 4 the protein is passed through the TIC channel to the stroma inside the chloroplast where another protein (cpn60) cleaves off the transit peptide sequence allowing the desired protein to fold into its final shape.

As several of these sequences exist the first step in our experiments was to modify and isolate one such protein and attempt to use this transit peptide to functionalise our GNPs. Proteins modified to have a cysteine group on the terminal end for binding to GNPs has been shown to provide stable GNPs in several cases before[31,74,77]. Also a His-Tag is added to this modification to allow for the use of standard His-Tag purification protocols.

For the initial import experiments, we utilised our transit peptide known to target proteins to the TIC/TOC machinery. This TIC/TOC (translocon on the inside of the chloroplast/translocon on the outside of the chloroplast) machinery is specific to chloroplasts and aids in protein transport both in and out of the chloroplast. The

transit peptide that we attached to GNPs, targets proteins to this TIC/TOC machinery to initiate the transport process. We therefore hypothesised that the peptide would at least move the GNPs into close contact with the transport machinery, hopefully enabling import into the chloroplasts.

Chapter 2

2 – Methods:

All experiments and solutions were made up in Milli-Q ultra-pure water (MQ water) which was made as follows, water was distilled and passed through a long life dual wavelength UV light source to destroy any organics or bacteria via photo-oxidation. The water was then passed through a series of filters and ion exchange resins before dispensing. The resulting water was "Type 1" ultra pure as designated by the ISO (3696) international standards organisation with an approximate resistance of 18.2 MΩ cm and <0.01 CFU/mL of bacteria. All glassware was cleaned between experiments with aqua regia (3:1 HCl:HNO_3) followed by MQ water before use or stored filled with MQ water.

2.1 - Chemicals for Nanoparticle Synthesis

The tetrachloroaurate was purchased in powder form ($HAuCl_4.3H_2O$) from Sigma-Aldrich (≥99.9% purity, PubChem substance ID 24874179) and dissolved in MQ water to make a stock solution of between 0.3-0.5M or as required. The tri-sodium citrate was purchased in powder form ($HOC(COONa)(CH_2COONa)_2 \cdot 2H_2O$) from Sigma-

Aldrich (≥98% purity, PubChem substance ID 24892947) and dissolved in MQ water to the concentration needed and stored for no longer than 2 weeks before use at 4°C). Powder forms of Tannic acid (≥99.5% purity, PubChem substance ID 24865158) and potassium carbonate (99.99% purity, PubChem substance ID 24881291) were both purchased from Sigma-Aldrich.

2.1.1 – Synthesis of 13-15 nm Spherical Citrate Stabilised Gold Nanoparticle

Synthesis of spherical gold nanoparticles was carried out according to a modified version of the Turkevich-Frens[31] method. A solution of tetrachloroaurate (150 mL of 0.333mM made from stock solution, see above) was heated to refluxing temperature in a two-necked round bottomed flask (250 mL), under vigorous stirring to ensure even heating throughout the mixture. Once refluxing, a pre-warmed solution (~65-80°C, on a hot plate) of tri-sodium citrate (1% w/w, 4.5 mL) was quickly added to the round bottomed flask via the second neck; to reduce the Au (III) atoms to Au (0) as previously discussed. This solution was then left to reflux for 30 minutes, transitioning through the following standard colour changes: immediately from pale yellow to colourless; approximately 1 minute black in colour and then lightening to ruby red over approximately 10 minutes. The solution was then cooled to room temperature before filtering any aggregated gold and debris using fluted Whatman filter paper.

The particles are stored at 4°C to extend their "shelf life" and were used before any signs of instability or aggregation.

2.1.2 – Synthesis of 9-11 nm Spherical Citrate Stabilised Gold Nanoparticle

This synthesis was similar to section 2.1.1, with the following minor modifications: the round bottomed flask was 500 mL; the tetrachloroaurate solution concentration varied (0.01M and 200 mL); the concentration of the tri-sodium citrate solution (40mM, 20 mL); and the reduced Au solution was refluxed for 1 hour.

2.1.3 – Synthesis ~5 nm Spherical Citrate and Tannic Acid Stabilised Gold Nanoparticle

This synthesis was carried out according to the method set out by V. Puntes et.al[35]. A solution of tri-sodium citrate (2.2mM, 150 mL) containing potassium carbonate (K_2CO_3, 150mM, 1 mL) and Tannic acid (2.5mM, 0.1 mL) was made and vigorously stirred at exactly 70°C using a thermostatically controlled hot plate and an oil bath, in a two necked 250 mL round bottomed flask with a reflux condenser attached to prevent any significant changes in concentration during the experiment. Once at 70°C this temperature was maintained for at least 10 minutes, tetrachloroaurate (25mM,

1 mL) was then added to the round bottomed flask via the second neck in one quick injection. The solution was then left for at least 15 minutes to allow the complete reduction of the gold. Next 55 mL of the solution was removed and the same volume of tri-sodium citrate (2.2mM) was added, the solution was then allowed to heat back up to 70°C. After the temperature had been reached and maintained for approximately 10 minutes, an injection, via the second neck, of tetrachloroaurate (25mM, 0.5 mL) was added After a further 10 minutes, a second injection of 0.5 mL tetrachloroaurate was added. These particles were stored at 4°C and had to be functionalised within 24–48 hours as they are unstable in this form.

2.2 – Chemicals for Nanoparticle Functionalisation

Various Poly-Ethylene Glycols (PEG) were ordered from ProChimia as oils and were dissolved to approximately 0.1M concentration stock solutions in methanol and stored at 4°C (all PEGs were 11 carbon repeats long and either 4 or 6 ether repeats ending in either an alcohol or a carboxylic acid group). Short chain peptide with amino acid sequence CALNN was purchased as a lyophilised powder from Peptide Synthetics, a subsidiary of Peptide Protein Research Ltd; this was dissolved in MQ water to the desired concentration stock solution for the experiment (usually 1 mg/mL, 1.88mM for all functionalisation experiments). A short chain peptide with the sequence CALNNTAT (the TAT sequence of amino acids is GRKKRRQRRRPQ) was also purchased from Peptide Synthetics and a stock made using MQ water (0.5mM stock solution). The transit peptide was prepared and purified by myself, in collaboration

with Copenhagen University Plant and Environmental Sciences department (please see method in section 2.8.2 - Transit Peptide Purification). The 4-Mercaptophenol was purchased from Sigma-Aldrich (97% purity, PubChem substance ID 24879829) as a powder, which was dissolved in MQ water to the desired concentration for the experiment (0.1 or 1M). The sodium hydroxide was also purchased from Sigma-Aldrich (≥98% purity, PubChem substance ID 57652336) as pellets, which were dissolved in MQ water to the desired concentration for the experiment (0.1 or 1M).

2.2.1 – Gold Nanoparticle Functionalisation with PEG's

The concentration of the citrate stabilised gold nanoparticle solution was calculated using the absorbance from UV-Vis spectroscopy and the desired quantity measured into a sample vial. Then an aliquot of PEG was added to the vial, equivalent to 10 times the molecules of PEG per particle required to form a complete ligand shell. The sample vial was then left for a minimum of 3 hours but usually overnight to ensure full exchange with the citrate.

Particles were then centrifuged (15,000 rpm, 5^{o}C for ~40 mins, or until supernatant was clear) and re-dispersed in MQ water, this wash was repeated at least three times to remove any excess PEG and the displaced citrate. The particles were then concentrated using the same centrifugation process, a test sample with an approximate absorbance of 1 was analysed with UV-Vis to verify ligand exchanged had occurred (using the shift in plasmon resonance). The sample was then stored at

4°C and should be stable for over 12 months. All samples used in this thesis were used within 12 months of functionalisation. Before creating any sample dilutions, the sample was mixed thoroughly.

2.2.2 – Gold Nanoparticle Functionalisation with CALNN and CALNN-TAT Peptides

The citrate stabilised gold nanoparticle solution concentration was calculated using the absorbance from UV-Vis spectroscopy and the desired quantity measured into a sample vial. For the CALNN functionalisation, either 0.1 or 2mM of CALNN (depending on the experiment) was added to the sample vial and left overnight to ensure full exchange with the citrate. For the CALNN-TAT (TAT sequence GRKKRRQRRRPQ) functionalisation an aliquot of mixed capping ligand was added to the vial, equivalent to 10 times the molecules of capping ligand per particle required to form a complete ligand shell; this addition was 5% CALNNTAT and 95% short chain PEG ending in OH.

For both, the particles were then centrifuged (15,00rpm, 5°C for ~40mins, or until supernatant was clear) and re-dispersed in MQ water a minimum of three times to remove any excess peptide and the displaced citrate. The particles were then concentrated using the same centrifugation process and a test sample with an approximate absorbance of 1 was analysed with UV-Vis to verify ligand exchange had occurred (using the shift in plasmon resonance). The sample was then stored at 4°C

and as with the other functionalised particles were used within 12 months. Before creating sample dilutions, the sample was mixed thoroughly.

2.2.3 – Gold Nanoparticle Functionalisation with Chloroplast Transit Peptide

The final iteration of the method is given below, and the optimisation of this process is discussed in more detail in the relevant results chapter (5.2.2 – Chloroplast Extraction and Nanoparticle Import). The citrate stabilised gold nanoparticle solution concentration was calculated using the absorbance from the UV-Vis spectroscopy and the desired quantity measured into a sample vial. For each functionalisation, an aliquot of mixed capping ligand was added to the vial, equivalent to the number of molecules of capping ligand per particle required to form a complete ligand shell. This addition was done for 1, 5 and 10% transit peptide with the counter-part being 99, 95 and 90% respectively of short chain PEG ending in OH. These samples did not require any washing so were ready to use immediately after synthesis.

The samples were made as close to the transport study as possible to prevent possible aggregation and were stored at 4^{o}C. The samples were analysed using UV-Vis spectroscopy to determine if any aggregation had occurred and to verify that ligand exchange had occurred. Before using the samples, they were sonicated for a few seconds to ensure they were fully dispersed.

2.2.4 – Gold Nanoparticle Functionalisation with Mercapto-phenol

The citrate stabilised gold nanoparticle solution concentration was calculated using the absorbance from the UV-Vis spectroscopy and the desired quantity measured into a sample vial. The pH of the particle solution was adjusted to 11 using sodium hydroxide (NaOH; 1mM) before adding an aliquot of mercapto-phenol to the vial, equivalent to 10 times the molecules of mercapto-phenol per particle required to form a complete ligand shell. The sample vial was then left for a minimum of 3 hours, but usually overnight to ensure full exchange with the citrate.

The particles were then centrifuged (4,000 rpm, 5^{o}C for ~75mins, or until supernatant was clear) and washed in 1mM NaOH, to ensure the pH remained at 11, a minimum of three times to remove any displaced citrate. The particles were then concentrated using the same centrifugation process. A test sample with an approximate absorbance of 1 was analysed with UV-Vis to verify ligand exchanged had occurred (using the shift in plasmon resonance). The sample was then stored at 4^{o}C and was used within 12 months. Before creating sample dilutions, the sample was mixed thoroughly and re-dispersed in the relevant hydroxide electrolyte ensuring the sample was always pH 11.

2.2.5 – Gold Nanoparticle Functionalisation with Photosystem 1

The citrate stabilised gold nanoparticle solution concentration was calculated using the absorbance from the UV-Vis spectroscopy and the calculated quantity needed to provide a 1:1 ratio with the photosystem 1 was measured into a sample vial. An aliquot of n-Dodecyl β-D-Maltoside (β-DM, 1% w/w solution, purchased from Sigma-Aldrich, PubChem substance ID 24893890) was added to a final concentration of ≥0.1% w/w. The solution and all relevant equipment was then transferred to a dark box containing a green lamp for the next steps. An aliquot of the desired photosystem was thawed and pipetted into the solution, the aliquot container was rinsed out with 500 µl of MQ water to collect any residual liquid and the solution was mixed and kept in the dark till use.

2.3 – UV-Vis Measurements

UV-Vis measurements were made using a GENESYS ^{TM} 10S UV-Vis spectrophotometer purchased from ThermoFisher Scientific. All samples were diluted to an approximate absorbance value of 1 before measuring the sample in the absorbance window of 300-900 nm, as the area of interest is usually between 400-800 nm, thus ensuring nothing of interest is missed.

2.4 - Centrifugal Particle Sizer Standard Setup

The machine used was a Centrifugal Particle Sizer, CPS model DC24000, provided by CPS instruments inc. The blunted needles and disc closures were all provided by CPS instruments inc, as well as the PVC standard of known size (127 nm). The machine was cleaned, and gradient solutions were made up with MQ water. The sucrose was purchased in powder form from Sigma-Aldrich (≥99.5% purity, PubChem substance ID 57652987), the dodecane was also purchased in liquid form from Sigma-Aldrich (≥99% purity, PubChem substance ID 57648398). The machine was cleaned with ethanol from a drum solvent and Kimwipes ® disposable wipers (L x W 15 in x 17 in), this ensured that the disc was not scratched during cleaning. The plastic Pasteur pipettes (3 mL) used to drain the disc during cleaning (plastic pipettes prevent the disc from being scratched whilst also allowing for them to be inserted through the disc closure) where purchased from STARLAB.

Before experiments, the CPS machine was cleaned thoroughly as follows: (this procedure was defined by CPS instruments inc) the disc closure was removed and the disc was filled to the opening with MQ water, the disc was then spun and allowed to stop in both directions before the water was removed using a plastic Pasteur pipette (3 mL), into a waste container. The process was repeated twice over with MQ water before repeating 3 times with ethanol. A tissue was folded into a thin strip and soaked in ethanol before being fully inserted into the disc and run around the inside at least one full revolution; this process was repeated until the tissue has come out clean twice. The disc was then dried with a clean tissue to pick up any residual ethanol that

has not evaporated. The disc closure was then returned and the centrifuge was sealed. Cleaning is a very important step to ensure that the centrifuge remains balanced, as ultracentrifuges run at high speeds so if they become unbalanced it is very dangerous.

Two sucrose solutions were made up: 24% w/w sucrose solution containing 6 g of sucrose, made up to 25 g in weight using MQ water (all weighing was conducted on a 5 figure balance to 0.001 of a gram); 8% w/w sucrose solution containing 2 g of sucrose, also made up to 25 g in weight using MQ water.

The first sucrose gradient step (see Table 2) was injected into the disk after its closure, using a syringe (2 mL) and a specially blunted needle (this prevents the disc from being scratched or damaged), and the machine was turned on and the speed set to the desired value in the machine software. The machine was then allowed to reach full speed before any further steps. Both solutions were loaded into the needle at volumes recorded in Table 2, these were then mixed in the needle and any bubbles ejected (drawing up the sucrose slowly prevents the formation of bubbles). The sucrose mixtures were then injected in the order noted in Table 2. The last injection was dodecane (0.5 mL).

8% Sucrose Solution (ml)	24% Sucrose Solution (ml)
0	1.6
0.2	1.4
0.4	1.2
0.6	1.0
0.8	0.8
1.0	0.6
1.2	0.4
1.4	0.2
1.6	0
Dodecane	0.5

Table 2: Sucrose Gradient Injection Steps

Once the gradient had been built it was allowed to settle for a minimum of 15 minutes enabling the distinct layers to blend and a smooth density gradient to be formed. The gradient was tested by three consecutive runs of PVC of a known size. Once three concordant runs had been achieved, the gradient was ready for measurements. The sample was measured by first running the known sample of PVC to set variables (see 1.2.3 - Differential Centrifugal Sedimentation section for more details) followed by running the sample (following on screen instructions), this process was repeated until 3 concordant results were obtained.

Once the measurements were completed, the machine was stopped and excess fluid was removed by bending a plastic Pasteur pipette through the injection hole in the

disc closure, once the liquid level dropped below the disc closure, the closure was removed and cleaned following the protocol described previously.

2.4.1 – Centrifugal Particle Sizer Electrolyte Gradient

The following electrolytes were used for these experiments and were all purchased from Sigma-Aldrich and dissolved in MQ water. Lithium hydroxide, purchased as a monohydrate powder, purity 98.5%, PubChem substance ID 24896373. Sodium hydroxide, purchased as pellets, purity ≥98%, PubChem substance ID 57652336. Potassium hydroxide, purchased as powder, purity ≥99.97%, PubChem substance ID 329766684. Cesium hydroxide, purchased as powder, purity ≥99.95% purity, PubChem substance ID 24873911. Lithium perchlorate, purchased as a powder, purity ≥99.99%, PubChem substance ID 24867030. Sodium perchlorate, purchased as a monohydrate powder, purity ≥99.99%, PubChem substance ID 24863796. Potassium perchlorate, purchased as a powder, purity ≥99.99%, PubChem substance ID 24869702. Cesium perchlorate, purchased as a powder, purity ≥99.995%, PubChem substance ID 24880702. Lithium chloride, purchased as a powder, purity ≥99%, PubChem substance ID 24278056. Sodium chloride, purchased as a powder, purity ≥99.5%, PubChem substance ID 24899759. Potassium chloride, purchased as a powder, purity ≥99%, PubChem substance ID 24899027. Cesium chloride, purchased as a powder, purity ≥99.999%, PubChem substance ID 24852140. Sodium iodide, purchased as a powder, purity ≥99.999%, PubChem substance ID 24865632.

For the electrochemical double layer experiments, the sucrose was dissolved in pre-made electrolyte solution at equal concentration to the electrolyte present in the sample being analysed.

2.4.2 – Centrifugal Particle Sizer Protein Gradient

The BSA was purchased from Sigma-Aldrich, purity ≥98%, heat shocked fraction and pH 7, the BSA was in crystal form and was dissolved in MQ water.

The non-equilibrium/ chemisorbed samples were measured as stated in the previous section 2.4 - Centrifugal Particle Sizer Standard Setup. For the equilibrium samples, the sucrose was dissolved in pre-made BSA solution at the same concentration as the sample.

2.5 – Electron Microscopy

TEM images were obtained using the FEI Tecnai set to 120kV using the Tecnai Analysis program. SEM images were obtained using the FEI Quanta 250 FEG-ESEM, the beam setting varied and is noted on the individual images and was dependent on the substrate and humidity.

2.5.1 – Nanoparticle Preparation for Electron Microscopy

For TEM, the sample was diluted to an approximate SPR absorbance of 1 and then 10 µl of the sample was pipetted onto a copper TEM grid 100 mesh coated in either PVP or carbon coated PVP (purchased from Agar scientific and either coated with PVP if bare or used as bought if coated in carbon). The grid was then left to dry on filter paper before being stored in a labelled grid box for analysis. This method was also used for SEM but particles could also be pipetted on to a highly ordered silicon wafer and left to dry using the same method as the TEM grid.

2.5.2 – Negative staining of sample for Transmission Electron Microscopy

Given below is the optimised staining procedure, but a variety of times for the staining steps were used and the exact conditions for staining are given with each image. After a sample had been placed on to a grid and the grid was dry it could be post-stained. The staining was done in as low light intensity as possible and the stain was covered by a light blocking lid whenever they were not in use. A piece of parafilm was stuck to a plastic surface using water and the staining and washing droplets set up in order. The stains used were filtered through 0.22 µm syringe filters and centrifuged (using a bench top centrifuge at 5000 g for 2 minutes) to remove precipitant before use; 4% uranyl acetate in MQ

water, 4% Reynolds lead citrate in MQ water (both purchased from Agar Scientific, pre-made and stored at 4^{o}C and used within a few months). The grid was placed sample side down on top of the uranyl acetate droplet using forceps, and left for 2 minutes before transferring to a MQ water droplet for a few seconds.; after which the grid was transferred to the Reynolds lead citrate droplet for 2 minutes. Finally, the grid was transferred for a few seconds to a MQ water droplet before putting on filter paper to dry sample side up; the grid was then put in a labelled grid box till analysis.

2.5.3 – Fixation and staining of Chloroplast samples for Transmission Electron Microscopy

Every step of the fixation was done wearing gloves and in a fume hood following the required COSHH procedures. Karnovsky's fixant was prepared fresh on the day of fixing as follows: 1 g paraformaldehyde, purchased from Sigma-Aldrich as a reagent grade powder (PubChem substance ID 24898648) was dissolved in 13 mL of MQ water and stirred at 80^{o}C till fully dissolved. Approximately 2 drops of 1M NaOH was added to the solution causing it to become clear; then cooled to room temperature before the addition of 5 mL of glutaraldehyde (25% w/w, stored at 4^{o}C and used as purchased from Sigma-Aldrich, PubChem substance ID 24895235). The solution was then made up to 25 mL using 0.3M pH balanced sodium cacodylate buffer. Sodium cacodylate buffers of the following concentrations were pre-made: 0.1, 0.2 and 0.3M

solution made up in MQ water and pH balanced to 7.3, before being kept at 4^{o}C till use, purchased from Sigma-Aldrich as a tri-hydrate powder, purity ≥98%, PubChem substance ID 24892742.

Spur's resin was either defrosted from the freezer if under 1 month old or made fresh on the day as follows. All products required for the resin were liquids and purchased as an embedding kit from Sigma-Aldrich: 10 g epoxy resin (ERL 4221); 8 g Diglycidylether of polypropylene glycol (DER 736); 25 g Nonenyl Succine Anhydride (NSA). These three components were mixed thoroughly, ensuring no bubbles form, before the addition of 0.3 g of Dimethylaminoethanol (DMAE). All pipettes used to measure out the liquids were heated in an oven to cure any residual resin before disposal.

The sample to be fixed was pipetted into a small glass vial using cut off pipette tips and mixed gently into 0.5 mL of Karnovsky fixant before rotating for 2 hours. After the plant material and fixant were transferred to an Eppendorf® tube and centrifuged, using a bench top centrifuge at 5000 g for 2 minutes. The supernatant was removed and the pellet re-dispersed in 1 mL of 2% agarose, and then pipetted into a pellet mould and allowed to cool until set. The agarose pellet was then cut into small chunks, approximately 2 mm cubes, using a scalpel before putting into a fresh small vial with enough sodium cacodylate buffer (0.1M) to cover the sample and rotated for 20 minutes. The buffer was removed and replaced with fresh 0.1M sodium cacodylate and rotated for a further 20 minutes.

Next, the buffer was swapped for a staining agent made as follows; a 2 mL ampule of osmium tetroxide (OsO_4, purchased from Sigma-Aldrich, PubChem substance ID

57654490) was opened and added to a sample vial containing; 2 mL of MQ water and 4 mL of 0.2M sodium cacodylate, creating a final solution containing 2% osmium tetroxide. The sample vial was then left coated in the stain for 2 hours on a rotor. The waste osmium tetroxide solution had vegetable oil added to it and the entire vial disposed of in the dedicated osmium waste. The sample was washed twice with 0.1M cacodylate and then twice with MQ water, each wash rotating for 10 minutes. After the washes the sample was dried with 20 minute incubations of: 30% acetone (all the counterpart factions are MQ water); 50% acetone; then 70% acetone overnight in the fridge.

The next day the sample was further dried with 20 minute incubations in 90% acetone and then 100% acetone twice. Next, the sample was incubated for 30 minutes each time on the rotor, in the following ratios of spur resin: 100% acetone; 1:3, 1:1 and 3:1. The sample was then incubated for an hour in 100% spur resin with no lid on to ensure that all acetone evaporated; the incubation was repeated with 100% resin but a closed lid, then it was swapped for pure resin again and left overnight. The next day the resin was swapped once more and left on a rotor for 1 hour. The sample was then placed into pellet moulds containing spur resin, ensuring one cutting per mould, the sample was fully submerged and as close to the top of the pellet as possible. The moulds were then placed in the oven at 60^{o}C for 8 hours and then placed in labelled bags ready for analysis.

2.5.4 – Resin block cutting and preparation for Transmission Electron Microscopy

Singular resin pellets were fixed into a sample holder, the top was then trimmed under a microscope with a razor and the edges trimmed so that the sample block cross section was the foremost part of the pellet. The sample holder was then transferred to the Leica EM ultracut UC6, ultramicrotome instrument and fixed in place. A freshly made glass knife was made (A new glass knife was used after 2 sides of the cross section were cut) and used to cut a 350 x 350 µm cross section of the sample using these conditions; speed of 100 mm/s and a 1000 nm feed per slice, the cross section is 230 µm deep.

A clean (with MQ water), dry diamond knife (diatome ultra 45^{o}) set to a 6^{o} angle, was fixed into place and the 'boat' filled with MQ water, enough to create a flat surface with the knife edge which is standard protocol to obtain slices (which are lifted from the water level after slicing). For precision, the automated machine is set to slow the cutting mechanism by setting a cutting window to just above and below the sample block ensuring these sections are cut smoothly. To section the sample the speed was set at 1 mm/s and feed per slice set at 70 nm. Around 10-20 slices were cut before the process was stopped, then a Q-tip soaked in chloroform was held slightly above the slices to stretch out any wrinkles in the slices caused during slicing, afterwards using forceps a grid was slid underneath the sections to place them on the grids. The grids and sections were left to dry on filter paper and then put into a labelled grid box until staining and analysis; approximately 3-6 grids per sample were prepared.

2.5.5 – Sample preparation for Cryo - TEM

Samples for cryo-TEM were prepared by pipetting approximately 10 µl of particles onto a holey support film carbon grid (purchased from Agar scientific) freshly glow-discharged using argon plasma. After 60 seconds of incubation, the grids were quickly blotted on each side twice for 2 seconds and instantly plunged into a liquid ethene bath freezing the sample in a thin layer of amorphous ice (this process was done using an FEI Vitrobot Mk2 system, working at >96% relative humidity). The frozen samples were transferred onto a cryo-holder (626 Gatan cryo-holder) with a small liquid nitrogen tank to keep the holder and sample chilled. The sample was then imaged using the same machine and the same settings as previously discussed.

2.6 - Fourier Transform Infra-Red sample preparation and measurement

Samples were prepared for FT-IR by first concentrating and cleaning the samples after functionalisation as previously described. For the peptide control samples, a concentrated peptide solution (0.1mM) was made. The sample was first dialysed in ≥1 L of MQ water on top of a magnetic stirrer plate, in a magnetic spin dialyser chamber (volume approximately 2 mL, purchased from Havard apparatus) with dialysis membranes at either side of the chamber (10 kDa cut off, purchased from

Havard apparatus) the water was changed after approximately 8 hours and the process repeated twice. The sample was then flash frozen using liquid nitrogen and put under vacuum with a hole in the Eppendorf tube (1.5-2 mL) lid to allow for lyophilisation to occur, the sample was usually left overnight (~12 hours). The sample was kept in powder form in the lyophilisation chamber until ready to be analysed. After lyophilisation, the sample is re-dispersed in deuterated water (1 mL, purchased from Sigma-Aldrich, purity of atoms 99.9% Deuterium, PubChem substance ID 24849176, this was purchased as a liquid and kept in a glove box under argon atmosphere until needed), this process is repeated at least once more.

The FT-IR sample holder and windows (KBr) are cleaned thoroughly using ethanol before and after every sample. Once the sample was ready to be analysed it was re-dispersed in D2O (50 µl) and a 25 µl sample was pipetted into an FT-IR cell with a 25 µl spacer between the windows before being sealed. The FT-IR machine was prepared by cooling the detector with liquid nitrogen for at least 1 hour before the start of measurements. A background scan was run of the dry atmosphere inside the sealed FT-IR for a minimum of 1000 scans, followed by a short test of 5 scans for comparison to ensure there was no significant deviation from the background.

The sample cell was inspected for any aggregates or bubbles and was positioned between the light source and detector in such a way to avoid any of the aggregates or bubbles if they were present. After the sample had been put in the machine and the hatch sealed, the chamber was left for a minimum of an hour to remove any residual water before a measurement of the sample was conducted with 1000 scans.

The remaining 25 µl was used to run a UV-Vis spectrum for approximate concentration comparisons.

2.7.1 - Solid Medium Cell Culture Plates

The following protocol was conducted in a high flow-through sterile cell culture hood, cleaned with 70% ethanol solution before and after use and the LB-Agar bottle was never opened outside the cell culture hood. Premade LB-Agar gel (pre-prepared by the collaborators lab technician from powders purchased from sigma Aldrich; Bacteriological Agar (15 g) and Lysogeny Broth (LB), LB broth (Miller) (20 g), were mixed and made up to a litre with MQ water and set) was melted with a microwave (above 72^{o}C) and then allowed to cool to 55^{o}C before addition of the antibiotic, Ampicillin. (this needs to be below 60^{o}C, so the antibiotic is not denatured but above 40^{o}C to keep the agar liquid and is determined using an electronic thermometer: The Ampicillin stock concentration is 50 mg/mL and was provided by our collaborators and was stored at -18^{o}C). The final concentration of ampicillin in these plates was 50 µg/mL. The LB-Agar was then poured into Petri dishes (10 cm diameter) to give an approximately 0.5 cm even layer on the bottom; a few dishes were poured before addition of the antibiotics to be used as a control. The plates were allowed to set and could be sealed in a sterile bag, tied in the cell culture hood before being stored at 4^{o}C for up to 2 weeks before use.

2.7.2 - Transit Peptide Transfection into *Escherichia Coli*

All empty Eppendorf tubes, and chemicals were kept on wet ice during thawing and preparation.The competent *Escherichia Coli* (E.Coli) (provided by Copenhagen collaborators, cell line BL21(DE3)) was stored in a cryogenic -80^{o}C freezer until use. One 100 µL aliquot was thawed for use and pipetted gently before being split equally into two tubes and labelled as control and transfection sample. The expression plasmid (PET 15b -TP-His-Cys, purchased from Eurofins genomics, 1µl, with a 83.5 ng/µl concentration of plasmid measured by collaborators using a nanodrop) was added to the transfection sample (using a 1µl maximum sized micro-pipette) and stirred gently with the pipette tip before being returned to the ice bucket for 2-3 minutes to allow for the system to equilibrate. The cells with the plasmid were then heat shocked by heating at 42^{o}C for 45 seconds and then immediately returning to the ice for 2 minutes.

The following steps were conducted in a high flow-through sterile cell culture hood, cleaned with 70% ethanol solution before and after use. Also, any steps that involved work with bacterial cultures were also performed under these sterile conditions.

To the cells, 200 µl of LB was added and then placed on a shaker in an incubator at 37^{o}C for 30 minutes to start growth and recovery. For the control sample, 100 µl of competent cells were pipetted directly towards one outer edge of two petri dishes, one with ampicillin and one without. For the plasmid containing cells, three ampicillin dishes were prepared and 150 µl of LB added to each at one edge of the dish and then 5, 50 or100 µl of cells were pipetted into these droplets. 50 µl of cells in a 150

µl LB droplet were pipetted onto a singular dish with no antibiotic as a further control. All cells were spread across the plates using the following procedure, an inoculation loop (purchased from Bio-Rad laboratories Inc) was placed flat against the LB-Agar and spread across the surface evenly. All the dishes were then placed in an incubator at 37^{o}C and left overnight.

The following day the plates were checked for growth and colonies approximately counted. Polymer chain reaction (PCR) tubes were prepared each containing; deoxynucleotide triphosphates (dNTPs, 1 µl), designed primers for the forward and reverse ends of the peptide expression area (0.5 µl of each), buffer containing magnesium chloride ($MgCl_2$, 4 µl), Taq Phusion polymerase (0.1 µl), MQ water (13.9 µl); all of these items were purchased as part of a kit for PCR from ThermoFisher Scientific.

Using a fresh inoculation loop, a scraping was made of one colony from each of the controls and at least 6 colonies from the best growing plasmid plate and the colony labelled underneath the petri dish with a circle. Colonies with satellite colonial growths were avoided in case of contamination with non-plasmid bacteria. The selected colonies were streaked across one third of an Agar plate (containing ampicillin) with the loop flat against the surface in a decreasing zig-zag pattern from the outer edge to the centre. The streaked LB-Agar plates were then put into the incubator (37^{o}C) and the old dishes were sealed and put into the fridge for later analysis if needed. A small amount of each of these colonies was mixed into the prepared PCR tubes. The PCR tubes were then put into a PCR thermos cycler (model Mastercycler ® nexus purchased from Eppendorf AG) with the following program:

step 1, 95°C for 1 minute; step 2, 95°C for 30 seconds; step 3, 60°C for 30 seconds; step 4, 72°C for 30 seconds; steps 2-4 were then repeated for 30 cycles; step 5, 72°C for 30 seconds; and finally step 6, 4°C permanently until the samples were collected.

A fresh 1% agarose (purchased from Sigma-Aldrich, PubChem substance ID 24891469) gel was poured, from pre-made agarose gel kept liquid in an oven at 60°C, into a gel mold with an 8 well comb. Once the gel had set it was placed into an electrophoresis tray filled with fresh TAE buffer (this buffer was purchased as a premixed solution at 50 times the desired concentration and contains; Tris base 40mM, acetic acid 20mM and ethylenediaminetetraacetic acid [EDTA] 1mM) and into the bottom of the first well was pipetted a DNA ladder, 1 KB plus blue (15 µl, purchased from ThermoFisher Scientific). The PCR products (10 µl) were added to gel red (3 µl, purchased from Biotium) and mixed before being loaded (10 µl) into wells in the gel. The gel was then run at 100 A for 30 minutes using a BioRad Powerpac, with the current running from negative at the top to positive at the bottom.The gel was then analysed to confirm the presence of the plasmid DNA containing the expression vector.

2.8.1 - Transit Peptide Expression

The colony that provided the highest intensity band for the plasmid in the PCR was selected for expression and the relevant streaked LB-Agar plate checked the day after to check for colony growth. A scraping of the streaked plate was taken and added to

a small falcon tub of LB (10 mL) and placed in a shaker at 37^{o}C and left overnight. The next day, the liquid culture was added to an autoclaved larger conical flask with large indentation in the bottom, sealed with foil and one fifth filled with LB containing ampicillin (≥50 μg/mL); which was put on a rapid adhesive stirring plate in an incubator (37^{o}C). Samples were taken at regular intervals after the first hour of incubation and the optical density (OD) of the solution at wavelength 600 was recorded to approximate the concentration of the cells in the culture. This OD is taken to determine when the *E.Coli* have reached the exponential growth stage in their life cycle and will therefore produce a large volume of proteins.

Once the OD600 value was over 0.7, the expression factor Isopropyl β-D-1-thiogalactopyranoside (IPTG, 200 μL) is added to the culture, 5 mL of the mixture was removed and put on ice to serve as a uninduced control. After addition of IPTG, the culture's OD600 was measured every hour until it reached a plateau, at which point a sample was taken for gel electrophoresis analysis to determine the presence of the peptide and the remaining culture was split into several containers and centrifuged (4000 rpm for 15 minutes). The supernatant was discarded as genetically modified organism (GMO) waste and the pellets were flash frozen and at -80^{o}C until needed for peptide purification.

2.8.2 - Transit Peptide Purification

The final iteration of the method is given below, and the optimisation of this process is discussed in more detail in the relevant results chapter (5.2.1 – Production and Purification of Transit Peptide).

First, fresh lysate buffer was made containing, bicine (50mM, purchased Sigma Aldrich, ≥99.9% purity, PubChem substance ID 24891738) and triton X-100 (0.2% w/w, purchased Sigma Aldrich, PubChem substance ID 329826885) adjusted to pH 8 before adding 1,4 – Dithiothreitol (DTT, 10 mM, Sigma-Aldrich, PubChem substance ID 329798930) and kept on ice until needed.

E.Coli pellets were thawed and weighed before dissolving in premade lysate buffer. The lysate was then passed through a cell homogeniser or french press twice at 30 Kpsi (model CF range, from Constant Systems ltd). The lysate was centrifuged at 10000 g for 20 minutes at 4^{o}C to remove cell debris and the supernatant collected.

The peptide was then purified from the supernatant using the ammonium sulphate precipitation method, the following steps were done in the cold room (4^{o}C) to prevent any protein degradation. First ammonium sulphate was added up to 50% saturation (saturation concentration is 3.9M) a few granules at a time ensuring the powder was dissolved before the next addition to prevent any localised high concentrations. The sample was then left to equilibrate for at least an hour in the cold room on a rocker. The sample was then centrifuged (conditions 16000 g, for 20 minutes, at 4^{o}C) and the supernatant collected before centrifuging again under the

same conditions and the supernatant collected. All cell pellets and debris were kept for testing as a control to ensure the peptide had been solubilised. More ammonium sulphate (100% saturated solution) was added stepwise until the percent saturation was brought up to 70%, the supernatant was then left to equilibrate at 4^{o}C for an hour on a rocker. Afterwards, the supernatant was centrifuged twice more (16,000g, for 20 minutes, 4^{o}C) each time collecting the supernatant and saving the cell pellet for later analysis. Then the pellet from the first centrifugation was resuspended in phosphate buffer saline solution (PBS, 250 µl).

The peptide solution was dialysed (approximately 350 µl) in approximately 800 mL of MQ water for at least 1 hour and then the process repeated with fresh water. The samples were then analysed by gel electrophoresis to verify the presence of the peptide in the pellets and supernatant This also determined the presence of other proteins and hence the purity of the sample.

2.9 - Bradford Assay

The chemicals used in the Bradford assay were as follows: various concentrations of sodium chloride and BSA (chemical information given previously); Bradford reagent (purchased from Sigma-Aldrich) used as purchased.

The Bradford Assay is used to determine the concentration of the purified peptide, as the Bradford reagent changes its absorption frequency on binding to the protein so quantification of this can give the concentration.

First a calibration curve was created using a range of BSA concentration (the range used was 0, 250, 500, 750, 1500 µg/mL), in a total volume of 1 mL containing 20 µL of BSA dissolved in 0.15M of sodium chloride and made up to using Bradford reagent. This follows the standard protocol for a Bradford assay for 1 mL samples. All samples made must be left a minimum of 5 minutes (put on a rocker for the duration of this incubation time) to ensure full binding to protein but analysed within 1 hour of addition.

The transit peptide sample was prepared by diluting a sample of the peptide 1:10 with the sodium chloride solution and then added to the Bradford reagent in the same way as control samples. All the data was then plotted, and the transit peptide concentration calculated using the known calibration curve.

2.10 - Gel Electrophoresis

Transit peptide samples were prepared for gel electrophoresis by adding at least 0.3% w/w of BugBuster master mix ® (purchased from Sigma-Aldrich) to a sample of supernatant or a small amount of cell pellet re-dispersed in PBS (1-2 mL). The samples were put on rocker at room temperature for 10-20 minutes. Afterwards, the samples were centrifuged (16,000g, at 4^{o}C for 20 minutes) and then put on ice until ready for loading into the gel. The running buffer used was 2-(N-morpholino) ethanesulfonic acid (MES) which was made fresh when needed and made by diluting a 20 times concentrated solution purchased from ThermoFisher Scientific (the buffer after

dilution contains, 50mM MES, 50 mM Tris base, 0.1% w/w sodium dodecyl (lauryl) sulfate (SDS) and 1 mM EDTA all pH balanced to 7.3).

The gel electrophoresis tank was set up, with a pre-cast 12 + 2 well Citrion, 12% tris agarose gel (both were purchased from Bio-Rad), and the tank filled with MES buffer. A aliquot of supernatant from the sample (40 µl) was pipetted into tubes and SDS running buffer (10 µl, the buffer was made from the following ingredients all purchased from Sigma-Aldrich: Tris/HCl, 240mM ~pH 6.8, PubChem substance ID 329749168; SDS, 8% w/w, ≥99% purity, PubChem substance ID 24896426; Glycerol, 40% w/w, ≥99% purity, PubChem substance ID 24895216; DTT, 100 mM; EDTA, 50mM; Bromophenol blue, 0.004%, PubChem substance ID 24891504) was mixed with each sample. The tank lid was connected to a Bio-Rad PowerPac and run for 30 minutes at 200V, stopping just before the running band came out of the bottom of the gel. Gels could then be stained with Coomassie Blue to visualise all protein bands present in the sample.

2.11 - Western Blot

Some gel electrophoresis samples were further analysed by western blot. Tris Glycine SDS (TGS) buffer was made by diluting 10 times concentrated stock solution purchased from Bio-Rad (final concentration of buffer contains; 25mM Tris, 192mM Glycine, 0.1% SDS and pH adjusted to 8.3). A precast gel was used with a 4-15% tris content 18 + 2 well and run using the setup describe previously and run for 20

minutes at 250V, the gel was then imaged as previously for reference but without staining.

Western blots are used to verify the presence of the purified protein in the fractions run on a gel using electrophoresis. This is done by soaking the run gel in an anti-body, for the His-tag that is part of the desired peptide, that has been bound to a dye molecule allowing for visualisation.

The gel was then placed between two transfer membranes (purchased from Bio-Rad) ensuring all bubbles are removed using a roller, then placed into a trans-blotter box and run using the trans-blot turbo ™ transfer system purchased from Bio-Rad for 5 minutes at 2.5V.

The gel was rinsed and placed in a tray on a rocker with enough Instant Blue™ stain (commercial Coomassie blue stain purchased from Sigma-Aldrich) to cover the gel and left to stain for at least 1 hour, after staining the gel is scanned. The transfer membrane was washed for a few seconds in methanol before being put in a tank to soak with PBS-T (PBS-T is Phosphate Buffered Saline solution with Tween 20 added for stability ~25 mL, made from a 20 times concentration stock to a final concentration containing; 10 mM sodium phosphate, 0.15M sodium chloride, and 0.05% Tween-20). A second PBS-T solution was made containing 5% reconstituted milk (25 g of milk powder in 50 mL of PBS-T), the membrane was transferred to the second solution after rinsing with PBS-T buffer and put on rocker for 1 hour. The membrane was then rinsed twice in PBS-T before soaking in the primary antibody (anti-His antibody harvested from mice and purchased from General Electric [GE healthcare] this was made up to the desired 1:3000 dilution with PBS-T) for 1 hour;

the antibody was then washed 3 x 5 minutes in PBS-T. The secondary antibody (diluted 1:5000 with PBS-T, also purchased from GE healthcare containing 0.4 g of milk powder) for 1 hour, and then rinsed in the same way.

The membrane was then coated in pre-mixed exposure elements (purchased from Bio-Rad) and then imaged using variety of exposure times.

2.12 - *Pisum Sativum* Growth and Chloroplast Extraction and Import

Pisum Sativum, Kelvedon Wonder peas (Purchased from Plantfrø by our collaborators from Copenhagen Plant and Environmental Science Department) were chosen as the chloroplast harvesting organism. Growth trays were prepared with a 50/50 mix of fine grain vermiculite and soil approximately 3-4 cm deep, on top of this a liberal covering of the peas were scattered creating a thick layer of seeds on the surface. Another thin layer of fine grain vermiculite was added and the peas were watered till the soil was wet to the touch. The peas were then incubated in a Percival growth chamber (light intensity 120-150 µmol/m^2sec, with a light cycle 16hour/8hour, light/dark, temperature between 22-23^{o}C and humidity 50-60%, purchased from Accela), the peas were watered every 2 days if the peas were dry and grown for at least 10 days and until small shoots with leaf buds had grown from as many seeds as possible. Once the peas had grown to the desired maturity they were moved to a dark room and left overnight before chloroplast extraction.

The following steps were done in the dark room apart from the centrifugation which was conducted in as low light as possible and the samples where covered with tin foil during transport. First HS buffer at 1x and 5x concentration was prepared (the normal concentration HS buffer contains; 250mM, HEPES (NaOH salt), PubChem substance ID 24895572; 1.65 M, sorbitol, PubChem substance ID 57653050, both were purchased from Sigma-Aldrich) and kept on ice. The leaves, buds and tops of all saplings were cut and put into a blender, then HS buffer was added ensuring that all the plant material was fully covered. The material was partially homogenised with 3-5 short pulses of the blender. The resultant material was then filtered through a double layer of nylon gauze into a container on ice and then carefully separated in to equal amounts in round bottomed centrifuge tubes (these tubes were pre-cooled on ice). The tubes were then centrifuged in a pre-cooled centrifuge with the following conditions; 4^{o}C, 3300 g with an acceleration of 9 (top-speed) and a deceleration of 4, the supernatant was carefully poured off to avoid disturbing the pellets and the pellets were resuspended carefully in HS buffer (1.5 mL) using a micro-pipette with a diagonally cut tip with an opening of approximately 0.5 cm; the liquid can be gently stirred with a Q-tip cotton bud if resuspending the mixture is difficult.

Fresh tubes were put on ice in pre-made holes in the ice so as not to cause kinetic stress to the chloroplasts at any stage. In these fresh tubes Percoll ® pads (containing, 4.5 mL of MQ water, 3.5 mL of Percoll ® purchased from Sigma-Aldrich, and 2 mL of the 5 times concentrated HS buffer made previously) were prepared and the resuspended chloroplasts where pipetted very carefully onto the pads, using the cut off tip pipettes and by letting the liquid run gently down the side of the tube at a shallow angle (no more than 5 mL of chloroplast resuspension was used per Percoll

® pad). The tubes were then centrifuged for 8 minutes at 4°C (pre-cooled), 1400 g, acceleration of 7, and a deceleration of 4. The sample separated into three layers, the broken and unsuitable material at the top, the Percoll ® pad in the middle and the suitable, unbroken chloroplasts at the bottom as a pellet. Using a glass Pasteur pipette, the first two layers were carefully removed and disposed of in biological waste, the pellets were resuspended in HS buffer to the maximum fill level of the tube and centrifuged again for 2 minutes at 3000g and 4°C (pre-cooled), with an acceleration of 7 and a deceleration of 4. The supernatant was then disposed of and the pellets collected and resuspended in 200-500 µl of HS buffer using cut off pipette tips. A sample (50-100 µl) of the chloroplasts was kept and flash frozen with liquid nitrogen for testing (if the sample appears to be anomalous in subsequent testing) and the rest was immediately used for the import study or direct fixation for TEM imaging. Chloroplasts are stable for 8 hours maximum once extracted without flash freezing.

For the import experiments all chemicals (from Sigma-Aldrich) were prepared fresh on the day and kept on ice. The HS buffer was the same as previously discussed; Magnesium Adenosine Triphosphate (MgATP) (100 mM in HS buffer, ≥95% purity, PubChem substance ID 24891422); calcium chloride (100mM in MQ water, ≥96% purity, PubChem substance ID 24892577); and the type X-protease thermolysin (57.8µM in HS buffer).

The chloroplast concentration was approximated by taking 5 µl of chloroplasts and making up to 1 mL with 80% acetone (and MQ water). This solution was then centrifuged at maximum rpm until the system had pelleted, the absorbance was then

measured at 652 nm (against a 80% acetone baseline) to then calculate the concentration.

All the samples were kept on ice until incubating in a light bath, and all mixing was gently done using pipette tips with the tips cut off to widen the opening. The samples were made by mixing in an Eppendorf (1 mL) containing: chloroplasts (50 µl at an approximate concentration of 1 µg Chloroplast/µl); MgATP (12 µl of 100mM stock solution); HS buffer (63 µl) and after the bath was set up and all the solutions were mixed, the sample was added (12.5 µl) and mixed. The samples were put into an Eppendorf float and immediately moved to a large tank of water (kept at 25^{o}C), with a large, high intensity white light source directly beneath the bath, and incubated for 30 minutes.

Afterwards 700 µl of HS buffer was added and the sample was centrifuged (6000 rpm for 1 min at 4°C). All resultant sample pellets were resuspended in HS buffer (120 µl each) and stored on ice, in the dark and fixed as soon as possible. The two particle samples were concentrated by the removal of at least 30 µl of water, then calcium chloride (2.5 µl of 100mM) and thermolysin (2.5 µl of 57.8µM) was added to each sample. The samples were mixed and then incubated on ice for 40 minutes. EDTA (2 µl of 0.5M) was then added to the mixtures to stop the reaction and then centrifuged (6000 rpm for 1 min at 4°C) before resuspending in HS buffer (30 µl), in preparation for fixing.

2.13 - Gold Slide Coating with Particles and Photosystem 1

The gold slides were purchased from Arrandee ™ metal GmbH and Co KG, and were 11x11 mm glass squares coated in a gold (111) terrace a few hundred nanometres thick. The slide was only ever handled with gloves and tweezers. The slide is initially cleaned and annealed by rinsing several times with ethanol and then heating until the corners glow red in a butane fuel burner set to a low flame, after which the slide was then placed into the first incubation solution.

First the slide was incubated for 7 days in 2mM hexane dithiol (purchased from Sigma-Aldrich, PubChem substance ID 24901736) dissolved in ethanol. The slide was rinsed multiple times by submerging in a sample vial filled with MQ water for 2 minutes and repeating the process with fresh water twice more. The next coating was dependent on the experiment, for the photosystem 1 coating, the rinsed slide was placed in a vial of photosystem 1 solution in a dark box and left for 48 hours before rinsing again with MQ water; the photosystem 1 solution was made up as described previously in this section. For the nanoparticle coating, a solution of citrate gold nanoparticles with sodium citrate added to a final concentration of 20mM was made and the slide incubated in this solution and left for 48 hours; after this the slide was rinsed once more in MQ water.

Chapter 3

As previously discussed, GNPs with surface functionality that are either charged or can become charged in biological conditions, can form an EDL. Once introduced to biological media, if the particles form an electrochemical double layer, this will change the surface chemistry and how the GNP interacts with the outside of the cell; such as its cellular uptake. Another problem caused by the formation of an EDL around GNPs is that it creates a localised high concentration of certain electrolytes, which can cause certain triggers in cells to occur and alter intracellular signalling which could be undesirable.

The EDL has been studied using a variety of techniques, as discussed previously, and experiments have shown that the EDL is predicted to be no more than a few nanometres in size[42,43]. With increasing electrolyte concentration around the GNP, the 'slipping layer' becomes more densely packed, as more ions of both charges become available and attract each other. Our previous work showed that with DCS it is possible to observe changes in nanoparticle diameters as small as 0.2 nm, we hypothesised that DCS could be a suitable technique to analyse the thickness of EDL surrounding GNPs in different solutions with varied electrolyte concentrations.

3 – Differential Centrifugal Analysis of Electrochemical Double Layer

For the initial experiments, we needed to consider the size of the nanoparticles, as the smaller the particle, the larger the percentage of change to the nanoparticle distribution with the EDL and therefore the easier to study. However, the smaller the particle the longer each sample will take to analyse and the CPS machine is not capable of analysing a GNP smaller than 3 nm, due to the larger contribution of Brownian motion. The initial particle size chosen was approximately 8-10 nm, as these GNPs have a relatively simple, rapid synthesis and are large enough for a relatively short and achievable sample analysis time. The possible relative change in size ranging from 0.1 (the smallest resolution previously achieved by the CPS machine) – 1 or 2nm (the largest theoretical size of the EDL) would give 1-20% of a diameter change in these samples which we hypothesised would be simple to analyse. We also considered which ligand would be used for the GNP stabilisation and the capping ligands ability to become charged in electrolyte solutions, i.e. its ability to form an EDL. The particles also needed to remain stable in the electrolyte concentration used during the experiments. Figure 24 is an image of the range of ligands that were used throughout these experiments. The initial two ligands chosen were PEG (11 carbon atoms and 6 ethylene repeats) ending in an alcohol group, as this ligand should remain un-charged at the pH of the experiments planned and the

short peptide CALNN, as this ligand has many side groups that should become readily charged at the pH planned for this experiment.

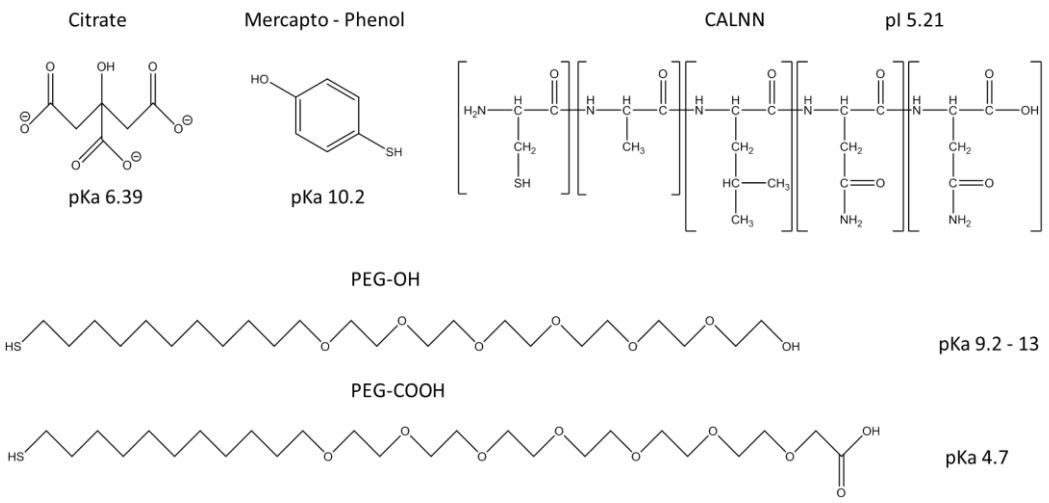

Figure 24: Ligands used in EDL experiments and the approximate pKa and pI[100]*.*

Finally, we needed to decide on the range of electrolyte concentrations and the types of electrolytes we were going to use for these experiments. The coating on the CPS disc, as the manufacturer states, is reasonably resistant to chemicals but a relatively inert electrolyte was still the best choice, to ensure these electrolytes would not damage the CPS and hence alter our results or shorten the life span of the machine. The electrolyte chosen also could not contain any active halogen species, as this could react with the gold nanoparticle surface and affect the experimental outcome. The initial electrolyte species chosen was sodium sulfate, as it met all of the above criteria and has a reasonably large anion.

As previously discussed in section 1.1.3 – Electrochemical Double Layer, the EDL consists of a slipping layer that does not travel at the same speed as the solid, much

denser nanoparticle core, as such this can lead to electrophoretic drag and or the loss of the slipping layer during centrifugation. To limit the loss of the slipping layer and the effect caused by the electrophoretic drag on the results, the sucrose gradient contained the same concentration of electrolyte as the sample measured, this aimed to maintain the double layer's equilibrium throughout the measurement. This meant that every measurement was performed in a freshly made gradient, which makes the process more time consuming, and required the disc to be thoroughly cleaned in between each new gradient, to ensure no contamination. The measurements were also done in ascending order of electrolyte concentration, to ensure that any contamination between runs would be negligible. Any changes to the gradient density or viscosity due to the electrolyte are accounted for by the machines software during analysis, by initially running a control sample of a PVC with a known size.

For the primary experiments, initial stability tests were performed by taking a sample of nanoparticles (at approximate absorbance of 1 and to a total volume of 2 mL) and adding electrolyte at a known range of concentrations (0, 0.001, 0.005, 0.01, 0.05, 0.1, 0.5 and 1M). The samples tested were citrate and the afore mentioned PEG OH and CALNN; the citrate was found to aggregate at 50mM, and CALNN was found to aggregate at 0.5M. Given the stability tests, the initial experiments were completed with just the PEG OH and CALNN stabilised particles, over concentrations of 0 – 0.1M. The samples were incubated with electrolyte overnight to ensure equilibrium was reached, before measurements were taken. The expected result was that as the electrolyte concentration increased, the EDL would contract and form a thinner more compact layer, as previously discussed in section 1.1.3 – Electrochemical Double

Layer; so, the reported size should get larger due the CPS density discrepancy decreasing (also discussed in section 1.2.3 - Differential Centrifugal Sedimentation).

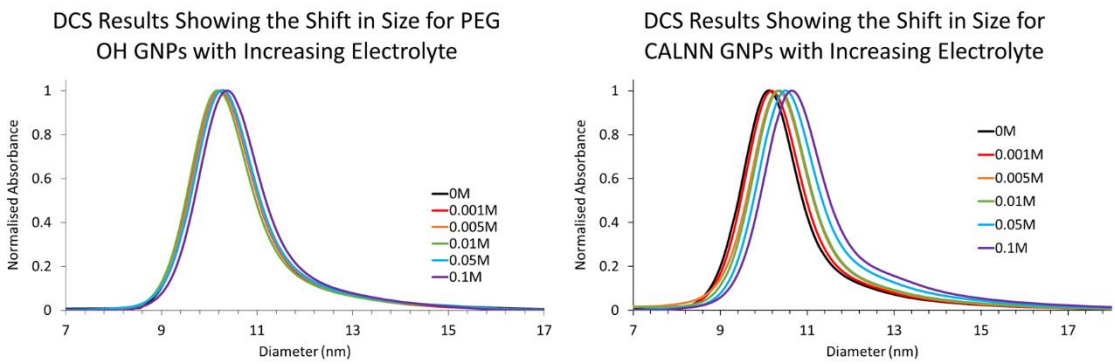

Figure 25: Raw DCS results showing the shift of the initial particle tests when introduced into solutions with increasing concentration of electrolytes.

As can be seen from the initial results in Figure 25 the expected trend was observed for CALNN with the reported size rapidly increasing in size, indicating a thinner EDL was formed. Whereas the PEG OH stabilised particles show little to no change in size when electrolyte concentrations were increased, which was expected as these GNPs should be uncharged at the experimental conditions and hence minimally affected by the addition of electrolytes. Only at the highest electrolyte concentration did the PEG OH GNPs show any visible change in size.

DLS and Zeta potential measurements were taken of all of these initial samples, but the data for both were inconsistent and this made it difficult to draw any conclusions from this data, so it is not shown in this thesis. Due to the high concentrations of electrolyte in the samples, the zeta potential measurements were never consistent and at the highest concentrations all measurements were reported as error values.

The DLS measurements are also known to be poor and easily distorted by contaminants (in this case the increasing concentration of electrolytes) with particles of this size range[31,55].

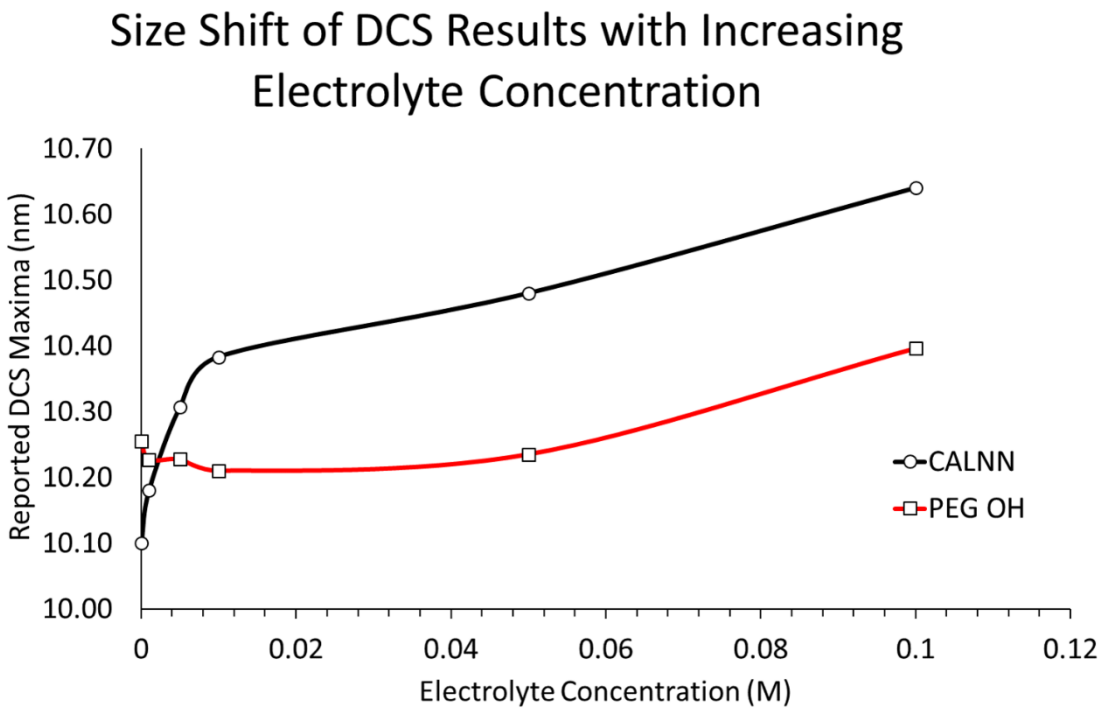

Figure 26: Graph showing the shift in size seen by the DCS measurements with increasing electrolyte concentration for both CALNN and PEG OH coated GNPs. All points are the average of at least three runs of the same experiment.

The raw DCS maximum values of the GNPs without added electrolyte were deconvoluted, using the method described in section 1.2.3 - Differential Centrifugal Sedimentation, to give a core size value for this batch of nanoparticles and the thickness of the ligand shells. The deconvolution formula can then be geometrically modified to account for a second layer (the electrolytes) on top of the ligand shell, that simulates the effect on the reported size by the EDL and therefore providing an

approximate thickness for the EDL itself (This is the same splitting of the ρ_{eff} as published in our recent paper[101] and discussed later in this thesis, Equation 14. Figure 27 shows the deconvoluted data which demonstrates the change in size due to the EDL plotted against the electrolyte concentration used.

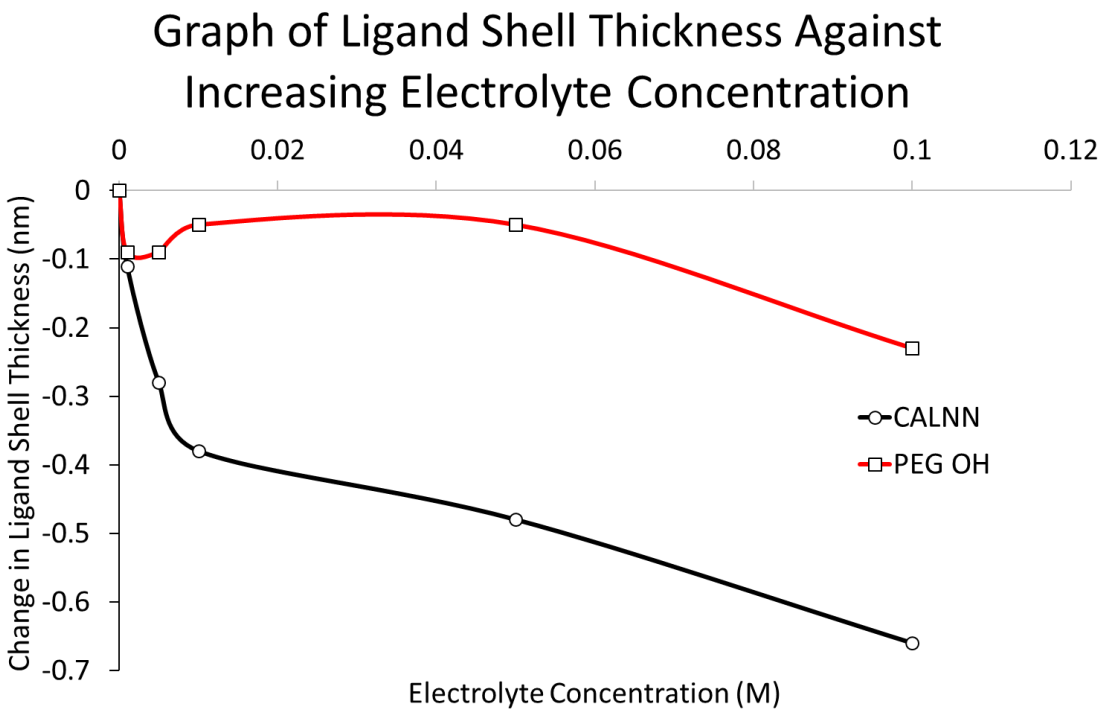

Figure 27: Graph showing the shift in ligand shell thickness with increasing electrolyte concentration. All points are the average of at least three runs of the same experiment.

As can be seen in the graph above (Figure 27), the PEG OH as previously stated shows little to no change in size as it should not be charged and therefore no EDL should be formed. However, at the last concentration (0.1M) there is a shift of 0.2 nm, but this is close to the error of the measurement, so is not thought to be significant on its own. The CALNN particles however, do have a significant shift in ligand shell size with increasing electrolyte, shrinking with increasing electrolyte layer by 0.66 nm. This is

the expected trend to see for the double layer with increasing electrolyte concentration, as the charges increase and the electrolytes concentrate into a thinner layer.

The density of the EDL layer was expected to change as the electrolyte concentration is increased, as this will reduce the solvent present as it is replaced by a more compact layer of ions. This makes obtaining exact numerical values for the EDL more difficult than previous deconvolutions as this compacting process needs to be accounted for. Also, as previously mentioned, electrophoretic drag will still play a part in slowing the particle during centrifugation, thus changing the reported size. During the deconvolution, the assumed solvent density of 1.064 g/L for the hydrated solvent shell was adjusted to the fraction of the electrolyte density added. At the concentrations we measured this change in density assumption had little effect on the final values (the effect of density on the measurements when the shell is small compared to the nanoparticle has been shown in our published work Z.Krpetić Et. al.[31] and later in A.Davidson Et. al[101]. The adjustment of the density also assumed the density of the bulk solution, which is not strictly true for our experiments but as it made little difference to the value, it provided a good approximate.

As for the electrophoretic drag, we added electrolyte to the gradient, in an attempt to minimise this issue, but the parallel trend of the data seen after a certain concentration, could be the effect of the electrophoretic drag becoming the dominant force, after the EDL has shrunk as much as possible.

Although there have been many models to determine electrophoretic drag produced previously for applications such as gel electrophoresis, a case like this has not been

modelled previously. Also, most models that do exist, are only applicable for a limited range of Debye lengths and electrolyte concentrations[102]. This is not a simple process, as most previous models calculate drag based on the force applied from an external electric field; which in our experiments is a pseudo electric field induced when the particles beginning to move under the influence of the centrifugal force applied. The force experienced by an individual particle is difficult to accurately measure, as is the exact nature of the field and the drag experienced by the particle this adds complexity to the overall process making it more difficult to model. After undergoing an extensive literature review[41,42,102–109] a simplified expression of the Herny's function[103] was discovered that we found to be a good approximate of the situation.

$$U = \mu E$$

Equation 11: Formula relating momentum of particle to electric field/force applied[103].

Equation 11 is a formula using the momentum of the particle (U) (which is also linearly proportional to the particles mass), which can be determined from the time the particle takes to be detected in the CPS measurement. This equation relates this momentum to the electrophoretic mobility (μ) and applied electric field (E), which in our experiment, is the overall force experienced by the particle. This equation shows that the momentum is linearly proportional to the electrophoretic mobility of the particle, which can be calculated using Equation 12; where ε_r, ε_0 are as described in the introduction (1.1.3 – Electrochemical Double Layer), η is the viscosity of the fluid

(Pa.s), ζ is the zeta potential (V) and f(κa) is the Henry's function which depends on the debye length κa.

$$\mu = \frac{2\varepsilon_r \varepsilon_0 \zeta}{3\eta} f(\kappa a)$$

Equation 12: Formula for calculating the electrophoretic mobility of a particle[103].

A simplified version of Henry's function was used, which accounts for a wide range of Debye lengths and electrolyte concentrations, to within 2% variation from the more accurately modelled shorter ranges (Equation 12); where κa is the calculated Debye length which was calculated originally using Equation 2.

$$f(\kappa a) = \frac{16 + 18\kappa a + 3\kappa a^2}{16 + 18\kappa a + 2\kappa a^2}$$

Equation 13:A simple approximation of Henry's function[103].

The relationship was then modelled by plotting the observed change in ligand shell thickness in nm against Henry's function for the electrolyte concentrations used (Figure 28). This should be a linear relationship if the electrophoretic drag is involved within the process and the trend line seen in our data agrees with this hypothesis.

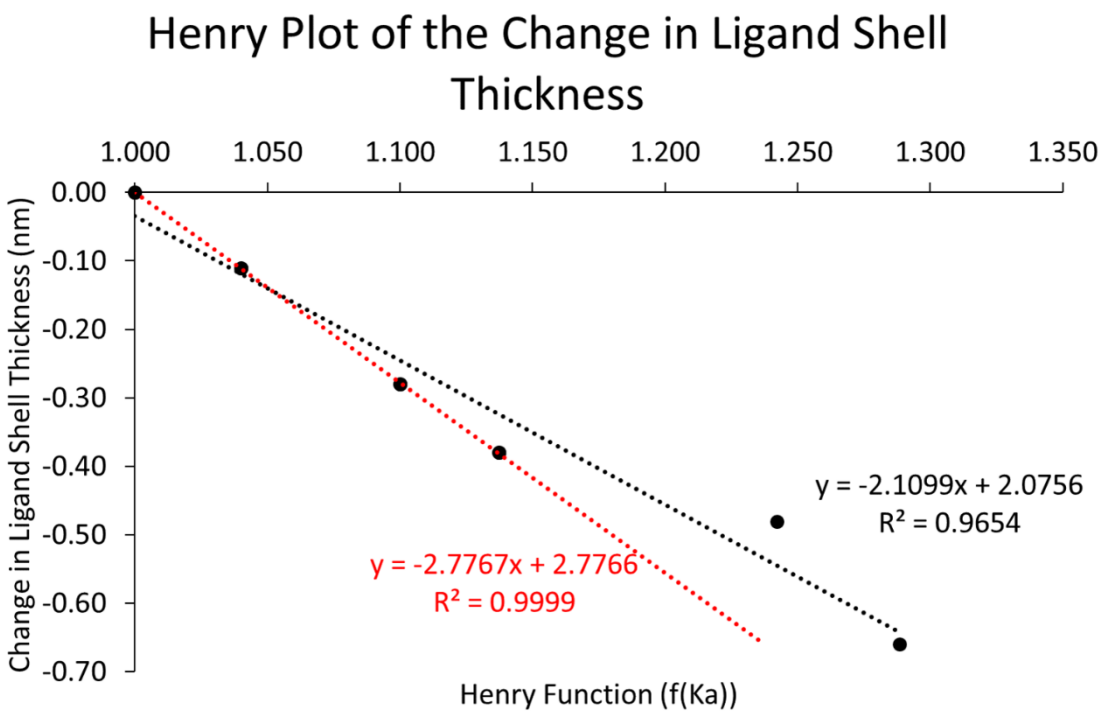

Figure 28: Henry plot of the change in ligand shell thickness. The black trend line aligns with all data points and the red trend line aligns with for the first 4 data points and excludes the two outlying data points at higher electrolyte concentrations.

When the trendline is aligned to all the data points (black trendline), our data is reasonably close to this trend, but with a larger margin for error; whereas when the trendline is fitted through the first 4 data points, omitting the last two as outliers (red trendline) the R^2 value improves dramatically. The quantitative analysis of the data as a whole, proved to be a lot more difficult to achieve than predicted, given the high number of variables in this system, so a larger number of data points and information was required in a hope to improve the accuracy of this data.

It is also important to note that using the above equation, the Debye length (or Henry's function in this case) would also show a linear relationship with respect to the zeta potential (ς) and the inverse of the viscosity (η) which can be seen in Equation 12. The zeta potential and viscosity will change drastically over the range of electrolyte

concentrations used in this experiment. While the viscosity should be adjusted for by the standards run before every measurement in the technique, this could still play a role. The zeta potential could be measured for the samples in question thus helping to remove or account for the variable in the analysis; however, the equipment and expertise required for this were not readily accessible within the time frame of this project but should be considered for future work.

Several things were considered for these follow up experiments in an attempt to improve the data gathered including; the concentration range, the capping ligand and the electrolyte. The concentration range cannot be altered much due to its role in the stability of the particles but additional concentrations within the range could easily be included in future experiments. The ligands chosen needed to be reconsidered, CALNN has many charge centres which added complexity to the analysis as a high number of charge centres might affect the structure of the EDL. PEG OH did not need repeating, as it had shown no EDL formation which was expected due to its lack of charge. The electrolytes previously used were divalent, which would also affect the structure of the EDL and make analysis even more complex, so monovalent electrolytes were chosen instead.

After these considerations, further experiments used citrate, mercapto-phenol and PEG COOH capped particles, and used sodium perchlorate as the electrolyte solution (the range was 1mM-30mM (20mM limit for the citrate GNPs)). The new particles were all analysed in a pH 11 buffer to ensure the mercapto-phenol and PEG COOH particles were fully de-protonated and therefore charged. The deconvoluted changes in shell thickness are given below in Figure 29, where they are plotted against the electrolyte concentration.

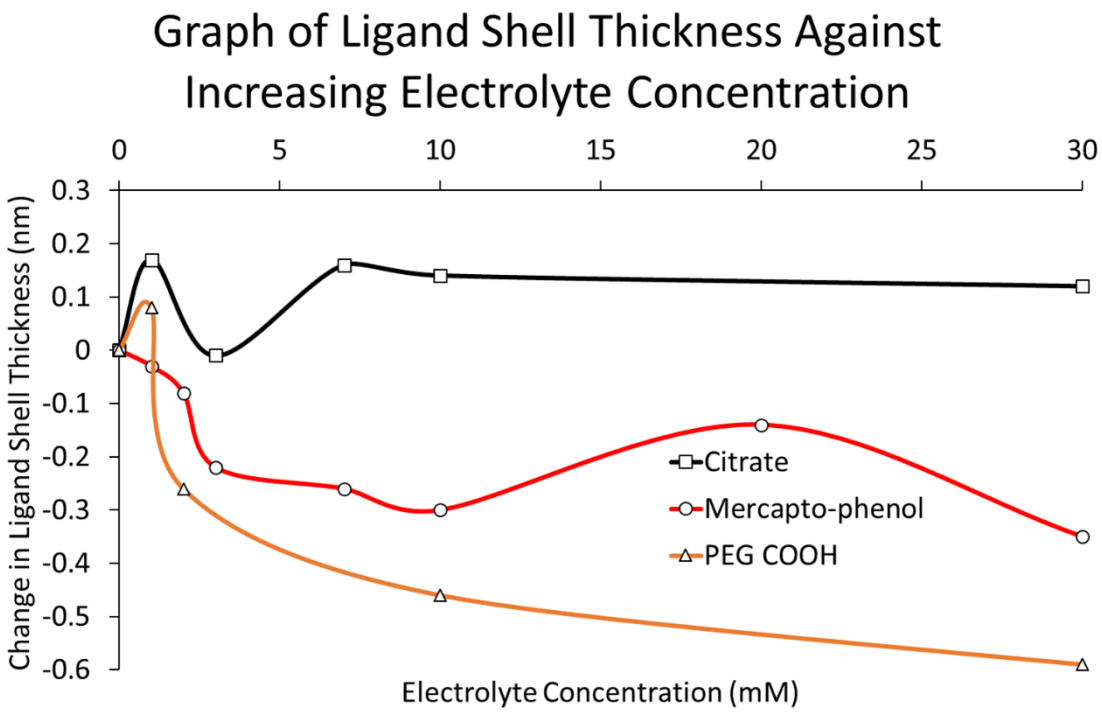

Figure 29: Graph showing the shift in ligand shell thickness with increasing electrolyte concentration. All points are the average of at least three runs of the same experiment.

Figure 29 shows the citrate GNPs experienced no appreciable change in ligand shell thickness until they rapidly aggregated at higher electrolyte concentrations. The mercapto-phenol particles appear to follow the expected trend however, there was some variation in the measurements and the synthesis of these GNPs was much more difficult to handle and produced a more heterogeneous sample that would affect our measurements and possibly hinder the reproducibility and hence accuracy of these data points. Given these results, only the PEG COOH particles were continued over the larger concentration range, as they were found to be much more stable at higher concentrations. Below (Figure 30) are the deconvoluted changes of the shell

thickness of these PEG COOH GNPs, plotted against the increasing electrolyte concentration.

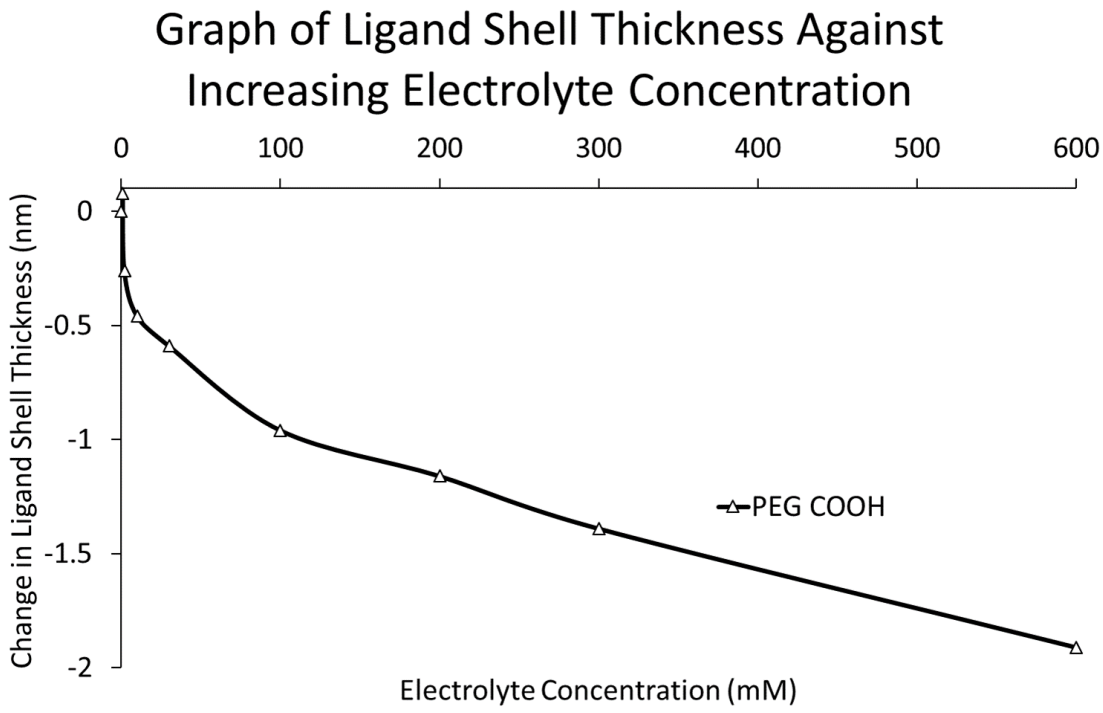

Figure 30: Graph showing the shift of the ligand shell thickness of PEG COOH GNPs with increasing electrolyte concentration. All points are the average of at least three runs of the same experiment.

Figure 30 shows that the PEG COOH GNPs are stable, even at concentrations of 0.6M of sodium perchlorate. The ligand shell thickness follows the expected trend of the double layer shrinking with increasing electrolyte. Next, we wanted to see if there could be any difference distinguished between changes in the ions used in the EDL. The PEG COOH GNPs were incubated in lithium perchlorate, potassium and cesium chloride (up to a concentration of 200mM, as the PEG COOH particle batch was running low and we wanted to complete all the comparisons with the same batch of particles for consistency). Potassium and cesium chloride were chosen as their

perchlorate counterparts have very low saturation points (at room temperature) however, this made the two sets difficult to compare. Figure 31 demonstrates the changes in shell thickness for the PEG COOH particles when exposed to the different electrolyte solutions.

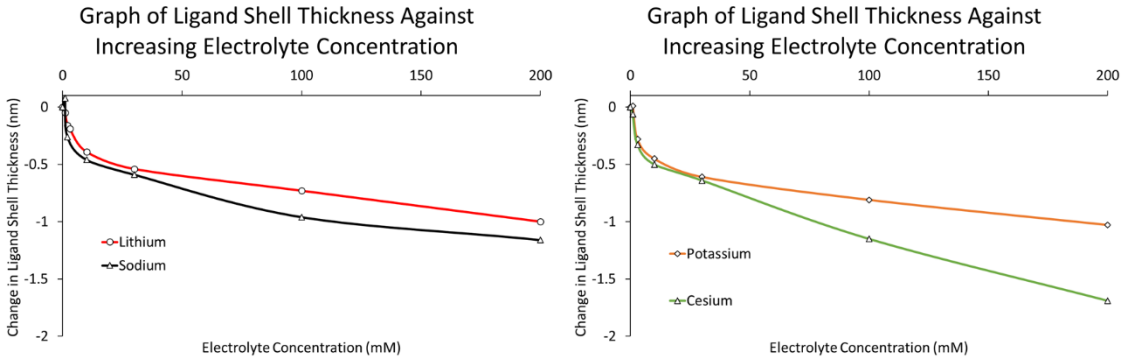

Figure 31: Graphs showing the change in thickness for the PEG COOH particles when exposed to the different electrolyte solutions. Left, the change with lithium (red) and sodium perchlorate (black)with and right, the change with potassium (orange) and cesium chloride (green). All points are the average of at least three runs of the same experiment.

As can be seen in Figure 31 the data showed very minor changes between the different electrolytes until a concentration of higher than 30mM and then the variation between the electrolytes became much larger. This deviation was also in a similar position to the parallel affect seen in the initial data; however, in both sets the shifts (in the minor ones) occurred in the expected order, due to the mass of the ions, with the larger and heavier ions giving greater changes in size. Figure 32 compares all of these samples on the same graph, but as previous mentioned, it is difficult to directly compare these samples.

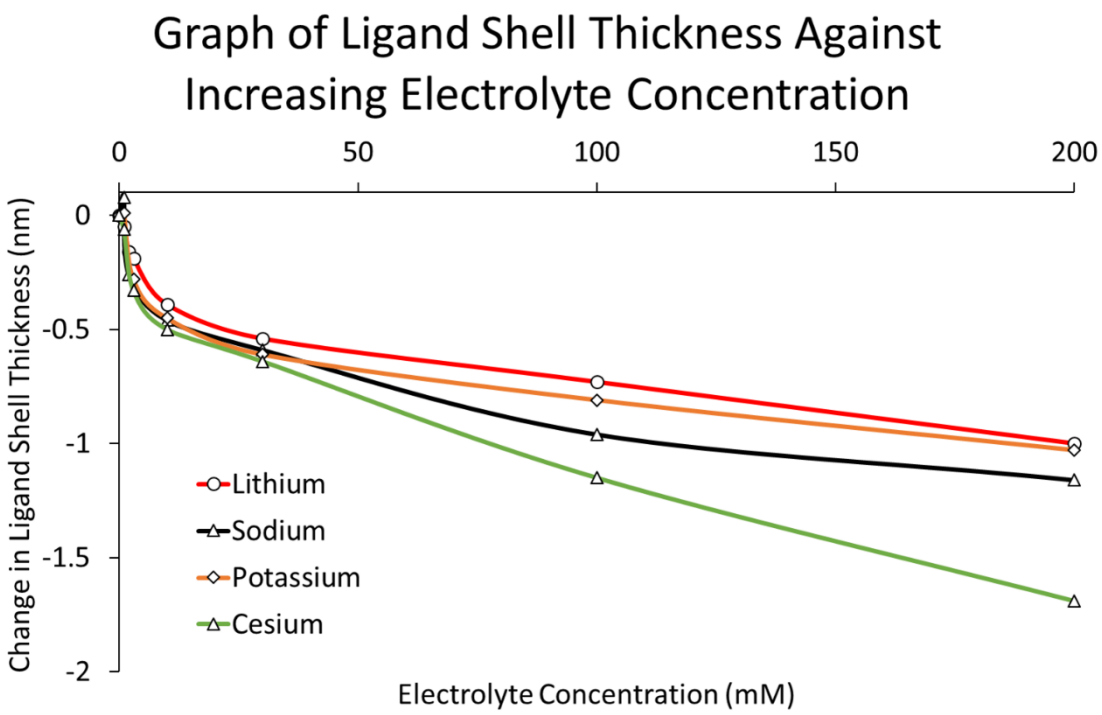

Figure 32: Graph showing the changes in thickness for the PEG COOH particles when exposed to different electrolyte solutions. All points are the average of at least three runs of the same experiment.

Finally, we completed further preliminary tests in which we changed the anion by incubating the particles in sodium chloride and iodide. Sodium iodide was expected to produce a subtler change in size when compared to the chloride sample, as the surface charge of the GNPs is negative. A large proportion of the double layer is likely to consist of the cation; especially if the slipping layer is changed or lost in any way during the centrifugation. Below is a graph of the results (Figure 33). This preliminary data had very large margins of error and no real conclusions could be drawn from this data.

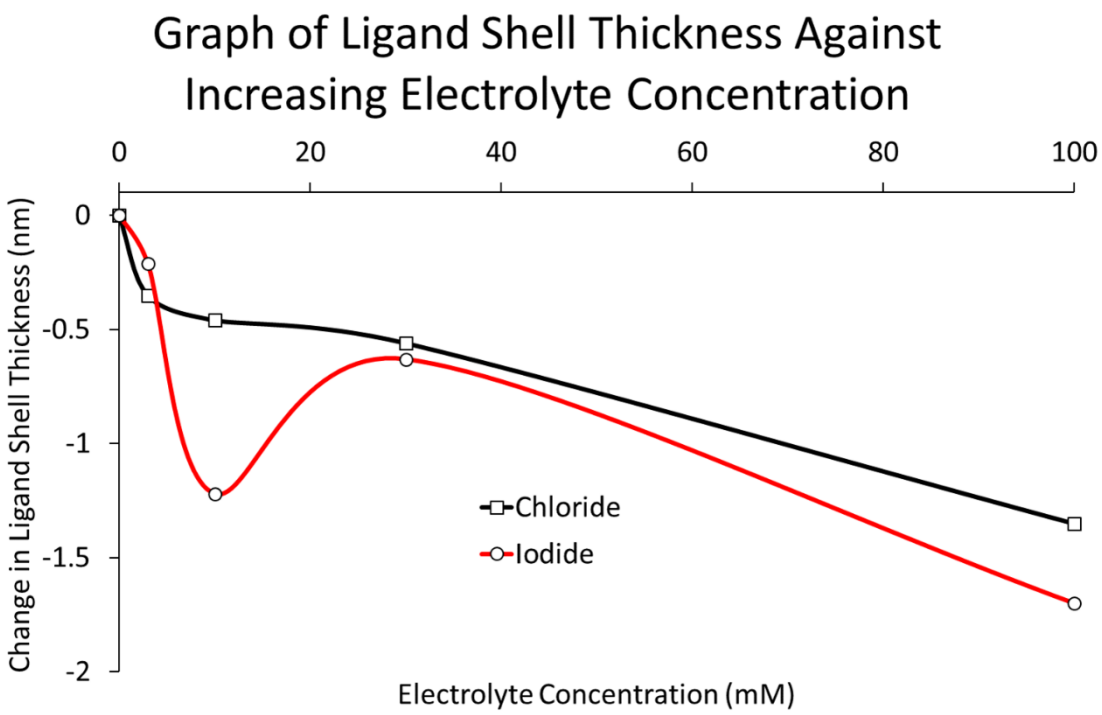

Figure 33: Graph showing the changes in thickness for the PEG COOH particles when exposed to the different electrolyte solutions. All points are the average of at least three runs of the same experiment.

To conclude, the DCS method appears to observe a regular and repeatable shrinking in ligand shell size when exposed to increasing concentrations of electrolyte. However, while qualitatively this can be assigned to the EDL and our data followed the expected trend giving size changes in the double layer that seem reasonable, quantitatively, this effect proved difficult to analyse with a multitude of variables.

Chapter 4

4 – Differential Centrifugal Analysis of Protein "Corona"

In this chapter we expand on the work our group and I did previously using the CPS and FTIR methods. From this work the below two papers were published: 1. Computational and Experimental Investigation of the Structure of Peptide Monolayers on Gold Nanoparticles; Colangelo E, Chen Q, Davidson AM, Paramelle D, Sullivan MB, Volk M, Levy R; LANGMUIR; 33(1):438-449 20 Jan 2017[77] ; 2. Sensitive Analysis of Protein Adsorption to Colloidal Gold by Differential Centrifugal Sedimentation; Davidson AM, Brust M, Cooper David L, Volk M; Analytical Chemistry; 89(12):6807-6814; 17 May 2017[101].

This work focused on evaluating whether the CPS could be used to measure protein interactions with GNPs, initially we investigated the packing density of peptide coatings, and then we looked into the formation of a protein corona.

4.1 – DCS Measurement of the Packing Density of a Short Chain Peptide Bound to a GNPs Surface

As discussed in the introduction, work done previously demonstrated[31] that the CPS can be used to analyse even small changes in the size of the ligand shell. Additional work done by Duchesne[110] on different CALNN capping layers and others[31,74] who have shown that FTIR can also be used to determine differences in packing density of short chain peptides attached to nanoparticle surfaces. Following the method set out by Duchesne et al[110], gold nanoparticle surfaces were functionalised with two different peptide densities. In brief, we incubated citrate stabilised GNPs with a high (~2mM) and low (~0.1mM) concentration of CALNN peptide to give different packing densities on the GNP surface. The difference in packing density was then verified by FTIR, using the methodology set out by previously by Martin Volk[31], the results are shown below.

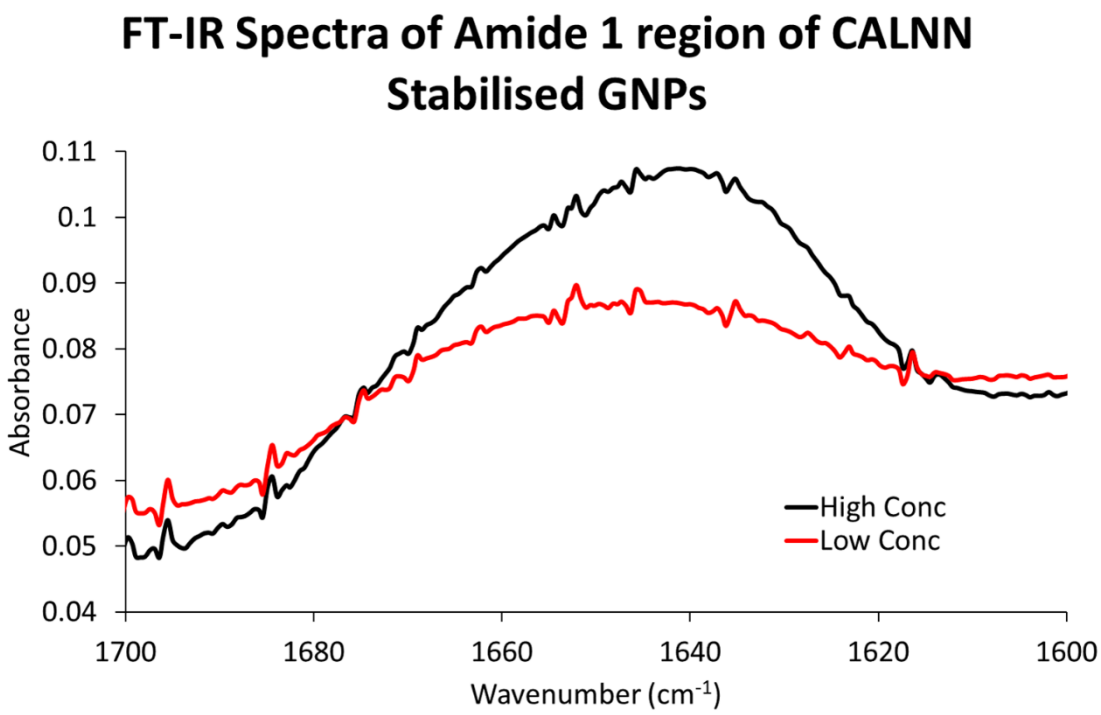

Figure 34: FT-IR spectra of the amide 1 region of the CALNN peptide incubated with GNPs at high and low concentrations. The spectra were run with a D_2O background which had the background water vapour removed.

The spectra shown above were run with a D_2O background and had also had any water vapour removed from the spectra mathematically. However, due to the relatively low concentration and hence low signal of peptides on particle surfaces, the spectra still had some noise associated with water vapour. The area shown in the spectra represents the amide 1 band, as this can be used to determine approximate concentration and secondary structure.

The spectra were analysed quantitatively by Martin Volk using Origin Pro, the method is outlined here and for more details and examples of its usage previously see the SI of the Željka Kreptić et al[31] paper. The packing density was estimated using the concentration of the GNPs as determined using UV/Vis; the size of the core as measured using the DCS method and the integrated absorbance of the amide 1 band

from the spectra. The integration used a linear background and a sum of pseudo-Voigt functions and it was noted and accounted for in the final values that, the asparagine side chains at the end of the peptide are close enough to the GNPs surface to contribute to the amide 1 band, approximately 40%. The pseudo-Voigt functions consisted of the sum of a Gaussian and Lorentzian curve with identical full width half maximums (fwhm) fitted to closely resemble the shape of the true Voigt bands (this was used as it provides values similar to the Voigt functions within the error of the method whilst being computationally less demanding). The bands were allowed to vary with respect to the peak position, fwhm, band area and the contribution of the two, during the fitting process till the best fit was achieved.

External electric fields suffer significant distortion close to the surface of a metal particle (the exact effect can be quantified using Mie's solutions to the Maxwell equations[76]) this leads to the following surface selection rules; vibrations with transition dipoles parallel to the GNPs surface have their absorbance strongly suppressed; those with transition dipoles perpendicular/ radially to the GNPs surface are enhanced (this phenomenon is used to an advantage in techniques like Surface Enhanced Raman Spectroscopy). This effect decays rapidly further from the GNPs surface but is considered significant at distances equal to the GNPs radius; so, for the relatively short CALNN peptide the entire peptide can be considered subject to these selection rules.

As we reported previously[31] the CALNN peptide is considered to be in its fully extended conformation when bound to the GNP therefore a straight backbone perpendicular to the surface of the GNP. The amide 1 vibration, which is mostly

dominated by the carbonyl stretch (see Figure 19), is at an approximately 20° angle with respect to the bond and therefore approximately 70° from the backbone and the surface normal. These assumptions would mean a slight suppression of the amide 1 absorbance for every amide bond in the peptide, giving an approximate suppression factor of 0.7. This was then calculated more quantitatively using a method similar to Donaldson et al[111] and this was shown to be closer to 0.78, assuming a GNP of approximately 11nm in diameter, dipole moments at 70° angles to the surface normal, averaged over all surface positions and orientations up to 1.6nm (the length of the fully extended CALNN peptide) from the surface.

The limiting factor of this method is how well the surface selection rules are accounted for, the above assumption for CALNN was shown to be a fairly good approximation in our previous paper, as the value we obtained was found to differ from a similar case where surface selection isn't an issue (amino acid analysis[110]) by only this calculated suppression factor. So, we can have some degree of confidence in our values; also using this method the relative packing densities of the high and low concentration CALNN incubations were determined to be 2.1 and 1.4 peptides/nm^2, respectively. These numbers are in agreement with the values measured previously[110].

The FT-IR data was then used in conjunction with a collaborator[77] to help verify and improve simulation work of peptide functionalisation of nanoparticles, this work was subsequently published[77].

The CALNN particles were then analysed using the DCS, using a standard sucrose gradient, to determine if this method could measure the difference in peptide packing density.

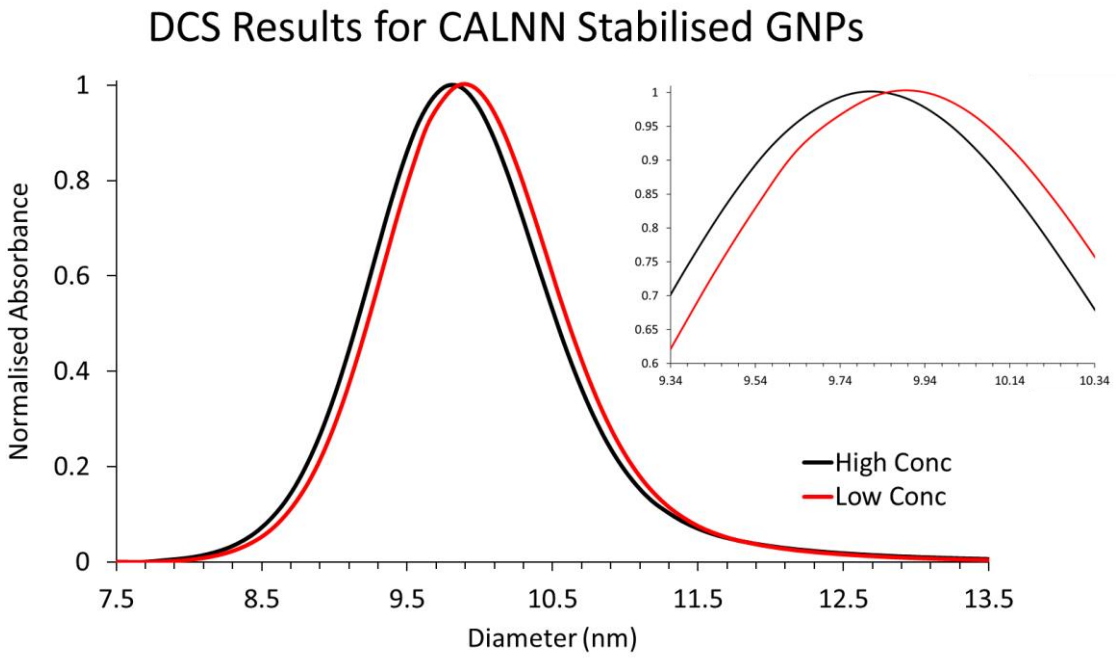

Figure 35: DCS results of GNPs incubated with high and low concentrations of CALNN peptide. Inset is an enlarged cross section of the graph, to highlight the shift in size.

As can be seen from the DCS data (Figure 35) there is a clear shift in size between the two particle populations of approximately 0.07 nm. This small value is normally within the stated noise of the measurement; however, the experiment was repeated multiple times, with the same core batch of citrate, and all repeats showed very little deviation from the above spectra; with the average of all runs giving a difference of 0.068 nm. As previously discussed (section 1.2.3 - Differential Centrifugal Sedimentation), a less densely packed ligand shell will allow the ligands to lie flatter

and be more solvated, thus lowering the overall density of the ligand shell of the particles and giving an expected increase in 'reported' size. In Figure 35 the shift in size was in the expected direction and after deconvolution, using our previously described method (discussed in more detail in section 1.2.3 - Differential Centrifugal Sedimentation) the higher CALNN concentration was found to have a capping layer approximately 0.12 nm larger than that of the lower CALNN concentration. This finding supports our FT-IR data in the hypothesis that, the lower concentration of capping ligand is less densely packed and therefore more able to move around in its random coil formation. This freedom of movement allows for a conformation more parallel to the particle surface and thus the particle appears larger in diameter.

Although close to the noise level of the machines measurement, it can be stated with reasonable confidence that a change in size was observed with different packing densities of proteins bound to nanoparticle surfaces. This was also in agreement with our FT-IR spectra of the particles and packing densities seen in previous work. Given the relative success of measuring such a subtle effect in size, the next part of this project focused on measuring adsorption of protein to a GNPs capping layer, rather than directly to the nanoparticle.

4.2 – DCS Measurement of Protein Corona Formation of the Capping Layer of GNPs

In this section the aim was to extend the use of the DCS method to analyse the formation of protein 'corona' around GNPs. The process of proteins adsorbing to gold surfaces and GNPs has been previously studied in a variety of ways [13,50–59], and the original analytical ultracentrifugation technique was pioneered to study a similar phenomenon (this is discussed in greater detail in section 1.2.3 - Differential Centrifugal Sedimentation)[68]. However, the more recent increase in GNPs being used in medical applications has seen an increase in the interest in understanding the formation of the protein 'corona'; this is because the protein 'corona' can greatly change or effect the activity of the GNPs. Several analytical methods that can yield information on the structure, size, orientation and stability of the protein 'corona' have been used. Some examples are: DLS and the work done by Walczyk et.al[112] and others[55–59,113]; Fluorescence Correlation Spectroscopy (FCS)[51–53] and Plasmon Scattering Correlation Spectroscopy (PSCS)[54] to study the hydrodynamic radii and diffusion coefficients; and TEM[114]. Each method has their own drawbacks and limitations.

We aimed to use DCS to measure the effect that protein corona formation has on GNPs. The majority of this work has previously been done using Human Serum Albumin (HSA) as this is the most abundant peptide present in human cells. However, due to its relative lower cost and availability, we used the Bovine analogue, BSA, for our experiments. The particle capping layers chosen for the initial test were: citrate, as it was known to be substituted by BSA[114]; a short chain PEG ending in OH, which was known to have limited-to-no interactions with biological molecules, such as proteins (and is often used as an unreactive coating in biological containers)[115]; and finally, a short chain PEG ending in COOH, as the carboxylic group was known to

interact with proteins and will also be charged[116]. A range of protein concentrations from 0.0017-15µM were investigated giving coverage over several orders of magnitude, to observe 'corona' formation. pH has also been known to effect particle growth and GNP stability depending on the capping layer. The charges of the end group of the PEG ligands can affect their interaction with proteins (PEG COOH carboxyl group ~pKa 4.7, PEG OH alcohol group ~ 9.2-13). The pH of the GNPs particles was measured after incubation in a range of BSA (has a pI of ~4.7[117] and is stable within the pH range of the experiments[118,119]) gradients and gave pH values from 6.1 (the citrate GNPs) up to 7.1 (the highest BSA concentration (500µM)). Below is an example of the initial results (Figure 36).

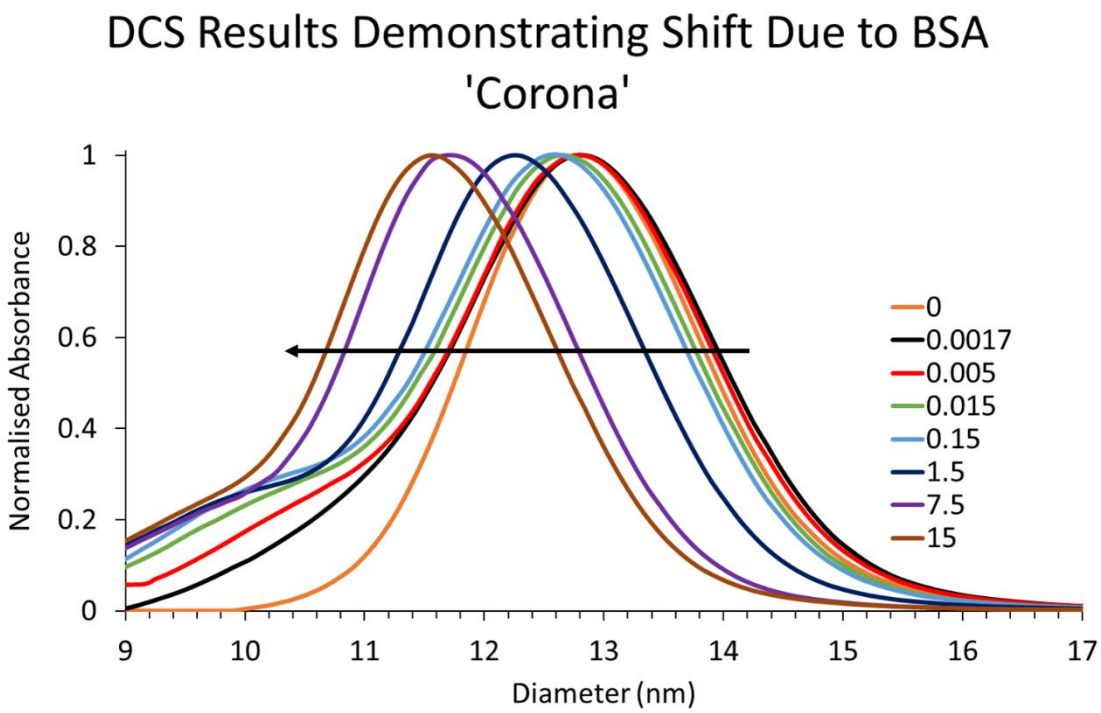

Figure 36: DCS results for Citrate GNPs incubated in various BSA concentrations. The arrow indicates the increasing BSA incubation concentration; the legend is the concentration of the incubating BSA solution in µM.

Figure 36 demonstrates that by increasing the BSA concentration, the apparent size of the particles decreased. As previously mentioned, the larger the capping layer (ligand and corona), the higher the error caused by the assumption of gold density and thus, the particle size is reported as smaller than actual, so the observed shift in size was as expected. The shoulder forming on the right-hand side of the peak is likely due to the non-uniform replacement of citrate by BSA in systems where a complete monolayer was not formed as polydispersity was introduced to the sample. The PEG COOH and OH also showed shifts of different magnitudes, the PEG COOH being comparable to the citrate and the shifts caused by the PEG OH being significantly less. The data was deconvoluted using a modification of the method previously published[31] and discussed in section 1.2.3 - Differential Centrifugal Sedimentation. The geometric splitting of the density component (ρ_{eff}) was split further, to include a second outer layer (where $s_{Protein}$ is the protein 'corona' thickness and $\rho_{Protein}$ is the density of the protein 'corona' layer) with a density of approximately 1.15 g/mL.

$$\rho_{eff} = \frac{\begin{bmatrix} d_{Au}^3 \rho_{Au} + \left(d_{Au-Shell}^3 - d_{Au}^3\right)\rho_{Ligand} \\ +\left(\left(d_{Au-Shell} + 2s_{Protein}\right)^3 - d_{Au-Shell}^3\right)\rho_{Protein} \end{bmatrix}}{\left(d_{Au-Shell} + 2s_{Protein}\right)^3}$$

Equation 14: Effective density component modified to include protein corona.

Previously, we used a value of 1.4 g/mL for a densely packed layer of peptides (CALNN[31]) which agrees with the literature for proteins, however, due to the irregular

shape of the peptide, the 'corona' is likely to be loosely packed making the smaller assumed density more reasonable. As demonstrated in our previous publication[31] the effect of the assumed density on the deconvoluted size is negligible even when changed by as much as ±0.2 g/ml. This statement becomes less true the further from the core of the GNP the shell extends, which is particularly important for the PEG COOH GNPs as the ligand shell already extends around 3.5 nm. Figure 37 includes graphs showing the effect of the change in density on the deconvoluted ligand shell thickness plotted against the reported size.

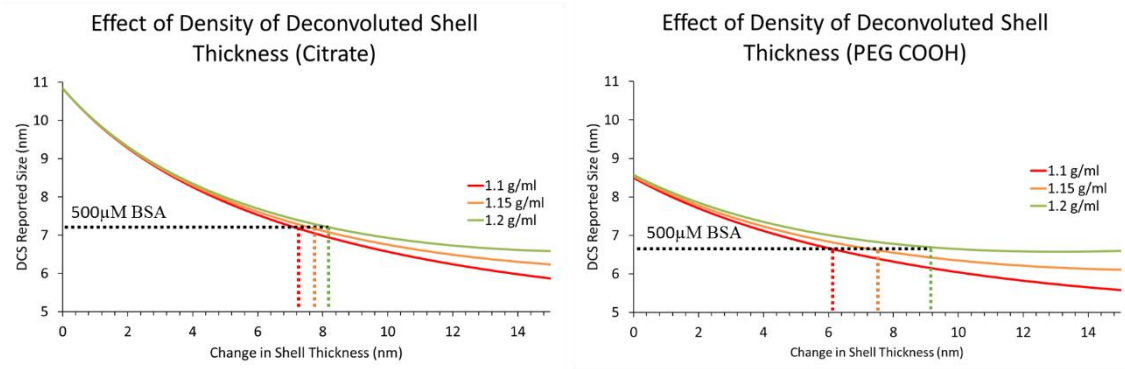

Figure 37: Graphs showing the effect of a change in density on the deconvoluted ligand shell thickness plotted against the reported size. Left Citrate, Right PEG COOH, Black line shows the final measurement at 500µM BSA, 1.1 g/ml(red), 1.15 g/ml (orange) and 1.2 g/ml (green).

Figure 38 demonstrates this effect in citrate GNPs, where the citrate is replaced by the BSA, the change in density measured at corona thicknesses lower than 6 nm are very minimal. Even at the largest concentration of BSA (500µM), the measurement shows a deviation of ±0.2 nm. In the case of the PEG COOH, the change in density before 5 nm thickness is minimal. However, at the largest concentration of BSA (500µM), the measurement shows a deviation of ±1.5 nm. So, the assumed density

appears to have a greater effect on thicker peptide layers skewing the sizing accuracy, again, this is because the density of these particles is more dominated by the protein. These results can be taken as a good gauge of the margin of error in the analysis of the data and for most of the measurements this error is very small (close to or less than the quoted resolution of the machine).

After the deconvolution, the change in capping layer in nm was plotted against the concentration of the BSA available in solution (Figure 38).

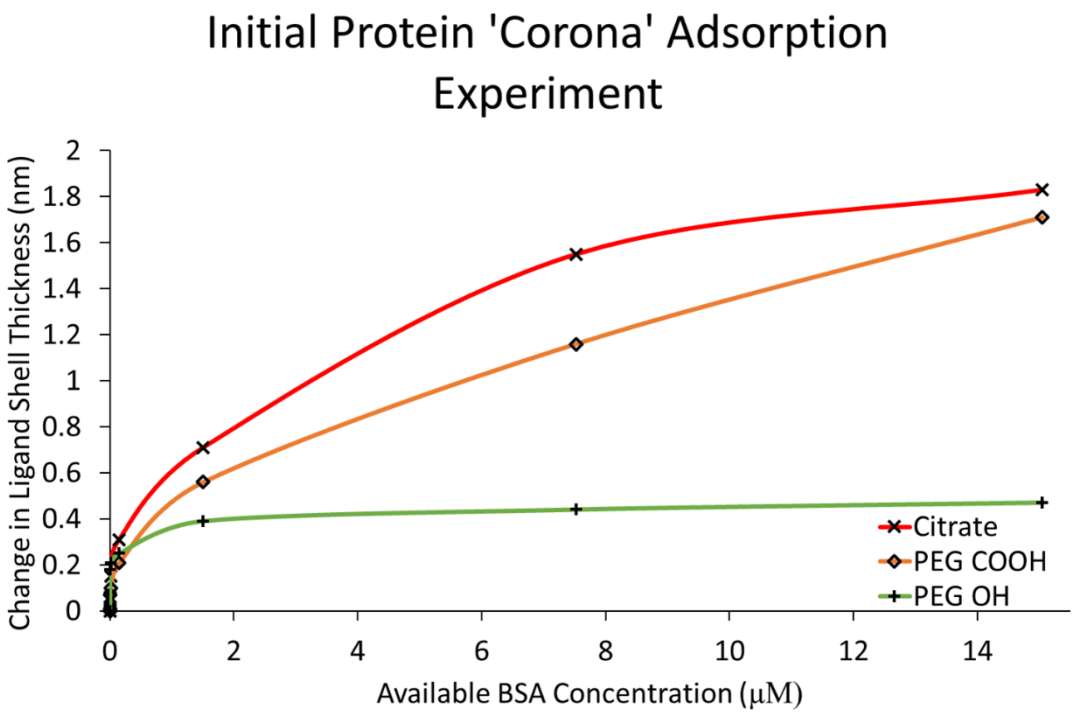

Figure 38: Graph showing the growth of the protein 'corona' with increasing BSA concentration. All points are the average of at least three runs of the same experiment.

As can be seen in Figure 38, the PEG OH shows very little change in size with increasing BSA, this was expected as PEG OH has limited biological interactions. The

citrate and PEH COOH GNPs appear to show the formation of a layer of approximately 1.8 nm thickness and the adsorption does not plateau within the range observed. Very little adsorption was seen before incubation in a BSA concentration of 0.01µM and in a native cellular environment, protein concentrations can get much higher than 15µM, so these experiments were repeated over a larger concentration range (0.001-660µM, Figure 39).

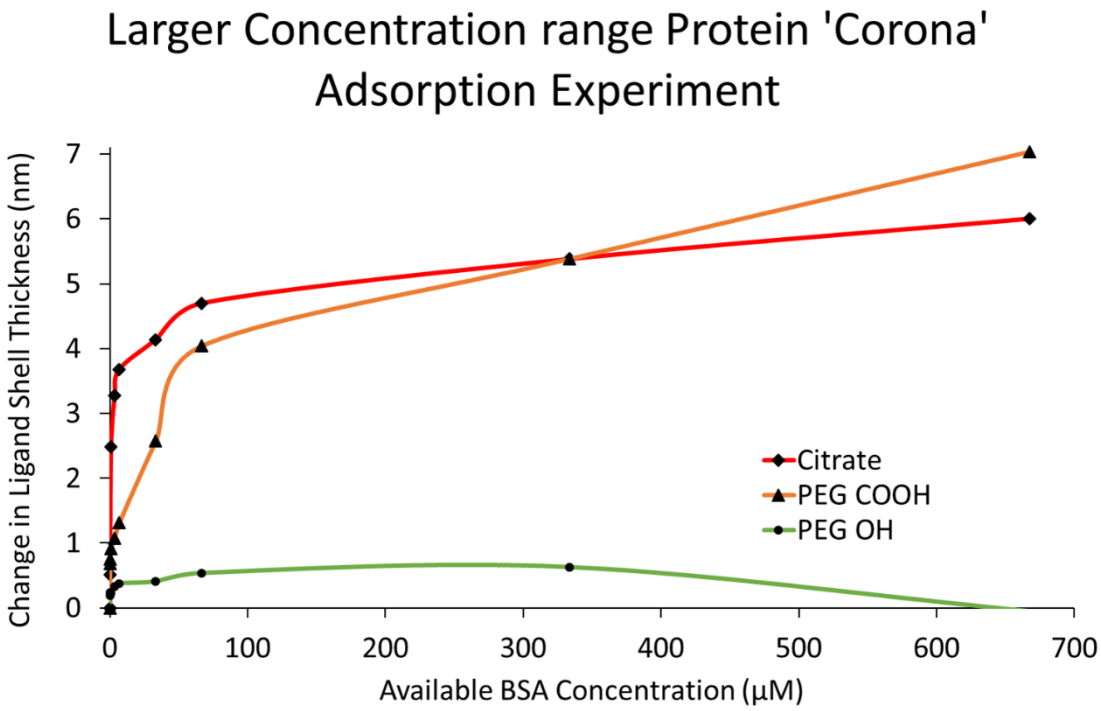

Figure 39: Graph showing the protein 'corona' growth over an extended range of BSA concentrations. All points are the average of at least three runs of the same experiment.

The PEG OH GNPs still showed no appreciable adsorption, even at the higher BSA concentrations, interestingly the last point on this graph returns to the original size even on repeated measurements. The larger BSA concentration range shows a higher level of protein adsorption. For the citrate and PEG COOH samples an adsorption of

approximately 6 nm thick layer of protein was seen. Given the measurements of the BSA protein (see Figure 8) this 6 nm thickness of capping ligand could be either, a bilayer of the BSA protein bound to the particle by its 'triangular' face or the BSA bound via the 'base' of the triangular prism.

A further test was done with particles capped with a 50:50 mix of the PEG OH and COOH and analysis found that these particles have a similar level of adsorption to the pure PEG COOH or citrate GNPs. Further percentages of the mixed PEGs were tested; containing 5:95, 10:90, 20:80, 40:60 ,60:80, 80:20 PEG OH: PEG COOH, however these results were found to be very inconsistent and difficult to reproduce and therefore analyse. We hypothesised that this was likely due to the statistical nature of the mixed capping agent method and patches or gaps in the capping layer, allowing for variable protein adsorption.

This method only gave information about the chemisorbed or 'hard corona' which was complementary to other techniques already used in the literature. We then extended this study further by adding BSA to the sucrose gradient in the CPS, so it contained the same concentration as the samples. A more selective range of BSA concentrations, 0.1 - 500μM, were also used. The previous range was less suited to a logarithmic axis which can help to display the data, also the highest concentration of BSA was a saturated solution, which was very difficult to handle so we lowered this final concentration solution to allow the BSA to be added easily. This addition of protein to the gradient allows the sample to remain in equilibrium during the measurement and therefore provides information about the 'soft corona' or physisorbed proteins. The 'soft corona' cannot be measured by most of the other

established methods and adding BSA to the CPS sucrose gradient allows this phenomenon to be simply measured. This additional BSA allows any protein lost from the corona during centrifugate to be easily replaced. As we were adding BSA to each gradient, a fresh gradient was required for every sample, making the measurements a bit more time consuming. Also, at higher concentrations, the density and viscosity of the gradient would be affected but by running our usual PVC standard before each measurement, the machine's software could account for these changes. Below is a comparison of the size shifts for citrate with BSA present (Figure 40, Right) and absent (Figure 40, Left) from the gradient.

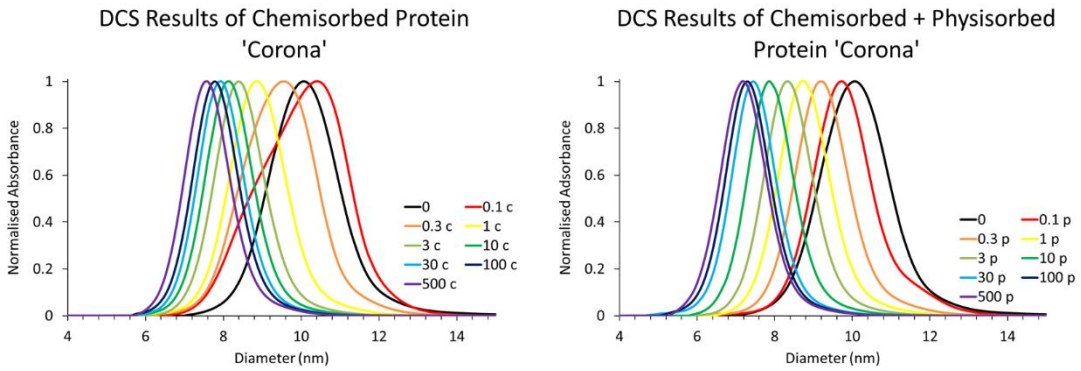

Figure 40: DCS results comparing a sucrose gradient and a gradient containing BSA. The graph labelled chemisorbed is a sucrose only gradient whereas the one labelled chemisorbed + physisorbed is a sucrose and BSA gradient.

Figure 40 demonstrates that with BSA added to the sucrose gradient (Figure 40, Right) all measurements shift marginally to smaller reported sizes (and therefore larger actual size) with a larger overall change in size (0.4 nm before deconvolution). Also, when BSA was not present in the gradient (Figure 40, Left) the initial measurement at lower BSA concentration had a different peak shape which appears

to be caused by the BSA not being present in large enough quantities to fully replace the citrate on the GNP and hence introducing polydispersity to the sample, affecting the measurement. The PEG OH GNPs showed no appreciable changes, as expected, as there is very little protein adsorption to begin with; and the PEG COOH also showed very similar results to the citrate samples. Figure 41 shows the deconvoluted data represented as before, with each graph showing a separation of the physisorbed and chemisorbed layers.

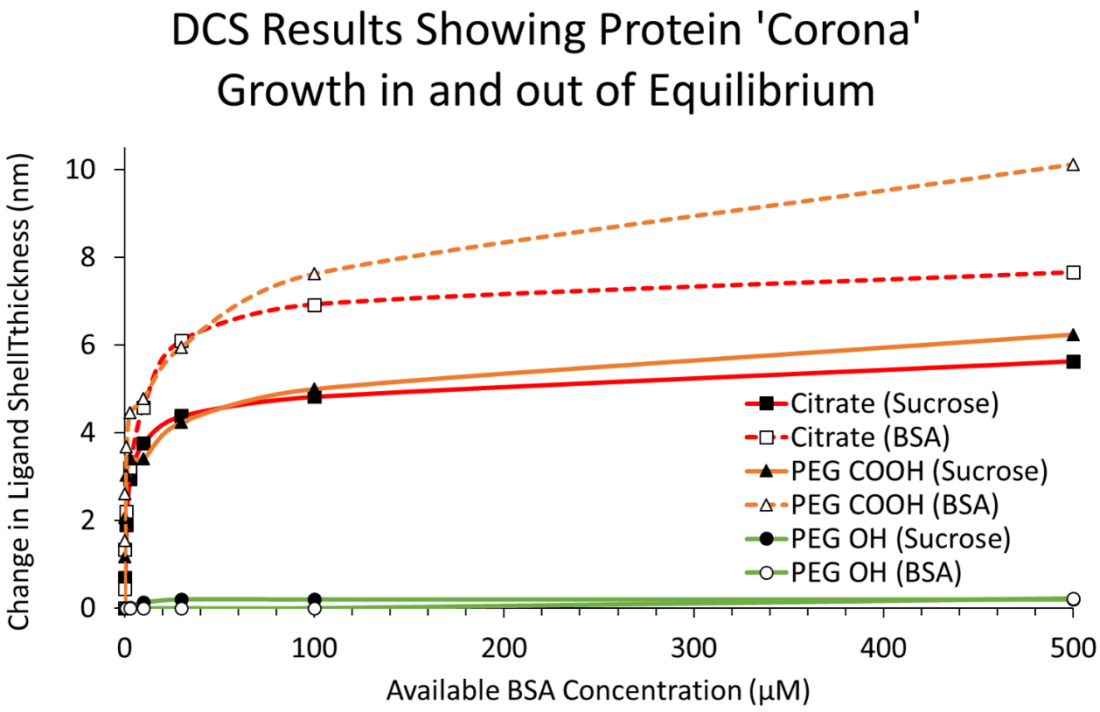

Figure 41: Graph showing the difference in shift for the three particle types in a sucrose gradient (solid line and filled points) and sucrose/BSA gradient (dashed line and hollow points). All points are the average of at least three runs of the same experiment.

As can be seen in Figure 41 the PEG OH shows little difference, as expected and the citrate and PEG COOH in sucrose gradient alone produces a similar trend. However,

the sucrose/BSA gradients for both the citrate and PEG COOH GNPs showed a much thicker layer of protein around these particles, the latter being almost twice the thickness seen in the purely sucrose gradient.

There are several caveats with claiming that the sucrose gradient data corresponds to only the chemisorbed layer including whether all the physisorbed BSA is removed during the measurement which would prevent the physisorbed BSA from altering the measurement. It is also important for our analysis that the chemisorbed layer has reached full equilibrium and that this process isn't reversible within the time frame of the DCS experiments.

A sample of citrate particles were incubated with a concentration of BSA (7.2μM) for time intervals ranging from 15 seconds to 24 hours, before analysing using DCS to observe any change in the reported shell thickness, the results are given below.

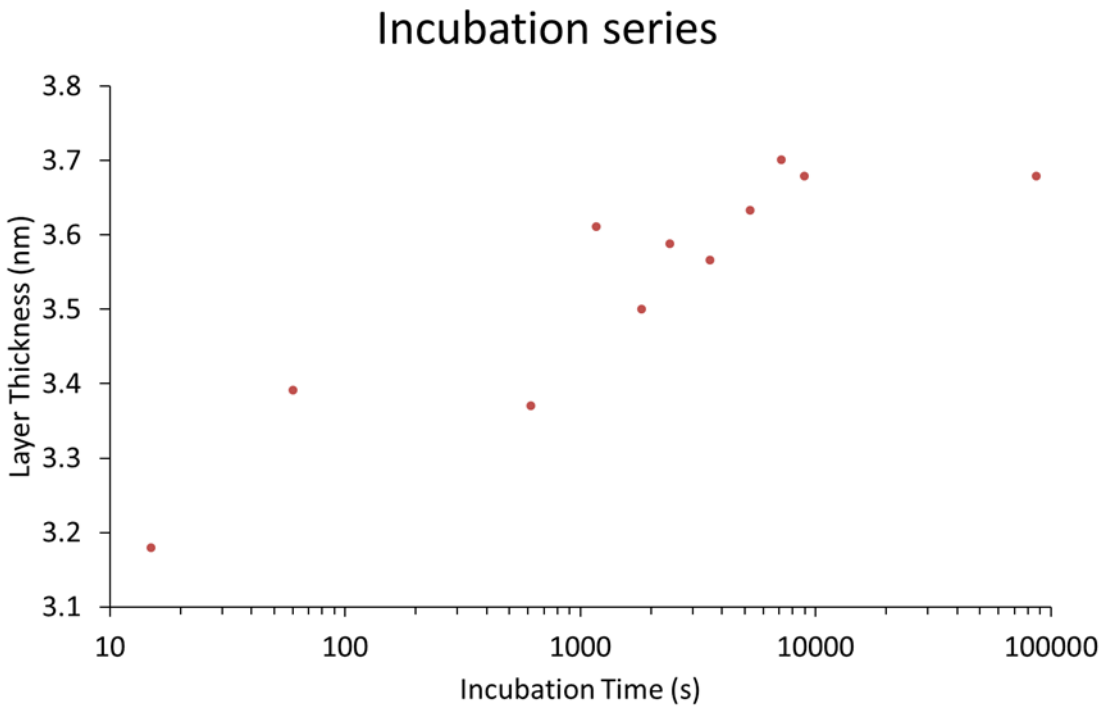

Figure 42: Graph plotting deconvoluted layer thickness (nm) against incubation time (s).

Figure 42 demonstrates that a high majority of the BSA binds immediately (approximately 85%) as seen by the increase in shell thickness, during this experiment additional BSA was slowly added after the initial incubation with more BSA being added up to 2 hours later. After two hours and also 24 hours after the incubation there was no appreciable change in size, as can be seen by the relative straight line made by the final three points in Figure 42. As all samples were incubated for at least 24 hours before analysing it was a reasonable assumption that the chemisorbed layer was fully formed and had reached equilibrium before analysis. This time resolution was larger than reported in some literature which attempted kinetics measurements[2,57,120] but found comparable findings that the corona is formed quickly, but stated that a longer incubation time is required for full equilibrium to be reached. The slow 'settling' of the protein 'corona', even in this simplified system was

in agreement with the fields hypothesis, that the formation of the 'corona' is a complex kinetic process involving competition for sites by various different serums and components[10,11,14,121].

A series of experiments were designed where three samples of all the differently capped particles were incubated in 100μM BSA (this concentration was chosen as there is an appreciable difference between the gradient ± sucrose measurements at this concentration), then one sample was kept as a control, and the other two were centrifuged and cleaned 3 times to remove all excess BSA (the citrate particles were re-dispersed in citrate solution (40mM) to ensure no aggregation and the others were re-dispersed in MQ water). After the final cleaning run, one sample of each GNP was re-dispersed in fresh 100μM BSA solution. The samples were then immediately analysed and then analysed a second time 24 hours later (after 24 hours the sample was tested in both a sucrose and BSA containing gradient), the deconvoluted shell thickness values of this test are given below in Table 3 for comparison (The PEG OH values are not included as no change was seen, consistent with our previously results).

Conditions		**Citrate (nm)**	**PEG COOH (nm)**
Process	**Gradient**		
Control (immediate)	Sucrose	5.56	4.24
Cleaned (immediate)	Sucrose	5.53	3.93

Cleaned then BSA (immediate)	Sucrose	5.63	3.98
Control (24 hours)	Sucrose	5.25	4.20
Cleaned (24 hours)	Sucrose	5.43	4.02
Cleaned then BSA (24 hours)	Sucrose	5.56	3.93
Control (24 hours)	BSA	7.67	6.10
Cleaned (24 hours)	BSA	7.11	5.64
Cleaned then BSA (24 hours)	BSA	6.95	5.93

Table 3: Table of control experiments, demonstrating the minimal deviation of the results before and after cleaning and therefore the rapid removal of physisorbed protein and the strength of the chemisorbed. PEG OH results not shown due negligible change.

The citrate data above shows little change to the sample in a purely sucrose gradient when run immediately (within the error of the measurements themselves at the high concentrations of BSA) indicating that the physisorbed BSA is removed by centrifugation within the time frame of the DCS measurement and has little effect on the final value. This also supports the hypothesis that the chemisorbed layer is very strongly bound to the particle and is not removed even when exposed to a citrate solution for 24 hours. Interestingly, when the citrate GNPs were run in a BSA/sucrose gradient, all samples gave a higher measurement when compared to the control sample, implying the physisorbed BSA layer can be readily re-adsorbed after cleaning and in the case of the cleaned sample even gained during the measurement from the BSA included in the gradient. The difference between the control and the reintroduced BSA is larger than expected and could potentially be due to the longer (now closer to 48 hour) incubation or due to the deconvolution variation at higher concentrations of BSA. The PEG COOH sample shows the same trend, including in the

reintroduction of BSA with a slightly larger deviation in the latter results, which can be attributed to the larger effect of the uncertainty in density for the deconvolution of the PEG COOH samples (Table 3). These experiments gave us reasonable confidence that the sucrose gradient only shows changes that are due to the strongly bound chemisorbed layer and the BSA/sucrose gradients allow the measurement and analysis of the chemisorbed and physisorbed layer, as was hypothesised.

As discussed in the introduction the model used to describe the adsorption of proteins to GNPs within this field is the Hill model[51,60,61]. Figure 43 contains graphs with a more detailed breakdown of the adsorption isotherms and for the citrate, a fit line for the Hill model.

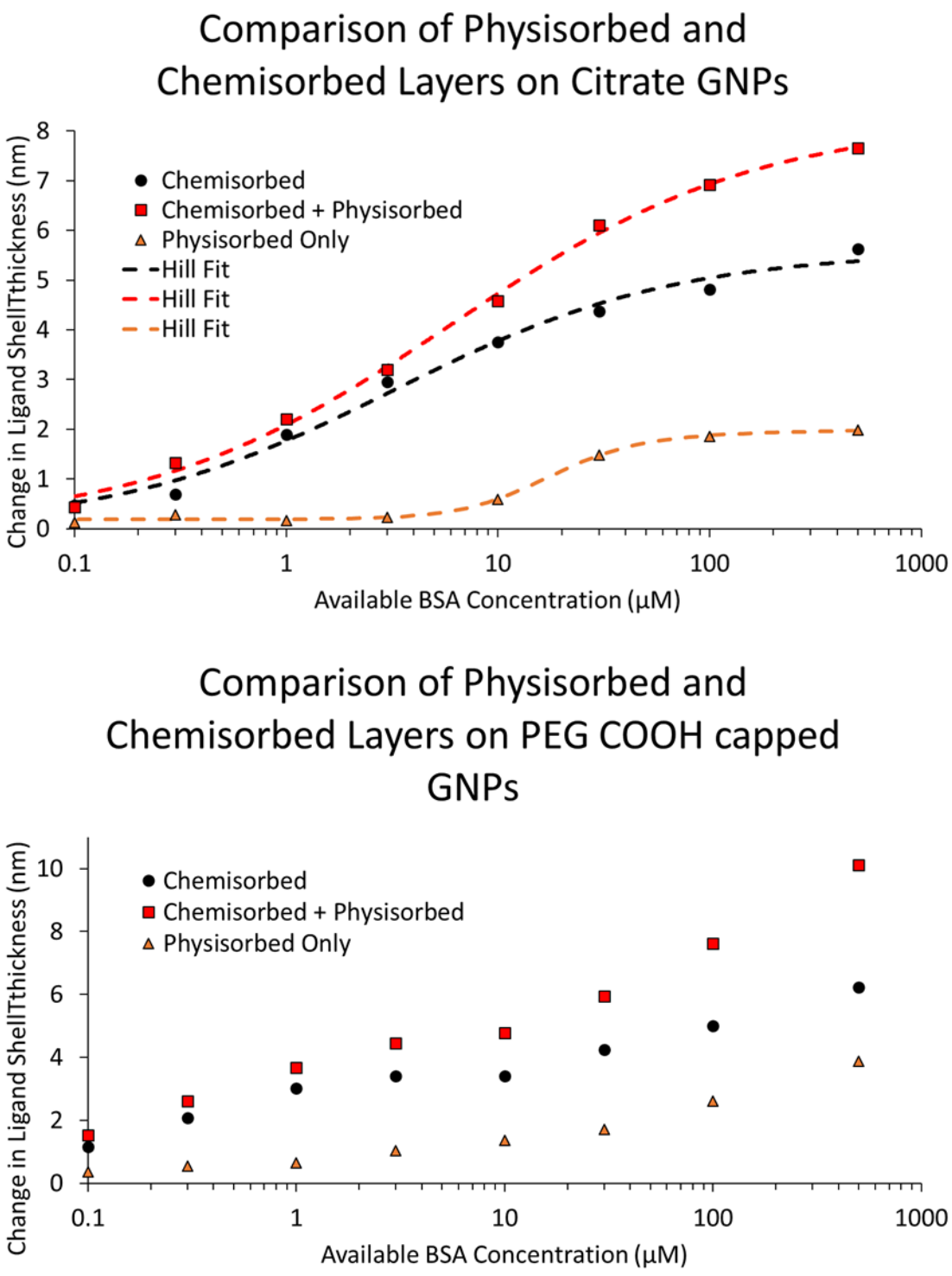

Figure 43: Top graph shows the absorption isotherm of the separate chemisorbed and physisorbed layers, as well as them combined; the Hill model fits are presented as dashed lines. In the bottom graph the absorption isotherm of the chemisorbed and physisorbed layers as well as them both combined are shown, this time for PEG COOH GNPs. In both graphs all points are the average of at least three runs of the same experiment.

From the graphs, it could be seen that a full chemisorbed layer likely forms at approximately 5µM BSA concentration and at higher than 10µM BSA concentration, the adsorption of the protein is much more dependent on the BSA available in the gradient. As can be seen in the graph above, the citrate data for both the chemisorbed (sucrose gradient, black) and the chemisorbed + physisorbed (BSA gradient, red) fit well with the Hill model. Even the difference between the two (orange) which represents the physisorbed layer, shows a good fit to the Hill model. The respective Chi-Sqr and R-Sqr values for each fit being: chemisorbed/black, 0.0567 and 0.985; chemisorbed + physisorbed/red, 0.0274 and 0.996; physisorbed alone/orange, 0.0199 and 0.969. These fits provide the following data: chemisorbed/black; N_{max} of 5.6±0.28 nm, KD of 3.2±0.8µM, and a Hill coefficient n of 0.65±0.08; chemisorbed + physisorbed/red; N_{max} of 8.2±0.26 nm, KD of 6.0±0.96µM, and a Hill coefficient n of 0.6±0.04; lastly the physisorbed alone/orange; N_{max} of 2.0±0.14 nm, KD of 16.4±3.57µM, and a Hill coefficient n of 1.32±0.31. The maximum thickness of the chemisorbed layer fits well with the BSA standing on the GNP surface by the base of the 'triangular' shape and the physisorbed thickness is likely due to BSA settling into the gaps or loosely attaching to itself. The KD values are similar to values found in previous studies for analogous proteins and particles[55,122,123]. A Hill coefficient of <1 for the chemisorbed layer is indicative of non-cooperative binding, which fits with the hypothesis that the BSA is replacing the citrate on the GNP surface and competing for binding sites. Whereas, the Hill coefficient for the physisorbed layer on its own being >1 is indicative of co-operative binding, which supports our hypothesis that the physisorbed BSA is binding to the BSA already present. The data obtained for the combined chemisorbed and physisorbed layers are difficult to

attribute to certain binding as this data is likely the combination of these two separate binding schemes.

The PEG COOH provided very poor fitting to the Hill model, with values being obtainable but no real conclusion could be made for a binding regime due to uncertainty of measurements in the larger concentrations which deviated from the model. The Hill coefficients suggested a highly non-co-operative binding regime for the PEG COOH GNPs, but the quantitative values provide little information due to the ill-fitting model.

The BSA protein is approximately an equilateral triangle in shape, with a height of approximately 6 nm and an estimated thickness of 2.5 nm (Figure 44). For the PEG COOH, the adsorption values derived from the DCS data strongly suggest a strongly bound protein 'corona' of the upright BSA forming the chemisorbed layer with a maximum value of 6.24 nm. Also, the BSA gradient measurements show a thickness of approximately 1.6 times the sucrose gradient with a maximum value of 10.11 nm, this thickness would strongly suggest an incomplete multi-layer of additional BSA forming on top of the chemisorbed BSA. This incomplete layer could also explain the lack of agreement with the Hill model for this data set, as the model does not account for multiple layers. These values are in agreement with the previous methods including, Tsai D.H. Et. al.[55] and others[56] which observed a similar trend with GNPs using DLS, however these results were reported in much larger particles than we have used in this project and they failed to obtain the same level of accuracy for smaller particles (10-50 nm[31]). Also, in this paper, the DLS could not be used to measure the particles in equilibrium with a BSA solution (they were cleaned first[122]) so by using

this method, only the chemisorbed layer was observed in that study. In the presence of high BSA concentrations, the DLS results can become greatly distorted by the protein and aggregates of unbound BSA; at the highest concentrations, only the BSA aggregate size is reported as it becomes the dominant species in the sample. Below are the reported maxima for our samples that were measured in the final set of our DCS data which confirmed the issues seen in published work by another group[122].

BSA Concentration (µM)	Citrate (nm)	PEG COOH (nm)	PEG OH (nm)
0	9.665	13.22	12.97
0.1	12.6	16.88	13.92
0.3	12.06	18.2	20.67
1	14.01	20.33	13.33
3	23.16	16.3	13.98
10	18.46	24.78	11.14
30	5.521	36.55	12.03
100	4.719	19.46	12.86
500	3.141	1.485	1.64

Table 4: DLS results showing the shift of GNPs incubated in BSA with no cleaning.

In table 4, the citrate GNPs show a smaller but similar absorbance for the chemisorbed layer with a maximum value of 5.63 nm for the shell thickness, this

would also suggest the BSA in an upright position. In the below image of the BSA the only surface available cysteine (this cysteine is also not involved in a disulfide bridge) is highlighted and enlarged (yellow sphere), this cysteine is in the base of the BSA and is likely the binding point to the GNP supporting this theory.

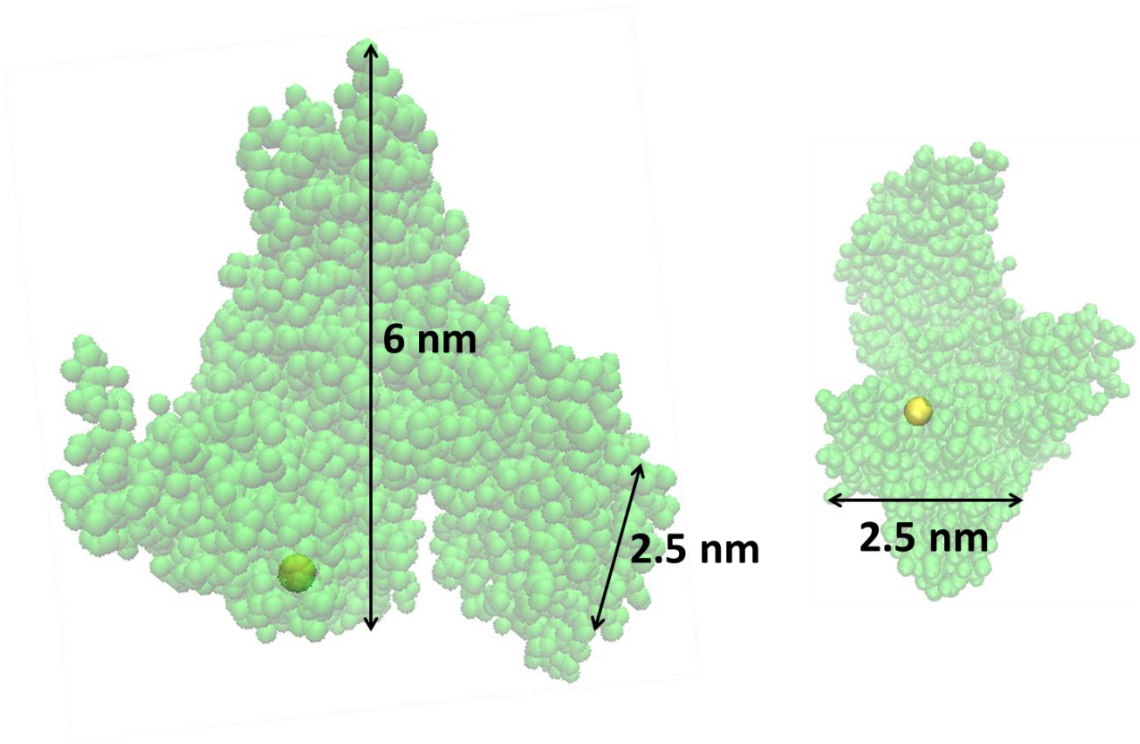

Figure 44: The structure of BSA. The yellow sphere is enlarged to highlighted to indicate the presence of the surface available cysteine.

Further data to support the hypothesis that the BSA is adsorbing directly to the GNP surface, is the UV-Vis spectra of the particles (Figure 45). As can be seen in Figure 45, there is a drastic shift in the SPR maxima of approximately 4 nm and an increase in absorbance, until the BSA is the dominant species close to the particle changing the molar absorption coefficient (ε) thus, changing the absorbance value. This change levels out when there is no longer any citrate present and it is purely BSA, however,

BSA has some absorbance around 300-400 nm (it is yellowish in colour) which as it increases in concentration contributes to this part of the spectra. There are no observed shifts for the other particles which agrees with the hypothesis that BSA does not replace the PEGs. The PEGs do show some minor changes in absorbance due to the presence of BSA in the 300-400 nm region.

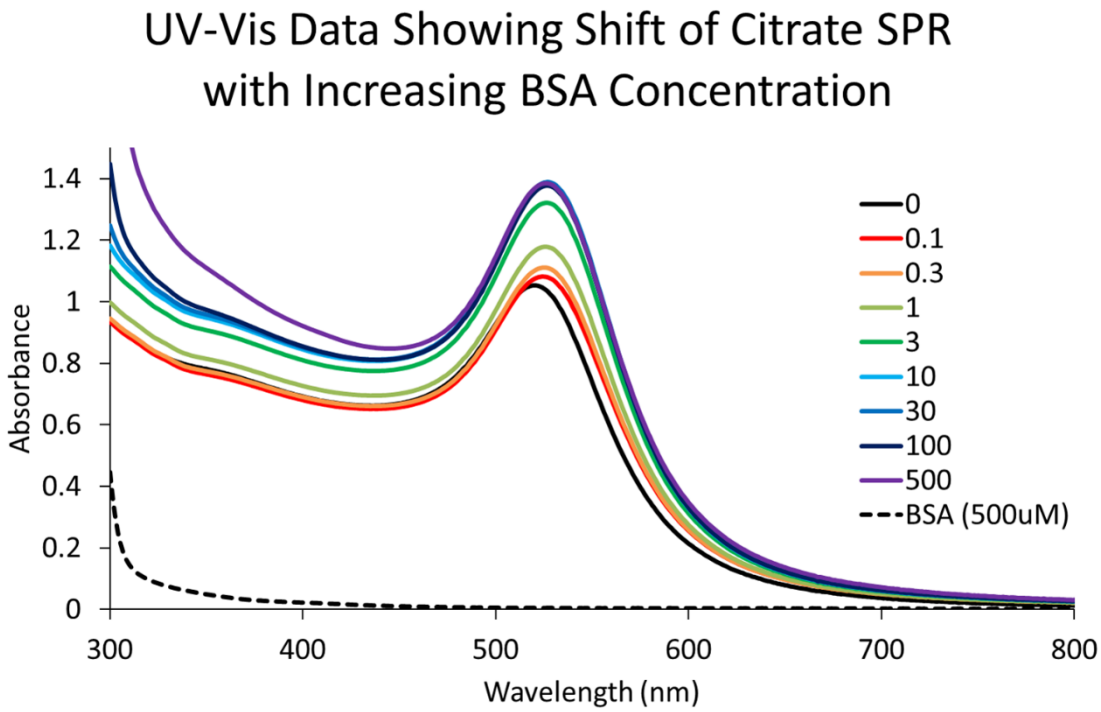

Figure 45: UV-Vis data showing the shift in Citrate GNPs SPR with increasing BSA concentration (µM

The exchange of the citrate with BSA has been demonstrated by other methods in agreement with our findings[123]. Given the information above, below is a cartoon showing the possible structure and orientation of the protein corona as suggested by our data on the two different GNPs, citrate (Figure 46, Right) and PEG COOH (Figure 46, Left); representing both the chemisorbed (black) and the physisorbed layer (red).

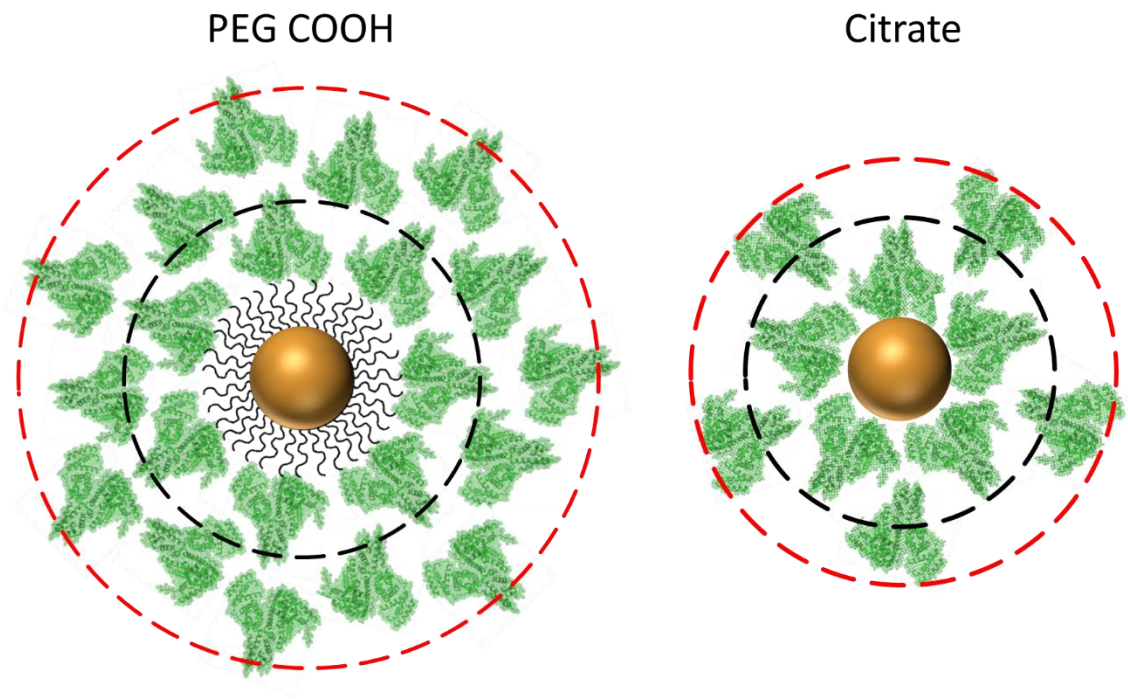

Figure 46: Cartoon of the hypothesised 'corona' formation around two different GNPs, Citrate on the right and PEG COOH on the left; both the chemisorbed (black dashed circle) and the physisorbed layer (red dashed circle) are included.

Given the information provided by the DCS and our complementary method, we can be reasonably confident that the DCS can be used to measure the chemisorbed protein corona of GNPs. Also, after addition of BSA to the sucrose gradient to maintain equilibrium, the physisorbed protein 'corona' growth can also be observed; something not achievable by many of the previous published studies.

Chapter 5

The following work was done in direct collaboration with the Prof P. E. Jensen group at Copenhagen University. The transit peptide purification and initial import study were done by me in Copenhagen but the repeat was done by our collaborators, following my protocol. This chapter's focus is on extending the DCS research done previously to a more practical 'real world' application, as well as preliminary work focused on creating nanoparticle-biological hybrids for energy harvesting.

This body of work was split into two parts: first, we investigated the functionalisation of gold nanoparticles to a section of Photosystem 1 (PS1) and characterising the systems created as well as assessing whether they are still electronically functional; second, we aimed to create systems containing gold nanoparticles attached to transit peptides to allow the internalisation or import of gold nanoparticles into the chloroplasts to create the systems in-vivo.

There is work done previously in the literature (ref) that uses gold electrodes instead to directly bind to PS1; our work here focuses on the binding to GNPs as the long-term aim is to possibly internalise these systems. The internalised systems might allow for short chains to be formed to an external electrode creating a living energy source with plant cells; or to allow for externally driving production of certain molecules of interest expanding on the work already done by our collaborators.

5.1 – Gold Nanoparticle – Photosystem 1 Hybrids

Work done previously by our collaborators at the Plant and Environmental Science Department in Copenhagen University, Denmark, introduced mutations into the photosystem 1 proteins to create available cysteines with the potential to bind to the surface of gold nanoparticles. Several mutations were tested in positions close to reaction centres to allow for electron transfer. All the selective mutations were tested for availability of binding by using solvent accessibility testing pioneered by Frolov et.al[83,124], all work was done by a previous PhD student from our collaborators (Lærke Műnter Lassen, Thesis Chapter 5).

The best mutation options were selected, accounting for closeness to electron centres and availability for binding to gold nanoparticles. The two mutations that met the criteria best were B and C (positions are highlighted in the image below, Figure 47). Mutation B (purple highlighted amino acid in Figure 47) located at the bottom of the PS1, in the peptides B sub-unit and positioned ~20Å from the special chlorophyll pair P700 (1.3.1 – Photosystem 1). Mutation C (yellow highlighted amino acid Figure 47) located at the top of the PS1, in the peptide C sub-unit and positioned ~13Å from the B iron cluster in the ferro-doxin site (see section 1.3.1 – Photosystem 1).

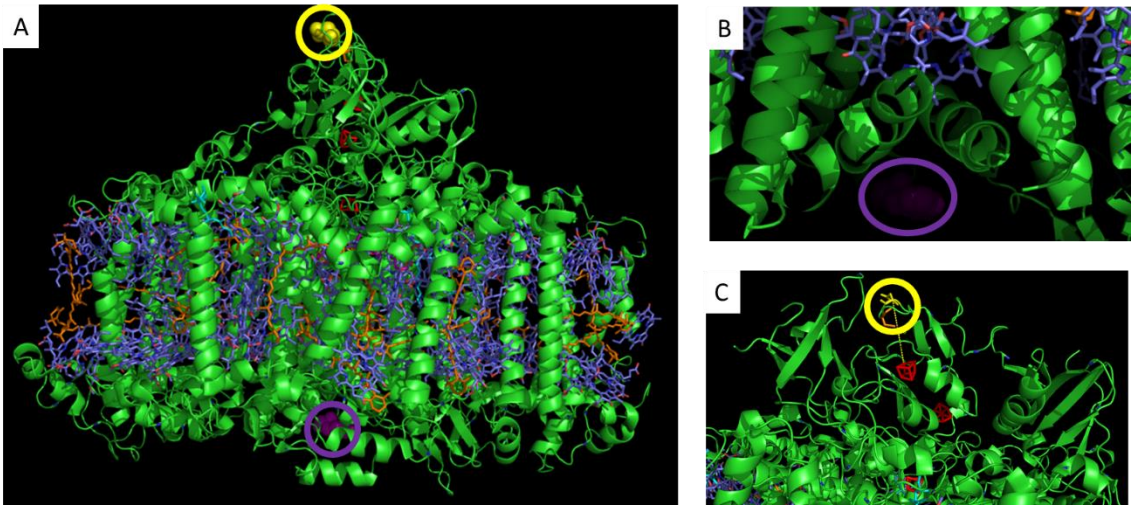

Figure 47: A. PS1 protein structure (image made in pymol, using PDB structural data 1JBO); B. Close-up of mutation site B; C. Close- up of mutation site C. Mutation C is highlight and circled in yellow in all images; mutation B is highlighted and circled in all images in purple[125].

Four versions of PS1 were extracted from the thylakoid membranes of cyanobacteria, *Synechococcus* sp PCC 7002, wild type (PS1 W.T.), single mutant C (PS1 C), single mutant B (PS1 B) and double mutant B and C (PS1 BC). The PS1 complexes were purified using sucrose gradient centrifugation techniques, and the PS1 systems flash frozen and stored at -80^{o}C in a cryo-freezer until needed and then they could be stored at -20^{o}C for a few months. Also, as previously discussed in section 1.3.1 – Photosystem 1, there has been work previously done on similar systems and the aim of these experiments was to create a more ordered way of forming these systems with the gold nanoparticles, with the possibility of forming oriented multi-layers. The mutations located at the top and the bottom of the protein were hypothesised to allow the peptide to orientate with respect to the nanoparticle in a way that would allow us to direct electron flow either into or out of the systems through the GNPs. This would allow for energy collection or into the systems driving production of

proteins[126]. With the double mutant allowing for strings of alternating particles and PS1.

To protect the photosystems, they were stored in light-proof cases and only ever handled in a dark box. The dark box we used was a large faraday cage, with all holes covered in duct tape and a large sheet of light-proof fabric affixed to the cage to drape over the opening when in use. A green light was used inside the dark box when needed as this would not be absorbed by the PS1s.

The initial experiments investigated whether the PS1 systems could bind to the nanoparticles. Samples of citrate particles were mixed with PS1 in a 1:1 ratio. The mixtures were always kept in the dark box until measurements were taken to prevent any breakdown or damage to the PS1. The samples were examined using UV-Vis spectrometry and the resultant spectra was analysed to quickly confirm if binding had occurred between the GNPs and PS1s by a change of the SPR frequency (spectra given below in Figure 48).

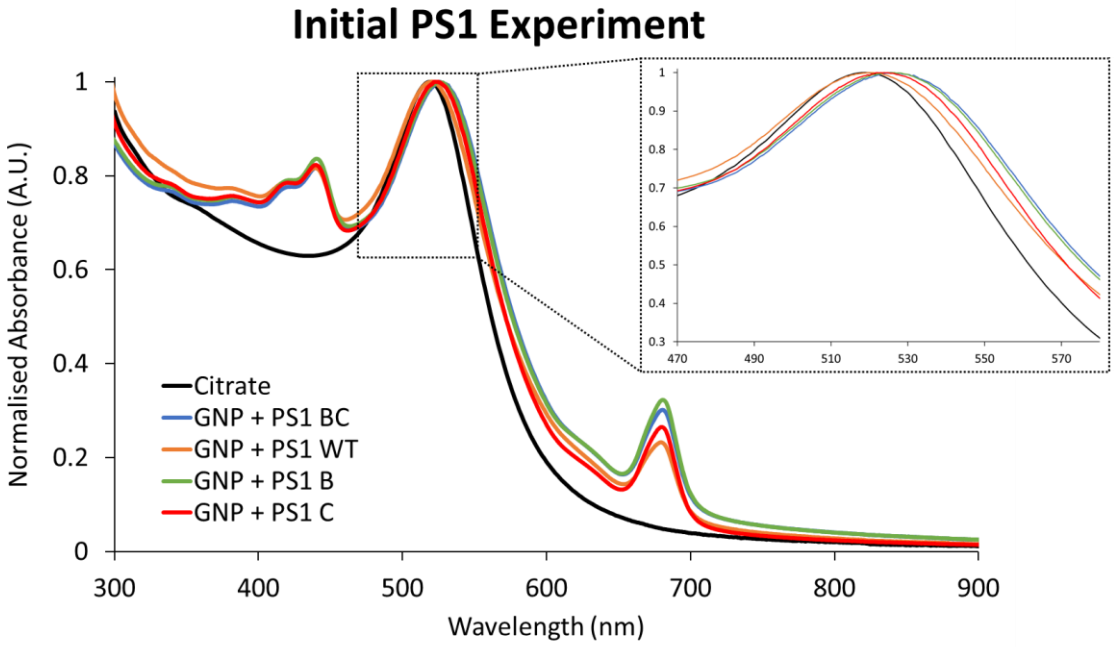

Figure 48: PS1 mutants appear to shift the SPR frequency of GNPs and hence, appear to bind. UV-Vis spectra comparing the initial GNP and PS1 binding experiments. Inset shows an enlarged y-axis cross section, showing the SPR band shift.

The initial UV-Vis data showed an expected red shift in the SPR frequency for the three mutated PS1 mixtures, which was a good initial indication that binding had occurred. The wild type PS1 WT does not result in a significant shift from the initial GNP SPR band which was anticipated as the PS1 WT was not expected to bind and hence would not shift the SPR. However, after being left for more than a few hours the sample began to precipitate and form a film on the bottom of the sample vial. The film retained the nanoparticles red colouring, implying that this was not aggregation (as this would alter the colour of the solution) and appeared to re-disperse fully upon shaking. A series of UV-Vis measurements were performed on the mixtures at regular time intervals to observe the precipitation process (Figure 49), as well as measurements of aliquots of the precipitate taken when full precipitation had occurred (Figure 49).

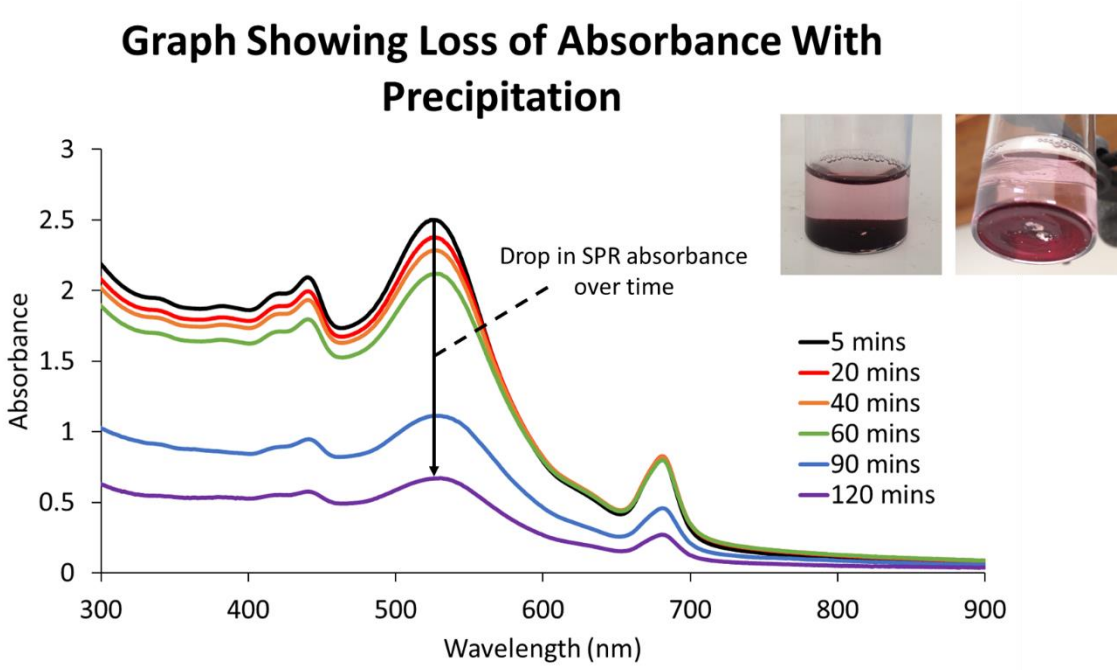

Figure 49: Mixtures of GNP and mutated PS1 appear to precipitate over time and decrease the SPR absorbance of the sample. UV-Vis spectra showing a drop in absorbance of SPR and PS1 absorbance bands[127] as the system precipitates. Inset shows the sample when this precipitation has occurred and the precipitated layer and how the colour is retained. The system shown in the inset figure is GNP + PS1 B.

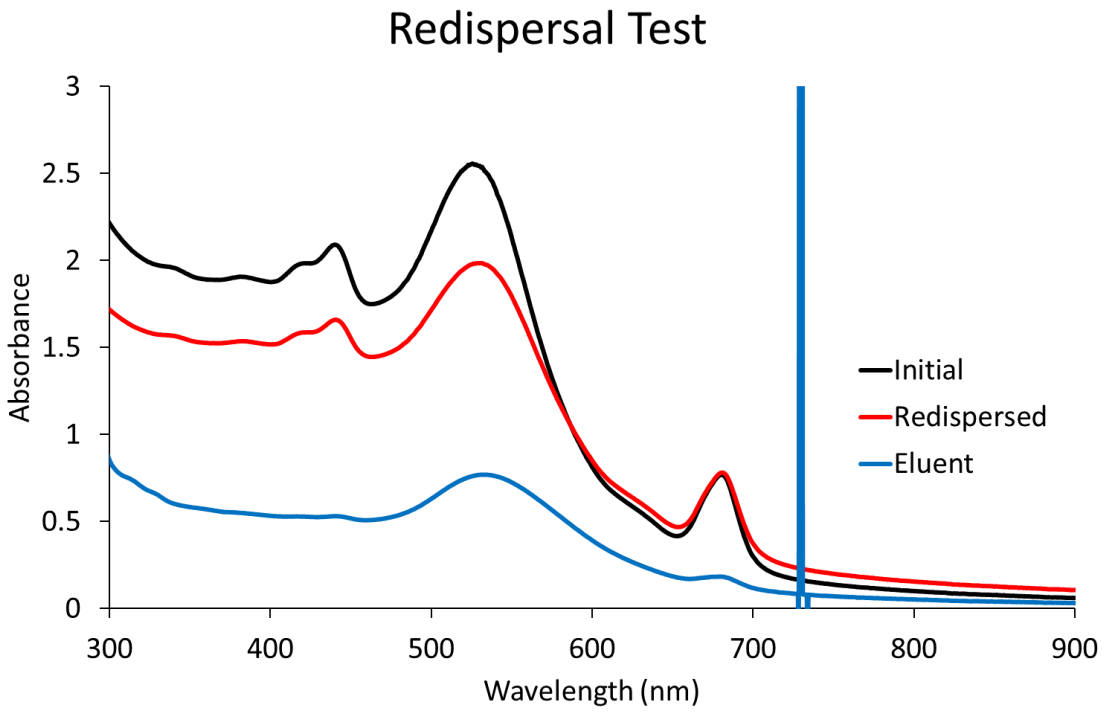

Figure 50: A UV-Vis graph comparing GNP + PS1 BC: the initial (black) spectra of the mixture; the eluent (blue) of the sample decanted of the precipitation; the eluent when added back to the sample and resdispersed (red) using sonication. Spike at ~730nm is a defect in the spectra.

In Figure 50 it can be seen that over a very short period of time the GNP and PS1 mixture precipitates out of solution. This was the case for both PS1 B and PS1 BC mixtures, but no obvious precipitation was seen for the PS1 WT and PS1 C samples. Figure 50 shows that approximately 70% of the system has precipitated out within two hours of mixing. This figure also shows that the system does not fully redisperse as initially expected. Increasing the ratio between the mutated PS1 and GNP increased the rate of precipitation and decreased the effect of redispersing the systems afterwards. The samples were also analysed by DLS however, the data was inconsistent and no obvious trends were apparent, so it is not included in this thesis.

As can be seen in Figure 47 PS1 is a roughly cylindrical protein complex. PS1 is a membrane protein and in its normal cellular environment the 'circular' faces which are hydrophilic are exposed above and below the membrane, whereas the 'cylindrical' face is hydrophobic and surrounded by a phospholipid bi-layer membrane. Also, when in its normal cellular environment PS1 exist as singular complexes embedded in the membrane or they can group together to form trimer rafts. As such the proteins isolated from the thylakoid membranes will naturally aggregate to form larger units that can subsequently collect together into incrementally larger rafts to limit the exposed hydrophobic surfaces. To prevent this aggregation in our experiments, a surfactant, n-Dodecyl β-D-maltoside, was added to the mixture before addition of the PS1; but this surfactant was added at the lowest concentration possible (around 1% w/w) to prevent it forming a stabilising layer around the nanoparticles or interfering with the GNP binding to the PS1. The choice of surfactant and the minimum concentration were conditions provided by our collaborators and represented an estimate of the minimum conditions to maintain stability for the PS1s while limiting the aforementioned effects on the GNPs. The addition of the surfactant prevented any signs of precipitation for at least 1-2 weeks from addition and the system did not fully precipitate even after approximately 6-8 weeks. All precipitation that did occur was reversible. These new GNP/mutated PS1 mixtures containing surfactant were analysed using UV-Vis to verify that no significant precipitation had occurred (spectra shown below Figure 51).

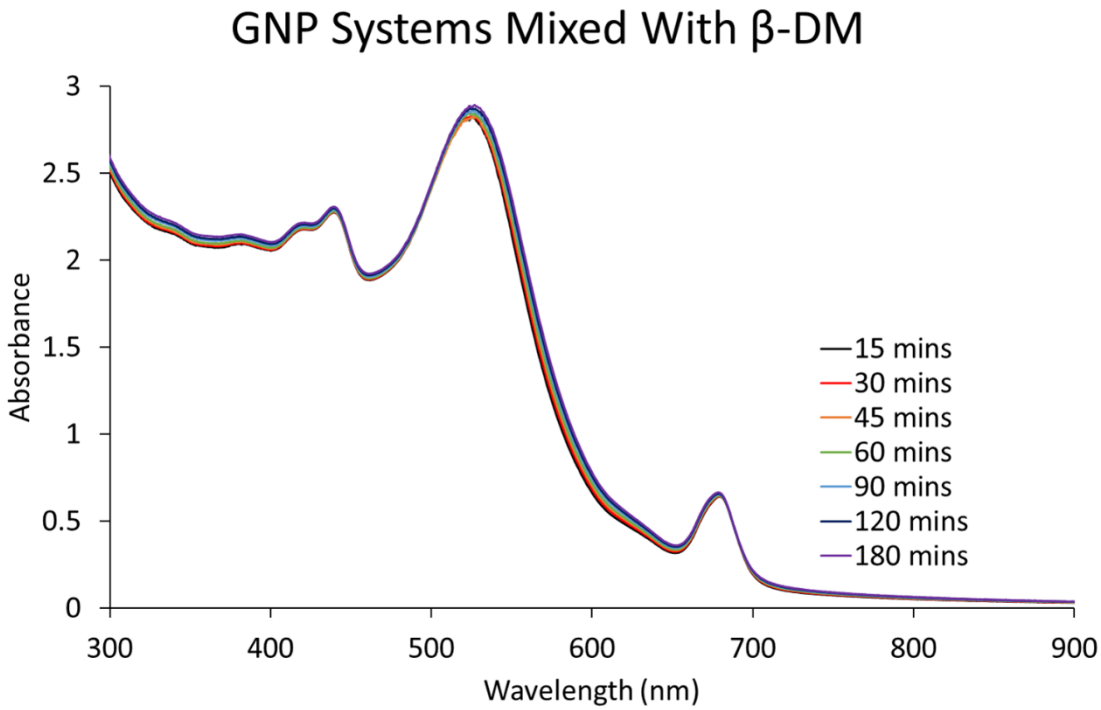

Figure 51: A UV-Vis graph showing that after β-DM was added to the mixes the spectra no longer demonstrates a decrease in SPR absorbance.

The shifts in SPR are still seen that indicate binding is still occurring between the GNP and mutated PS1. Spectra were run on GNPs samples with just β-DM added and no SPR shift was seen, indicating that β-DM had no effect on the spectra. Additional DLS analysis of the systems after addition of β-DM, was inconsistent but did show that the systems are significantly larger than the initial GNPs are in size. The size of the surfactant containing GNP/PS1 systems were then measured using the DCS to investigate whether DCS could be utilised to measure the size of a more applied example of protein structures. If successful, the DCS could potentially provide more information about the size of the different systems. The measurements are compared below in Figure 52.

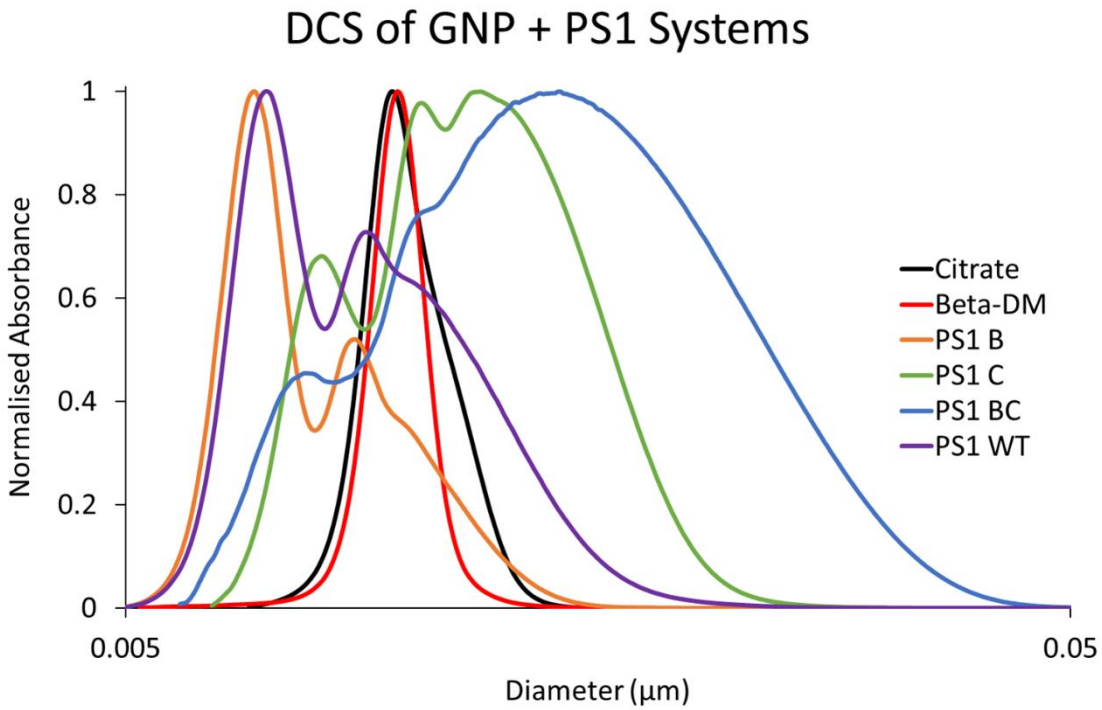

Figure 52: Shown are the DCS measurements of the various GNP + PS1 systems with added beta-DM surfactant.

Citrate, shown in black (Figure 52), was present in the graph as a reference point. The citrate particles with only β-DM added caused a minor shift in size, probably attributable to a physisorbed layer of the surfactant. The runs shown in Figure 52 were highly reproducible and apart from minor changes in the intensity of some of the peaks, these runs are representative of multiple runs of the same sample and were also repeatable across multiple samples. All the systems had an initial smaller peak, ranging from a shell thickness of approximately 3.5-7nm using a density of 1.2g/L, which would suggest an incomplete layer of PS1 on the nanoparticle surface. Each system also has a secondary and some also a tertiary peak that then becomes a broad hump, this is very indicative of flocculation/aggregation in a sample; with the second and third peak being double and triple the volume of the primary peak,

respectively. This is a good indication of the systems building up into longer strings of GNPs and PS1. The double mutant and mutant C in particular, seem to form much longer chains, with the double mutant forming the longest. However, due to the fact that the shell is incomplete, and the larger structures will be non-spherical and possibly rod like or amorphous in structure, the hypothesised formation of longer strings is not conclusive.

As the construction of the nanoparticle and PS1 systems and precisely what structure they form was inconclusive from the previous methods, electron microscopy was used in an attempt to visualise the systems. Initially, samples of the various PS1s without GNPs were drop cast onto TEM grids and stained with uranyl acetate and lead citrate (Figure 53); as previously discussed (1.2.5 - Electron Microscopies) this provided a better contrast as the PS1 protein consists of relatively low electron density atoms and thus will not diffract a large number of electrons making it difficult to image. TEM images of the GNP/PS1 mixtures were then visualised. Although multiple initial images were taken of the systems without staining, below is a comparison of the initial stained samples.

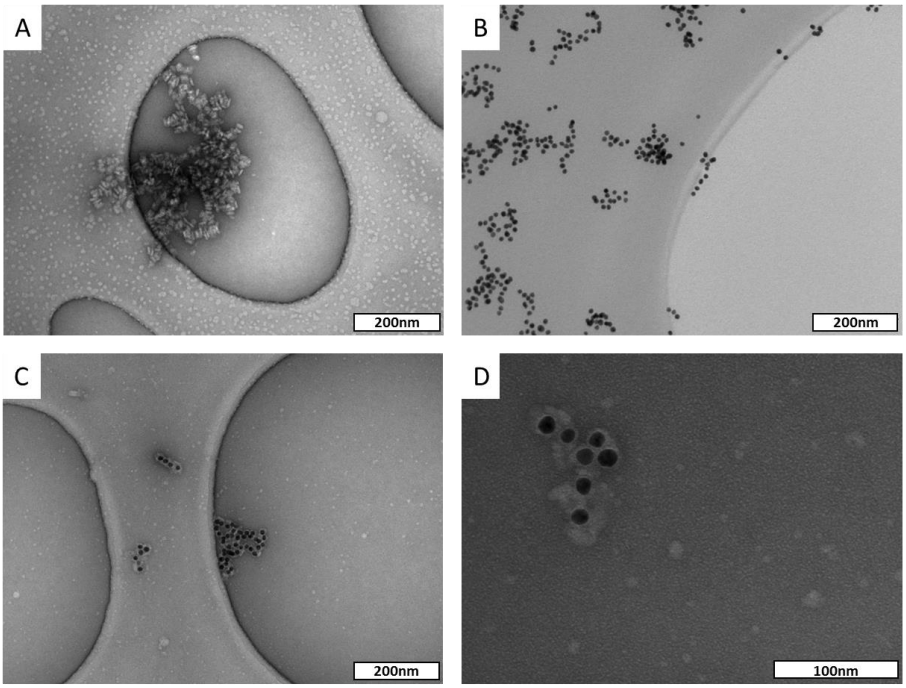

Figure 53: TEM images are shown of systems on holey carbon grid. A. Scale bar 200nm, post-stained photosystem 1. B. Scale bar 200nm, GNPs and PS1 with no post staining. C. Scale bar 200nm, post-stained GNPs and PS1 systems. D.Cryo-TEM on holey carbon grids of the same system Scale bar 100nm.

In the figure above (Figure 53) image A. shows that after staining the photosystems are easily visible as rod like shapes on their side or as rough circles when visualised from the top or bottom. Image B. shows the nanoparticles and photosystems without staining and the particles appear to form clusters with reasonably large spaces between them at certain points, most likely attributable to the photosystems. Image C. shows these systems after post staining where the photosystems can be seen bound to nanoparticles, either in chains or in clusters. Image D. shows the same system but with higher magnification. Cryo TEM, SEM and ESEM were used to image these systems and Figure 53 contains representative images; there are no significant differences between any of the systems when imaged.

All the methods used suggested that the synthesis of these hybrid systems had been successful, but differences in structure and orientation of the systems as they form complexes was not clear but analysing this in solution this would be difficult. Next, we wanted to address two outstanding questions: first, could the systems be assembled and added in an oriented way on a surface; second, could we verify that the photosystems were still electronically active and could act as energy collecting systems as seen previously in the literature.

The first step to address these questions we attempted to attach the GNP/PS1 systems to coated gold slides to investigate their electrochemical activity. To prevent any interference in the measurements by the gold on the slide interacting with the solvent we blocked the solvents access to the gold electrode surface. This was accomplished by incubating the slide with hexane dithiol for a week to ensure a thick 'brush' coating that was able to completely protect the slide from the solvent. Hexane dithiol has a sulfur atom available at each terminus, allowing it to bind to the gold surface and GNPs, hexane dithiol is also short enough to allow electron transfer from particles to the gold slide.

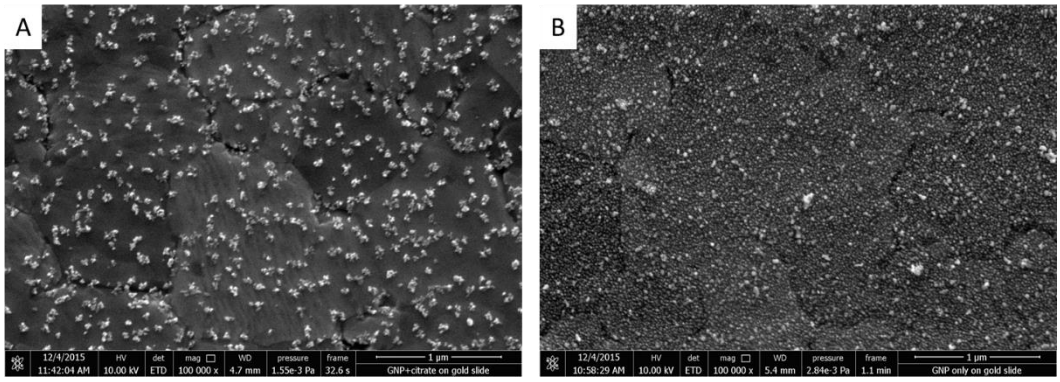

Figure 54: SEM images of citrate particles on gold slide. A. Scale bar 1µm, particles with no extra citrate addition. B. Scale bar 1µm, particles with extra citrate addition.

When the gold slide was incubated for 2 days in just citrate GNPs this caused aggregation of the GNPs on the slide and this aggregation produced a very uneven coverage. This uneven coverage was most likely due to the negative particles repelling each other as they bind to the surface, hence making it difficult to approach the surface without losing their protective citrate layer (Figure 54, A). Adding additional citrate to the particles before incubating the slide, allows for more screening of the particles charges and this in turn resulted in a more even coverage (Figure 54, B), but the amount of citrate added to the particles was carefully controlled otherwise the particles would aggregate.

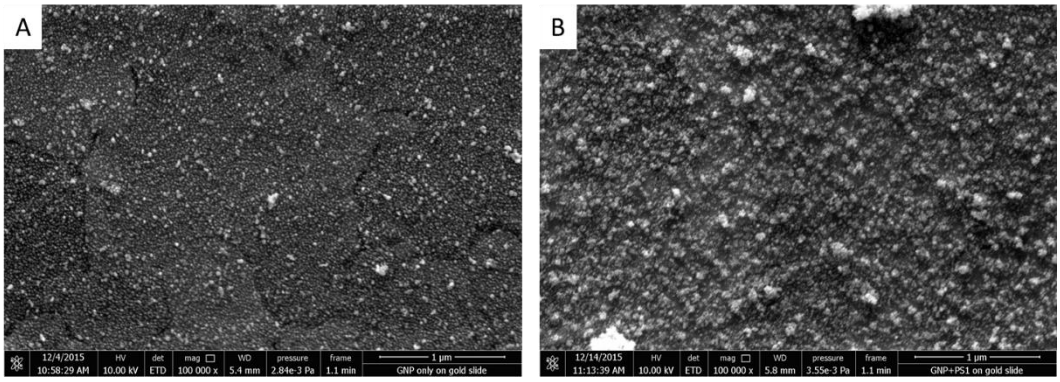

Figure 55: SEM images of citrate particles coated gold slide before and after incubation with PS1. A. Scale bar 1µm, slide before PS1 incubation. B. Scale bar 1µm, slide after PS1 incubation.

As previously discussed (section 1.2.5 - Electron Microscopies) biological material is difficult to image using SEM due to the lack of electron density and the gold slides we used were too large to image in the TEM. However, above is a before (Figure 55, A) and after (Figure 55, B) comparison of the same gold slides after a 2 day incubation in PS1. As can be seen from the images, the beneath structure becomes less well defined, as do the particles structures, which have become larger clusters, and this could be attributed to a layer of obscuring biological material.

The photosystem used in this coating was the PS1 C as this was predicted to orient the PS1 in a certain way that would allow the flow of the electrons to move towards the GNPs and the surface of the gold slide. Preliminary work was done by our collaborators using conductive AFM and electrochemistry to test the electronic viability of the systems on the slide that showed promise but due to time constraints this was not conclusive or reproduced.

5.2 – Gold Nanoparticles for Import into Chloroplasts

5.2.1 – Production and Purification of Transit Peptide

As previously discussed, although chloroplasts have their own DNA and protein transcription centres, they still have genes and protein sequences that have migrated to the main nucleus making import into the chloroplast very important. Chloroplasts therefore have their own import mechanisms, the most common one being the TIC-TOC import mechanism described in the introduction section. This mechanism requires a very specific transport sequence to allow for import through the membrane, as several of these sequences exist the first step in our experiments was to modify and isolate one such protein and attempt to use this transit peptide to functionalise our GNPs.

The protein transport sequence selected was isolated and sequenced from (*Synechococcus* sp PCC 7002) by our collaborators and then modified to include a cysteine to enable it to bind to the GNPs, followed by a sequence of 6 histidines (to allow for easier peptide purification using histidine binding resins), at the opposite end of the peptide to the reading path, to prevent interference with import process.

This sequence was cloned into an *E.coli* expression plasmid, as using *E.coli* as an expression vector is known to allow for a high level of protein expression and hence produce a large quantity of protein with each purification process. The recombinant plasmid was taken up by the *E.coli* from the surrounding media when the sample was

heat shocked, which forces the membrane pores open, the plasmid can then enter the *E.coli* cell and then when rapidly chilled the pores close again. The *E.coli* was then cultured on solid medium in the presence of the antibiotics which the plasmid confers resistance to, therefore allowing only the desired *E.coli* colonies, which have the plasmid present, to grow. In some cases, if the *E.coli* grows rapidly or is left to grow for too long, some colonies can consume all the antibiotic in an area leading to the growth of satellite colonies which form in the antibiotic free zones which do not contain the plasmid, so these colonies were avoided during selection. Colonies were tested for the presence of the plasmid via PCR and gel electrophoresis of the product. PCR works by rapidly increasing the amount of DNA by using a polymerase (taq Phusion from BioRad) and it is focused to just the desired insert by adding in forward and reverse primers (small sections of DNA) for the desired sequence. The PCR product is then dyed (gel red) and separated by gel electrophoresis allowing visualisation to confirm the presence of the insert in the plasmid but also to confirm the size of the DNA is as expected, the outcome is shown below in Figure 56.

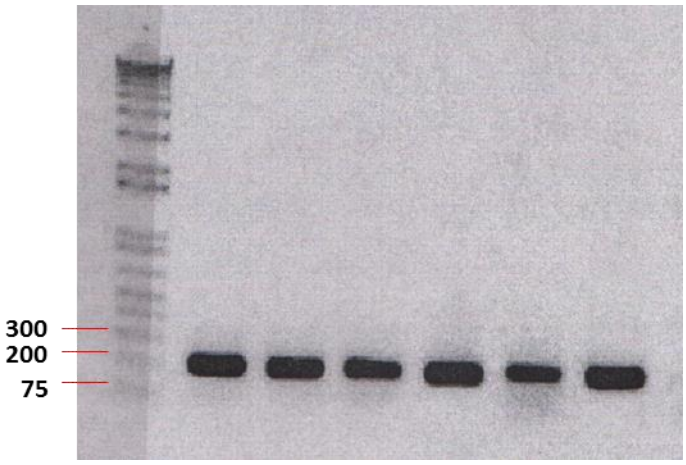

Figure 56: Ladder labels in relevant area are given in base pairs (bp). Image of agarose gel showing bands at approximately 200bp which confirms the presence of our transit peptide insert. (N.B. images were scanned from the lab book so sometimes the tape is present).

As can be seen from the gel, all the tested colonies gave an intense and clear band at around 200bp, which is approximately the length of the desired insert (186bp). After the insert presence had been verified, the *E.coli* were then cultured in much higher volumes to produce a large amount of bacteria for protein production. During the *E.coli* culture process, samples were taken at regular intervals (approximately every hour) to track the growth and a spectrophotometer was used to determine the optical density (O.D.) at a 600nm wavelength; as this is a good indicator of the turbidity of the solution in biological media. Once the O.D. has reached over 0.7 this indicates that the *E.coli* have multiplied so that a high number exist but the E.coli has not yet reached the stationary phase in their growth, hence this is the optimal time for protein production. When the OD is around 0.7 the expression factor (IPTG) was added to the culture batch, to begin expression of the desired peptide, this works by inducing the expression of the plasmid and this part of the peptide is read and transcribed repeatedly to produce high levels of the peptide.

The bacteria culture batch was then concentrated down by centrifugation and flash frozen until use (to prevent peptide degradation), but samples were taken prior and redispersed in a proprietary extraction mixture called BugBuster ® master mix, which extracts proteins from the *E.coli* but also ensured that all inclusion bodies (aggregates of proteins) were fully dissolved. To confirm that the protein production process was successful the BugBuster treated samples were centrifuged and the pellets and supernatants (run in various dilutions) of the sample were run on an SDS-PAGE (Figure 57). The gel was post-stained with Coomassie blue (a protein dye) to look at the total protein in these samples.

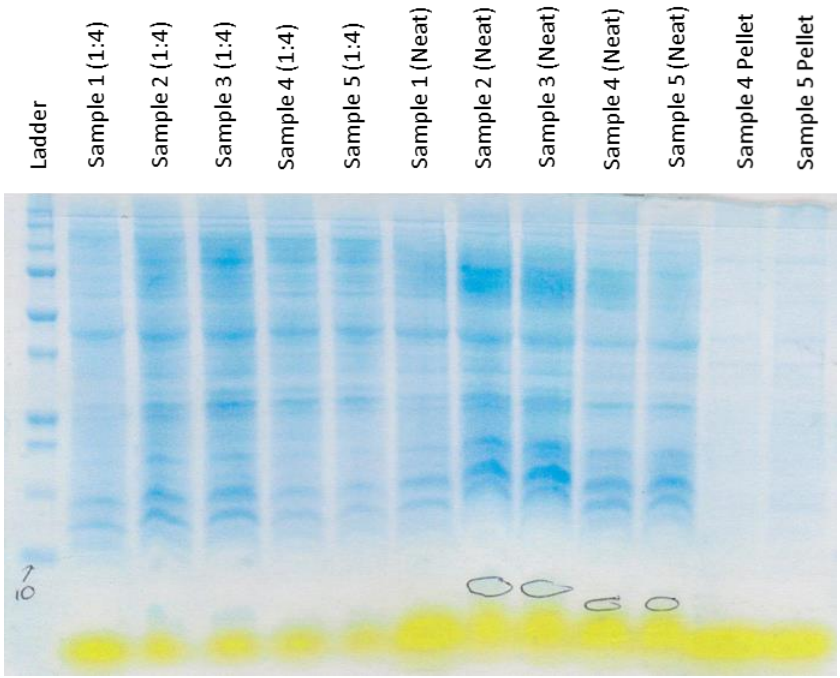

Figure 57: SDS-PAGE gel showing the protein fractions in the cell debris with each sample labelled above the gel. The faint bands where the transit peptide is present are circled in the image. The last relevant band is labelled (10kDa) with the ladder being in kilo-daltons (kDa).

The ladder used for this gel is a Bio-Rad marker ranging from 250-10kDa. The samples going from left to right are: the ladder; the next 5 wells are different samples from the culture supernatant diluted 1:4 with PBS; the next 5 wells are the same samples but undiluted; finally, the last two wells are the pellets from sample 4 and 5 redispersed in PBS (as a control to ensure the peptide is not still in the pellet which is the *E.coli* cell debris). The peptide is visible on the gel and is approximate 6.58kDa in weight, which correlates to its predicted size. So, the desired protein is expressed and can be extracted from inclusion bodies in most samples. However, the band is quite faint, so a much larger culture was grown and the process repeated, samples were taken every hour after the IPTG addition to follow the peptide production.

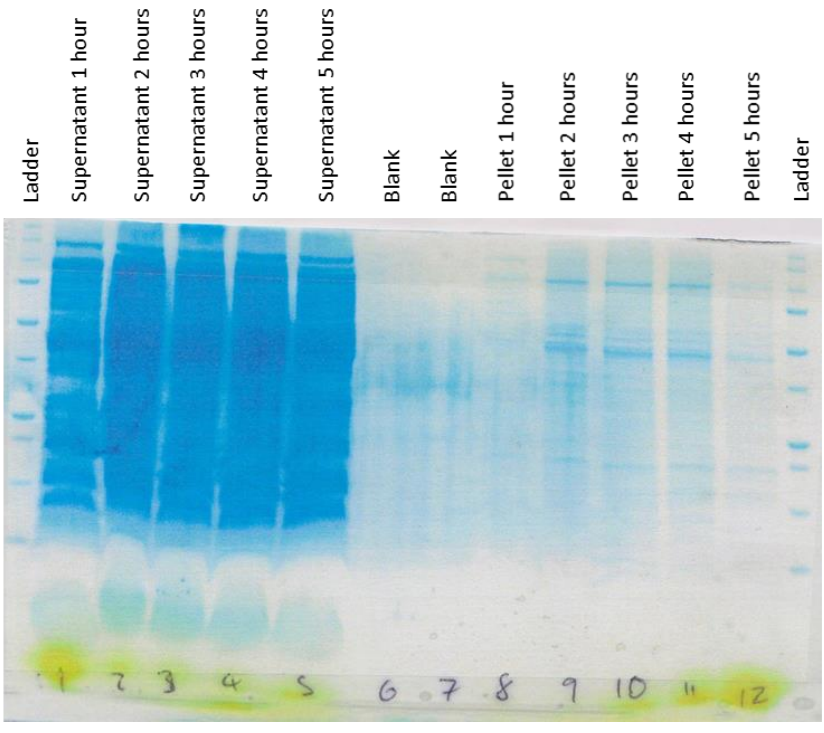

Figure 58: A SDS-PAGE of samples taken from the E.Coli culture at multiple time points after IPTG addition, the supernatant was run after redispersal in Bug Buster ® . The last relevant band from the DNA ladder is labelled (10kDa).

As can be seen from the gel (Figure 58), there is a large amount of the peptide present in the supernatant and not the pellet. From the gel is can be assumed the optimum time for extraction of the peptide or freezing of the sample is between 2-4 hours; as over time the *E.coli* will start to digest the excess peptide. The presence of the large running front (yellow colouring from the DNA dye) is unfortunately quite close to the band we are interested in which makes it more difficult to accurately see the band consistently in these gels, so none stained running buffer was used instead from that point on.

The BugBuster ® master mix was an expensive product that was reserved for preliminary tests where possible. The standard method was to redisperse the cell pellet in a buffer solution (also containing protease inhibitors and kept on ice wherever possible) known to dissolve the inclusion bodies and to use a cell disruption equipment, such as, a cell disrupter or cell 'French' press. The French press was used at 30Kpsi twice to ensure break down of all membranes and inclusion bodies. The buffer used was the 'binding' buffer which contains a standard Tris/HCl buffer (50-100mM at pH 7.4 to prevent peptide precipitation), sodium chloride (0.5M), with a small quantity of imidazole (20-40mM) to prevent the peptide his-tags sticking together but not enough to block them binding to the nickel resins used to purify his-tag peptides.

After French press the resultant supernatant was purified for the transit peptide using fast protein liquid chromatography (FPLC) and a column with divalent nickel resin (purchased as a pre-packed sepharose column from G.E. 2 ml volume). After adding the sample to the resin, it was washed several times with 100% binding buffer.

The purification process was analysed by measuring the A280 absorbance throughout the washing process. By measuring the A280 absorbance of the flow through solution, the protein concentration can be quickly estimated and used to determine at which point the flow through contains little to no protein and has therefore washed any unspecific protein out of the resin. The flow through was collected in one falcon tube (~10ml) until the O.D. became level showing that all unbound protein had been washed through the resin and theoretically the only protein left should be specifically bound to the resin. Next, the running buffer was changed from 100% binding buffer to approximately 40% binding buffer and 60% elution buffer (containing 500mM imidazole, which out competes the his-tag, complexing with the nickel resin and freeing the transit peptide) in 5% increments over an hour. The eluent was then automatically collected in a 96 well plate in 0.5 mL fractions till the O.D. showed that no more protein was being eluted. A final wash through solution (~10 mL) was then passed through the resin consisting of 100% elution buffer and collected in case any proteins remained bound to the column. Below is a representative purification gel and a selection of the fractions with the highest O.D. value.

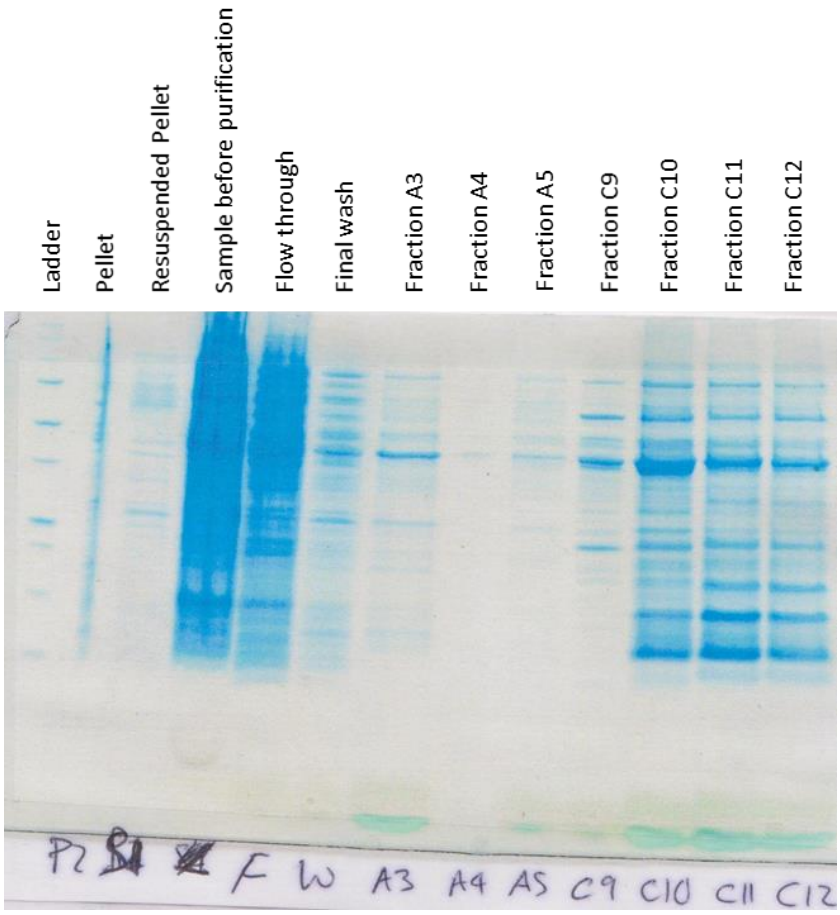

Figure 59: SDS-PAGE gel of the pellet (including the resuspended pellet) and the supernatant before purification, flow through, final wash and various fractions that had high O.D. values. The last relevant band on the DNA ladder is labelled (10kDa).

The gel showed very faint bands (Figure 59) which are around the correct size of the transit peptide in certain elutions but there was also a lot of non-specific protein binding (which is a result of poor purification) in the chosen fractions. However, the band seen around the size of the transit peptide was not present in the sample taken before purification, so this band was probably an artefact introduced by the purification process rather than the transit peptide. To verify the absence of the peptide, a western blot using an antibody specific to the his-tag was used.

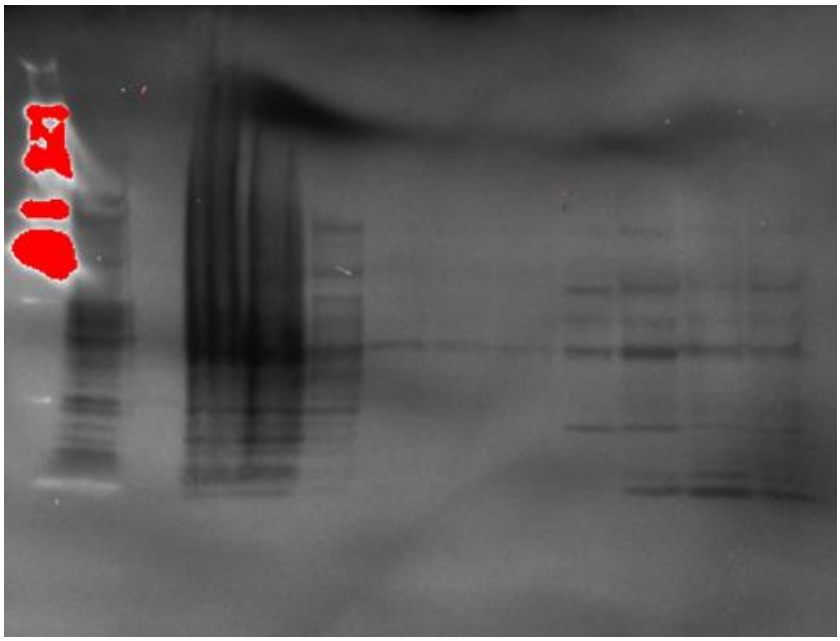

Figure 60: Western blot of the previous SDS-PAGE gel incubated with the anti-His antibody then visualised. Any his-tagged peptides present in the sample should appear very brightly (The bands in red are proteins that are over exposed).

The western blot determined that there are no His-tagged peptides present in this purified sample (Figure 60). Several different binding buffers, with different cell lysing agents were used to dissolve inclusion bodies, however the Bug Buster ® was the only one that seemed to allow the purification of the transit peptide. A small test sample of the cell lysate dissolved in Bug Buster ® was run through multiple different resins but the peptide was only ever present in the flow through, hence was not binding the specific resin, suggesting that the his-tag was not suitable for purifying this peptide or that the tag cloned onto the peptide was not able to properly bind the resin.

Using the ammonium sulfate precipitation peptide purification process, the transit peptide could be purified (by ~70% ammonium sulfate saturation) to the extent that it was the most abundant peptide seen in the gel, but the sample was not 100% pure (data not shown). This purification process works by incrementally increasing the

concentration of the ammonium sulfate (used because of its ability to stabilise peptides and due to its break down into two ions high in the Hofmeister series) causing peptides to 'salt out' and fraction out the sample. Due to time constraints, the process could not be optimised but as mentioned above the protein was quite pure for a biological sample. The peptide was then dialysed in milli-Q water, at least twice over a 12-24 hour period. The peptide was then added to 10 nm citrate GNPs, this size was chosen as they are reasonably easy to image in TEM whilst also being potentially small enough to be imported into chloroplasts. The peptide was added in excess to ensure a full coating of the particles and then centrifuged at least three times to remove any excess unbound transit peptide. The particles were then used in the import study.

5.2.2 – Chloroplast Extraction and Nanoparticle Import

During chloroplast extraction a few precautions were taken due to the nature of the chloroplasts. Chloroplasts can only withstand a small amount of kinetic energy before rupturing, older plants and hence larger plants, have more chloroplasts available due to a larger amount of starting material, however, the older the chloroplasts, the greater the number and size of starch granules present (plant cell energy storage) which can rupture the chloroplasts when centrifuged during extraction. We aimed to extract chloroplasts from young plants to try and minimise the caveats mentioned above. The organism chosen for chloroplast extraction was *Pisum Sativum*, Kelvedon Wonder (peas) and the shoots and leaves were harvested 10-14 days after they were

planted (the plants are grown in optimum conditions in an environmental chamber see methods section 2.12 - *Pisum Sativum* Growth and Chloroplast Extraction and Import). The plants were kept in the dark for at least 24 hours before extraction to force the plants to use stored energy and therefore use up their starch granules wherever possible. The deceleration of the centrifuges used for these experiments was set to as low as possible in an attempt to prevent damage to the chloroplasts during purifications.

After purification, the chloroplasts are initially imaged using light microscopy (Figure 61) to verify the presence of intact chloroplasts before being used immediately afterwards in the import study.

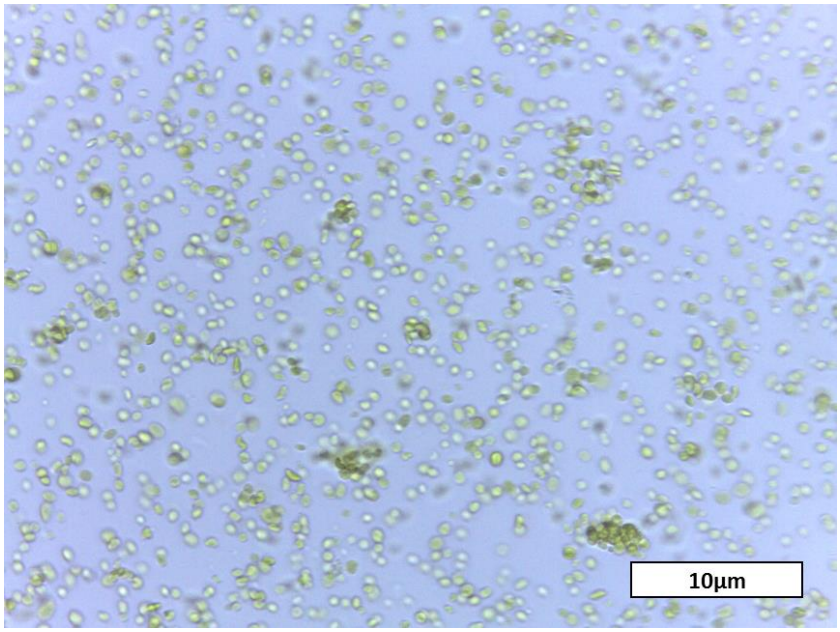

Figure 61: Light Microscope image of intact chloroplast sample.

The initial import study began by adding GNPs to a sample of chloroplasts, containing magnesium salt ATP which is the chloroplasts natural source of energy, this was included to hopefully encourage and aid in rapid import. The samples were then floated in a clear water bath at 25^{o}C and exposed to a high intensity white light source for 30 minutes to encourage rapid photosynthesis and import of any outside material to support this process. The samples were all centrifuged, using the low deceleration conditions again, to remove excess free particles and then separated into two samples. The latter sample had a thermolysin treatment to remove anything stuck to the surface of the chloroplast outer membrane, this provided a control in case particles were internalised, as it would remove any particles that were stuck on the surface but not yet internalised.

After attempted import, the particles and chloroplast samples were fixed using karnovsky's fixant and then pre-stained with osmium tetroxide before being embedded in Spur's resin for imaging. The blocks were then sectioned using a microtome. The initial imaging indicated that the pre-staining did not provide enough contrast, so where appropriate, post staining was performed on the sections. Uranyl acetate and Reynold's lead citrate were used to post stain the samples, with the optimum staining time being two minutes with each (1, 2 and 4 minutes were tested and it is noted in the image caption where the staining time differs in the results shown in this thesis).

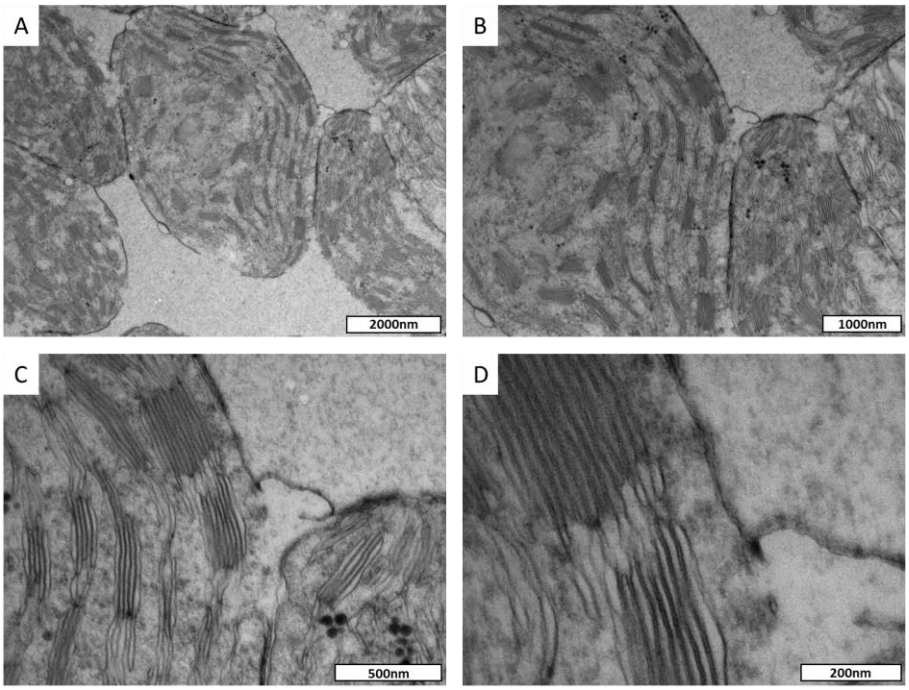

Figure 62: TEM images of post stained Chloroplasts slices 70 nm in thickness. A. scale bar 2000nm, shows a full slice of a chloroplast with other partial chloroplasts. B-D. are further magnifications of part of the same chloroplast.

The chloroplast images seen in Figure 62 are typical of those also seen in the literature and the outer membrane and thylakoid membranes can be clearly seen in the images. The dark spots seen in the images are plastoglobules (globules of plastoglobulin used by the chloroplast for various functions). Three other samples were made during the import study, a particle control with just citrate GNPs added to chloroplasts, to see if they are taken up without the peptide sequence and the third sample was the chloroplast and the transit particles, representative images are shown below for comparison.

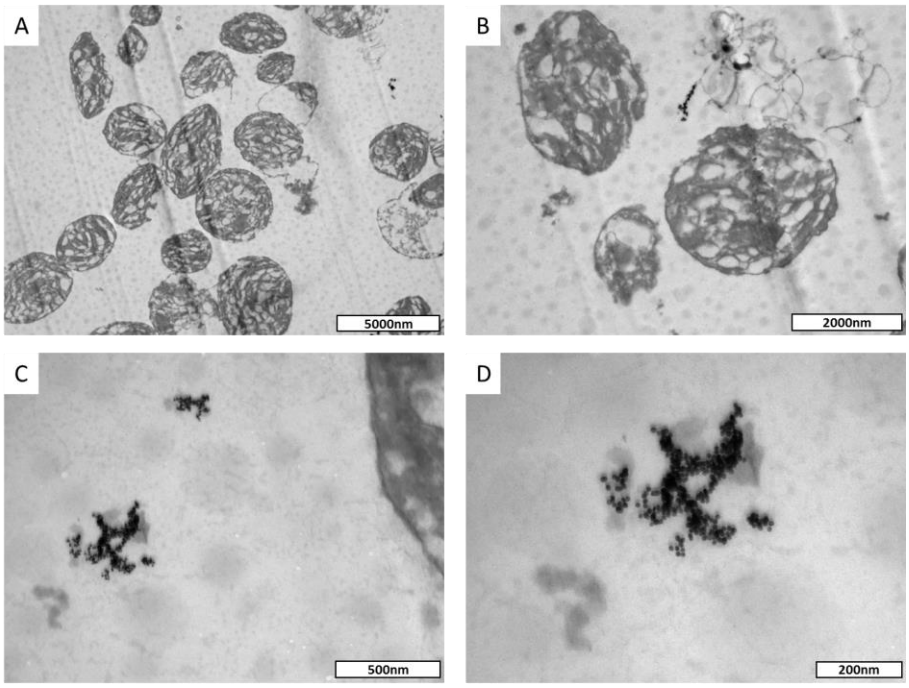

Figure 63: TEM images of post stained chloroplasts incubated with citrate GNPs, slices 70nm in thickness. A. scale bar 5000nm, showing chloroplasts and a patch of nanoparticles. B. scale bar 2000nm, similar subject but further magnification. C-D. close-up of nanoparticle patches.

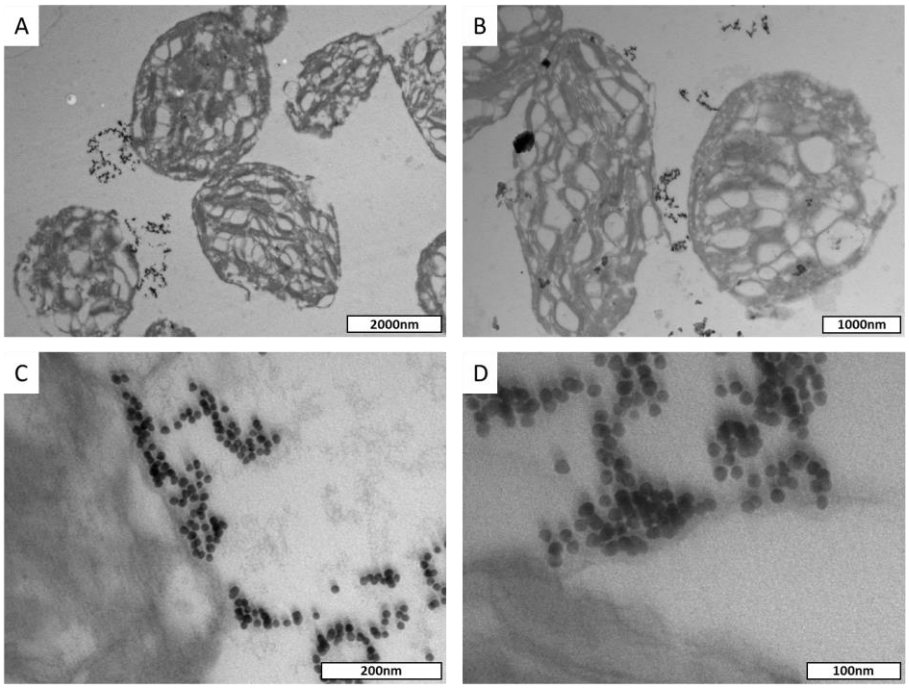

Figure 64: TEM images of post stained (1 minute) chloroplasts incubated with transit peptide coated GNPs, slices 70nm in thickness. A. scale bar 2000nm, showing chloroplasts with nanoparticles near and on the membrane. B. scale bar 1000nm, similar subject but higher magnification. C-D. close-up of nanoparticle patches seen on the chloroplast membranes.

The series of images in Figure 63 demonstrates that there was no obvious uptake with any of the samples tested. The citrate control shows GNPs in small amounts in the solution, but they are not near to the chloroplasts or attached to their membranes. In the close-up images of the citrate particle sample it is clear that the inter-particle core distance is very small or non-existent, so the particles are likely to have aggregated together, which is expected for citrate in biological medium (Figure 63). However, in the transit peptide coated GNP sample, the particles appear in much larger clusters and seem to be exclusively associated with the chloroplast membranes, this could indicate that the particles are getting stuck on the outside at the TIC/TOC channel proteins (Figure 64). The difference between this sample and the control sample does appear to indicate that the transit peptide is at least bringing the GNP to the membrane for import. The sample also shows significant aggregation of the particles, but the lack of a large blue shift in the particle spectra and the larger spacing between particles in the images, would suggest that the cores are not merging and the particles are stable. This effect is most likely due to interactions between the peptide molecule that are coating different nanoparticles. This aggregation could be hindering the import of GNPs into the chloroplasts.

As previously discussed, half of this import experiment was removed and received thermolysin treatment, this is a treatment with a surface 'cleaning' peptide that will cleave any extraneous peptides from the outer membrane of the chloroplast. The samples were then centrifuged to remove any excess particles before fixing. This was a control to determine if the particles were bound to the surface using the transit peptide or just next to the membrane by chance or weaker interactions (Figure 65).

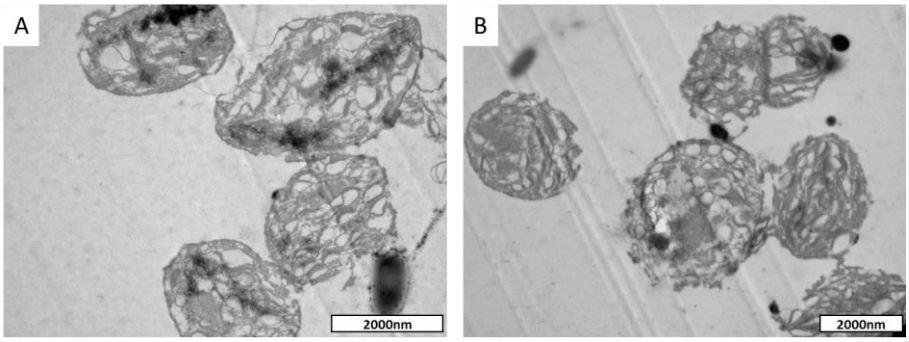

Figure 65: Thermolysin treatment appears to remove the GNP from the chloroplasts indicating that the GNPs are bound to the chloroplast membrane by the transit peptide. TEM images of post stained (1 minute) chloroplasts incubated with transit peptide coated GNPs, then thermolysin treated, slices 70nm in thickness, scale bar 2000nm in both.

The lack of any particles in the second samples would agree with the initial hypothesis that the transit peptide coated particles prior to thermolysin treatment, in Figure 64, were bound to the membrane surface and not there by chance.

There was enough peptide made during the previous bacterial culture for an additional more controlled study. Having a mixed capping layer, consisting of the transit peptide and a short chain PEG ending in an OH group, which is hypothesised to help remove the problem of the peptide-peptide interactions inducing aggregation, whilst maintaining the functionality. Short chain PEG OH's are known to not interact with biological systems and should be short enough so as not to interfere with the transit peptide signalling ability that induces transport to the TIC/TOC machinery. Also, we attempted to optimise the method by using smaller sized nanoparticles (3 nm and 5 nm), in case the size of the particle prevented it from passing through the import channel. The amounts of transit peptide and PEG tested were 1, 5 and 10% transit peptide. Other coatings used in the study were; CALNN as

a negative control as it has not been shown to enable uptake into chloroplasts; CALNN-TAT mixture (95% CALNN, 5% TAT) as this coating has been shown to cause successful uptake in human cells. Unfortunately, the 5 nm particles samples, the 10% transit peptide of the 3nm particles, and the 1 and 10% transit peptide particles aggregated and there was not enough peptide or time to repeat these experiments.

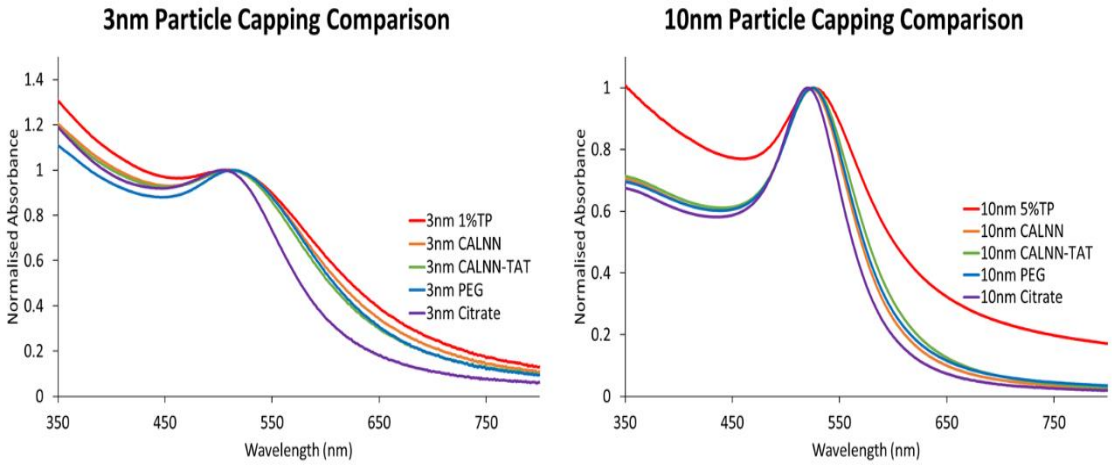

Figure 66: UV-Vis spectra showing shifts for the different capping ligands used. On the left are the 3 nm GNP samples and on the right, are the 10 nm samples. Peaks were normalised

The UV-Vis spectra show clear shifts for all the different capping layers with all the transit peptide samples showing drops in absorbance and a slow precipitation over time (this affect is reversible with shaking, Figure 66). The samples were redispersed before being use in the import study and the previous method was repeated but all samples were thermalized to ensure any uptake is clear for all the samples. Representative images of the all the systems are shown below in Figure 67.

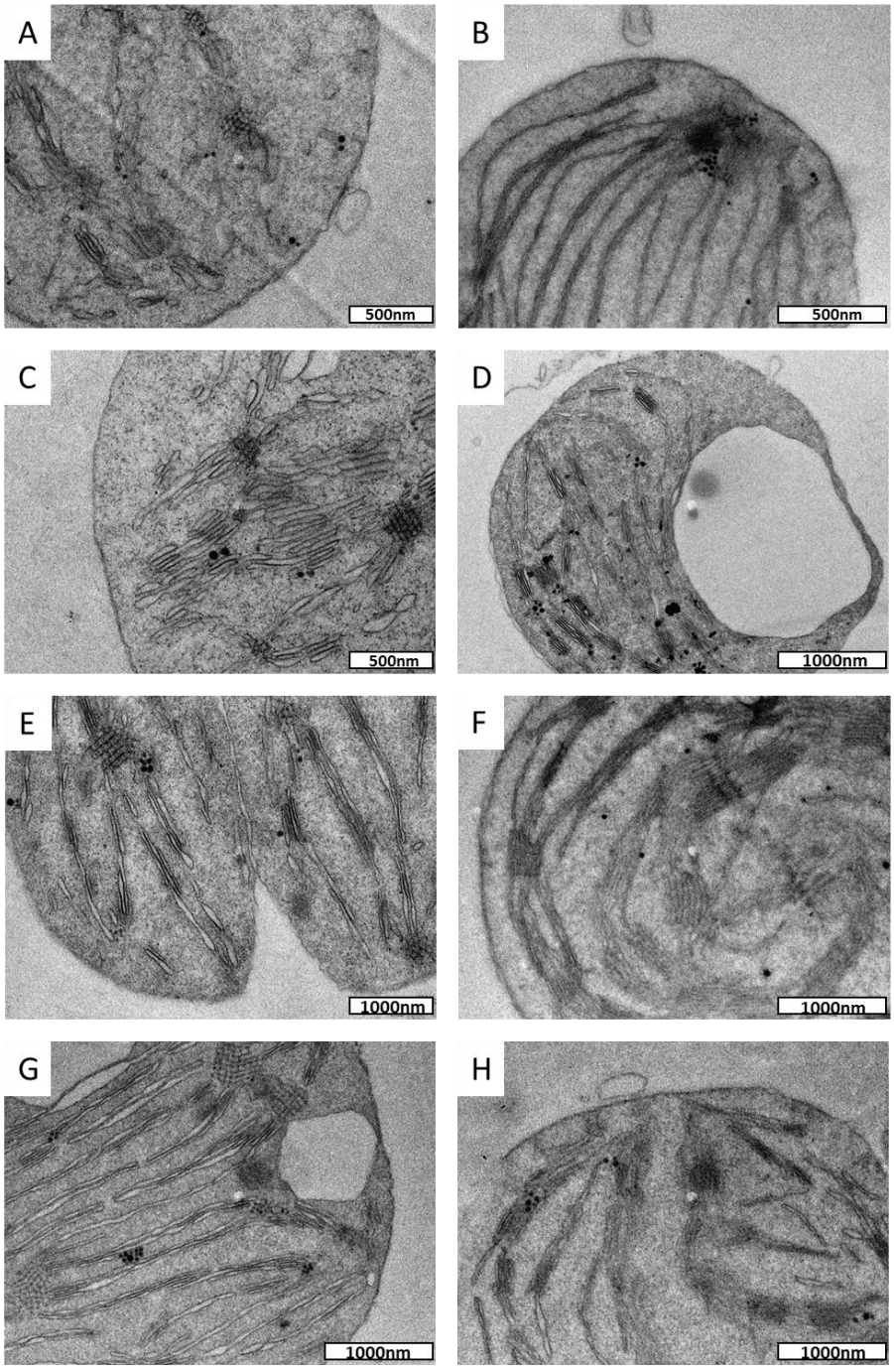

Figure 67: TEM images of post stained chloroplasts incubated with transit peptide coated GNPs, then thermolysin treated, slices 70nm in thickness. A-C. scale bar 500nm and D-H scale bar 1000nm. A. 3 nm GNPs 1% TP. B. 3 nm GNPs 5%TP. C. 3 nm GNPs CALNN. D. 3 nm GNPs CALNN-TAT. E. 3 nm GNPs PEG. F. 10 nm GNPs 5%TP. G. 10 nm GNPs CALNN-TAT. H. 10 nm GNPs PEG.

As can be seen in Figure 65, no particles were present in any sample, so it is possible that all particles could not be internalised and were removed after thermolysin treatment as seen in previous experiments.

To conclude, the import studies were promising with the transit peptide appearing to bring the GNPs into close contact with the chloroplast membrane, but import was not seen, possibly due to aggregation of the complexes. However, due to time constraints and a lack of protein these experiments could not be repeated or optimised.

6 – Conclusions and Future Work

6.1 – DCS as a Method for Analysing the EDL

To conclude, the DCS method appears to observe a regular and repeatable shrinking in ligand shell size when exposed to increasing concentrations of electrolyte. However, while qualitatively this can be assigned to the EDL and our data followed the expected trend giving size changes in the double layer that seem reasonable, quantitatively, this effect proved difficult to analyse with a multitude of variables.

Running the GNP's incubated in electrolyte, in a clean gradient (not containing electrolyte) may provide information about the electrophoretic drag or any underlying drift for the experiments; although this was tried with the initial testing and showed not interpretable results this could be done in a more robust manner.

Further experiments could provide more data however there are still too many variables that assumptions have to be made for to make this a valid method on its own. However, with information provided by other existing techniques such as, the electrophoretic drag coefficient from gel electrophoresis and capacitance measurements of the particles under these conditions using electrochemistry, further analysis of the data might be an achievable goal.

6.2.1 – DCS as a Method for Analysing Ligand Capping Densities

Although close to the noise level of the machines measurement, it can be stated with reasonable confidence that a change in size was observed with different packing densities of proteins bound to nanoparticle surfaces. This was also in agreement with our FT-IR spectra of the particles and packing densities seen in previous work. Although the actual number may have some error associated, this part of the project was a reasonable success.

Extending this to study other proteins with more complex secondary structures and more room to move would be interesting, maybe over a larger range of packing densities or using larger peptides so it is a larger change. We have already done some brief work demonstrating the ability of alpha helical peptides to maintain their structure even after heating if densely packed, using FT-IR verifying this using DCS would also be of interest.

6.2.2 – DCS as a Method for Analysing Protein Corona Formation

We demonstrated that the technique can be used to accurately follow the formation of a chemisorbed protein corona around differently capped nanoparticles. Also, with addition of protein to the density gradient, to maintain the equilibrium of the sample, the physisorbed corona can also be observed. Allowing for detailed information like K_D values and 'corona' thicknesses to be determined and more qualitative

information about the orientation of the peptide in the 'corona' to be obtained. This is information not readily obtainable using other established techniques, without more complex setups or addition of probes to the particles. Extending this method to include a second protein or differentiate the difference between a mixed layer of two proteins would be a good extension to this work and another addition to the field.

The preliminary work done with mixed OH and COOH ending PEGs could be done in a more robust manner over a larger protein concentration to more fully define the difference between the two.

6.3.1 – DCS as a Method for Analysing more Complex Protein Systems & GNP-PS1 hybrids

Due to the complex nature of the nanoparticle-photosystem hybrids created in this project, the differential centrifugal sedimentation technique could only provide qualitative information about the systems. It might be possible with better defined systems, like Nanorods to account for the change in geometry and include a non-sphericity factor. However, using this information and a variety of other techniques such as; UV-Vis spectroscopy and a range of electron microscopies, the systems were characterised further.

Preliminary work using the aforementioned systems attempted to create photo-electrodes, by coating gold slides with these hybrids. Cyclic voltammetry, conductive

AFM or similar techniques that have been used on previous systems would help to test the photoactivity of these systems.

6.3.2 – GNPs Import into Chloroplasts

Purification of the transit peptide was more difficult than originally intended with the His-Tag not functioning. Extending the His-repeat unit and performing a His-tag purification after the ammonium sulfate fractionation should provide a much purer sample. Creation of a large store of the peptide to allow for a larger and more comprehensive study of the functionalised GNPs would be desirable.

Better characterisation of GNPs after functionalisation using DCS, FT-IR (provided a large enough stock to make a peptide background measurement) and stained TEM or GFP tagged versions of the transit-peptide would allow for a more confidence in the functionalisation of the GNPs. Although initial results would suggest the particles are fully functionalised. More import studies with multiple repeats to confirm if the GNPs do in fact localise at the transport machinery would be good future work also.

6.4 – Final Conclusions

To conclude the main aim of the project was to evaluate the capabilities and limitations of differential centrifugal sedimentation for the high resolution analysis of

subtle size and mass variations in nanoparticles. This aim has been achieved by demonstrating its use in following subtle changes in the protective capping layers around nanoparticles. As well as giving information into the structure of the protein 'corona' and even the more transient physisorbed proteins.

Preliminary result showing its potential to possible characterise or be a complementary technique for characterising the thickness of GNPs EDL and possibly the type of ions contained in it. The secondary aim of preliminary work into creating photo-electrodes or internalising GNPs into chloroplasts to form a contact to the PS1 has been more mixed in its results.

References

1 R. Carpentier, *Photosynthesis Research Protocols*, 2011, vol. 684.

2 J. M. Abad, S. F. L. Mertens, M. Pita, V. M. Fernández and D. J. Schiffrin, *J. Am. Chem. Soc.*, 2005, **127**, 5689–5694.

3 Y.-J. Gu, J. Cheng, C.-C. Lin, Y. W. Lam, S. H. Cheng and W.-T. Wong, *Toxicol. Appl. Pharmacol.*, 2009, **237**, 196–204.

4 X. Huang, I. H. El-Sayed, W. Qian and M. A El-Sayed, *J. Am. Chem. Soc.*, 2006, **128**, 2115–20.

5 Ž. Krpetić, P. Nativo, I. a Prior and M. Brust, *Small*, 2011, **7**, 1982–6.

6 Ž. Krpetić, S. Saleemi, I. a Prior, V. See, R. Qureshi and M. Brust, *ACS Nano*, 2011, **5**, 5195–5201.

7 S. Pearson, W. Scarano and M. H. Stenzel, *Chem. Commun. (Camb).*, 2012, **48**, 4695–7.

8 J. Wang, L. Wu, J. Ren and X. Qu, *Small*, 2011, **8**, 259–264.

9 R. Wilson, *Chem. Soc. Rev.*, 2008, **37**, 2028.

10 T. Cedervall, I. Lynch, S. Lindman, T. Berggård, E. Thulin, H. Nilsson, K. a Dawson and S. Linse, *Proc. Natl. Acad. Sci. U. S. A.*, 2007, **104**, 2050–5.

11 M. P. Monopoli, D. Walczyk, A. Campbell, G. Elia, I. Lynch, F. B. Bombelli and K. a Dawson, *J. Am. Chem. Soc.*, 2011, **133**, 2525–34.

12 C. D. Walkey and W. C. W. Chan, *Chem. Soc. Rev.*, 2012, **41**, 2780–2799.

13 L. Treuel, M. Malissek, S. Grass, J. Diendorf, D. Mahl, W. Meyer-Zaika and M. Epple, J Nanopart Res, 2012, **14,** 1102 , DOI:10.1007/s11051-012-1102-3.

14 G. Maiorano, S. Sabella, B. Sorce, V. Brunetti, M. A. Malvindi, R. Cingolani and P. P. Pompa, *ACS Nano*, 2010, **4**, 622–627.

15 E. Mahon, A. Salvati, F. Baldelli Bombelli, I. Lynch and K. A. Dawson, *J. Control. Release*, 2012, **161**, 164–174.

16 A. Salvati, A. S. Pitek, M. P. Monopoli, K. Prapainop, F. B. Bombelli, D. R. Hristov, P. M. Kelly, C. Åberg, E. Mahon and K. A. Dawson, *Nat. Nanotechnol.*, 2013, **8**, 137–143.

17 K. Hamad-Schifferli, *Nanomedicine*, 2015, **10**, 1663–1674.

18 M. Mahmoudi, A. M. Abdelmonem, S. Behzadi, J. H. Clement, S. Dutz, M. R. Ejtehadi, R. Hartmann, K. Kantner, U. Linne, P. Maffre, S. Metzler, M. K. Moghadam, C. Pfeiffer, M. Rezaei, P. Ruiz-Lozano, V. Serpooshan, M. a Shokrgozar, G. U. Nienhaus and W. J. Parak, *ACS Nano*, 2013, **7**, 6555–62.

19 F. Wang, L. Yu, M. P. Monopoli, P. Sandin, E. Mahon, A. Salvati and K. A. Dawson, *Nanomedicine Nanotechnology, Biol. Med.*, 2013, **9**, 1159–1168.

20 T. Laaksonen, P. Ahonen, C. Johans and K. Kontturi, *ChemPhysChem*, 2006, **7**, 2143–2149.

21 G. A. Somorjai, *Langmuir*, 1991, **7**, 3176–3182.

22 E. Clementi, *J. Chem. Phys.*, 1967, **47**, 1300.

23 R. B. Grubbs, *Polym. Rev.*, 2007, **47**, 197–215.

24 P. Thoniyot, M. J. Tan, A. A. Karim, D. J. Young and X. J. Loh, *Adv. Sci.*, 2015, **2**, 1–13.

25 I. Ojea-jime and J. M. Campanera, *J. Chem. Phys. C*, 2012, **116** , 23582 - 23691

26 M. S. Strozyk, S. Carregal-Romero, M. Henriksen-Lacey, M. Brust and L. M. Liz-Marzán, *Chem. Mater.*, 2017, **29**, 2303–2313.

27 E. Pensa, E. Corte, M. H. Fonticelli, G. Benítez, A. Rubert and R. C. Salvarezza, *Acc. Chem. Res.*, 2012, **45**, 1183–1192.

28 J. A. Dean, *Lange's Handbook of chemistry*, 15th edn., 1999.

29 J. C. Love, L. A. Estroff, J. K. Kriebel, R. G. Nuzzo and G. M. Whitesides, *Self-assembled monolayers of thiolates on metals as a form of nanotechnology*, 2005, vol. 105.

30 M. Brust, J. Fink, D. Bethell, D. J. Schiffrina and C. Kielyb, *J. Chem. Soc., Chem. Commun*, 1995, 1655–1656.

31 Z. Krpetić, A. M. Davidson, M. Volk, R. Lévy, M. Brust, D. L. Cooper, Z. Krpetic and R. Levy, *ACS Nano*, 2013, **7**, 8881–8890.

32 J. Turkevich, G. Garton and P. C. Stevenson, *The Color of Colloidal Gold, 1950*.

33 J. Turkevich, P. C. Stevenson , J; Hillier, A Study of the Nucleation and Growth Processes in the Synthesi of Colloidal Gold, 1951.

34 N. G. Bastús, J. Comenge and V. Puntes, *Langmuir*, 2011, **27**, 11098–105.

35 J. Piella, N. G. Bastús and V. Puntes, *Chem. Mater.*, 2016, **28**, 1066–1075.

36 A. Taylor, K. M. Wilson, P. Murray, D. G. Fernig and R. Lévy, *Chem. Soc. Rev.*,

2012, **41**, 2707.

37 E. C. Cho, J. Xie, P. A. Wurm and Y. Xia, *Nano Lett.*, 2009, **9**, 1080–1084.

38 A. Verma and F. Stellacci, *Small*, 2010, **6**, 12–21.

39 E. Fröhlich, *Int. J. Nanomedicine*, 2012, **7**, 5577–5591.

40 B. Alberts, D. Bray, K. Hopkin, A. Johnson, J. Lewis, M. Raff, K. Roberts and P. Walter, *Essential Cell Biology*, Garland Science, Taylor & Francis Group, Fourth., 2014.

41 A. J. Bard, L. R. Faulkner, E. Swain and C. Robey, *Fundamentals and Applications*, 2000.

42 C. M. A. Brett, A. N. A. Maria and O. Brett, *Principles , Methods , and Applications*, 1994.

43 S. H. Radwan and H. M. E. Azzazy, *Expert Reviews Ltd,* 2009, **9**, 511–524.

44 R. Zsigmondy, *Kolloidchemie*, Otto Spamer, Leipzig, 2nd edn., 1918.

45 D. Maiolo, P. Bergese, E. Mahon, K. A. Dawson and M. P. Monopoli, *Anal. Chem.*, 2014, **86**, 12055–12063.

46 D. Alberghina, C. Giannetto, I. Vazzana, V. Ferrantelli and G. Piccione, *J. Vet. Diagn. Invest.*, 2011, **23**, 111–114.

47 A. Bujacz, *Acta Crystallogr. Sect. D Biol. Crystallogr.*, 2012, **68**, 1278–1289.

48 P. M. Kelly, C. Åberg, E. Polo, A. O. Connell, J. Cookman, Ž. Krpetić and K. A. Dawson, 2015, 1–73.

49 I. Lynch, A. Salvati and K. A Dawson, *Nat. Nanotechnol.*, 2009, **4**, 546–7.

50 D. Hühn, K. Kantner, C. Geidel, S. Brandholt, I. De Cock, S. J. H. Soenen, P. Riveragil, J. M. Montenegro, K. Braeckmans, K. Müllen, G. U. Nienhaus, M. Klapper and W. J. Parak, *ACS Nano*, 2013, **7**, 3253–3263.

51 C. Röcker, M. Pötzl, F. Zhang, W. J. Parak and G. U. Nienhaus, *Nat. Nanotechnol.*, 2009, **4**, 577–80.

52 S. Milani, F. Baldelli Bombelli, A. S. Pitek, K. A. Dawson and J. Rädler, *ACS Nano*, 2012, **6**, 2532–2541.

53 P. Maffre, K. Nienhaus, F. Amin, W. J. Parak and G. U. Nienhaus, *Beilstein J. Nanotechnol.*, 2011, **2**, 374–83.

54 S. Dominguez-Medina, S. McDonough, P. Swanglap, C. F. Landes and S. Link, *Langmuir*, 2012, **28**, 9131–9139.

55 D. H. Tsai, M. P. Shelton, F. W. DelRio, S. Elzey, S. Guha, M. R. Zachariah and V. A. Hackley, *Anal. Bioanal. Chem.*, 2012, **404**, 3015–3023.

56 E. Casals, T. Pfaller, A. Duschl, G. J. Oostingh and V. Puntes, *ACS Nano*, 2010, **4**, 3623–3632.

57 S. Goy-López, J. Juárez, M. Alatorre-Meda, E. Casals, V. F. Puntes, P. Taboada and V. Mosquera, *Langmuir*, 2012, **28**, 9113–9126.

58 C. Minelli, R. Garcia-diez, A. E. Sikora, C. Gollwitzer and M. Krumrey, *Surf. Interface Anal*, 2014, **46**, 663–667.

59 N. A. Belsey, A. G. Shard and C. Minelli, *Biointerphases*, 2015, **10**, 19012.

60 A. V Hill and J. Barcroft, *J. Physiol.*, 1910, **39**, 411–428.

61 A. . Hill, *Proc. Physiol. Soc, 1910.*

62 G. Limousin, J. P. Gaudet, L. Charlet, S. Szenknect, V. Barthès and M. Krimissa, *Appl. Geochemistry*, 2007, **22**, 249–275.

63 Y. G. Adewuyi, *Biog. Sulfur Environ.*, 1989, **393**, 529–559.

64 W. Haiss, N. T. K. Thanh, J. Aveyard and D. G. Fernig, *Anal. Chem*, 2007, **79**, 4215–4221.

65 W. Haiss, N. T. K. Thanh, J. Aveyard and D. G. Fernig, 2015, *Anal. Chem*, **79**, 4215–4221.

66 P. A. Annis, J. H. Campbell, A. Matsukura, A. Senentz and A. D. King, *Color. Technol.*, 2007, **123**, 242–247.

67 A. L. Lucius, P. K. Veronese and R. P. Stafford, *Methods Mol. Biol.*, 2012, **796**, 175–86.

68 O. Clay, N. Carels, C. J. Douady, G. Bernardi, Laidlaw and M. Steinmetz, *Analytical Ultracentrifugation: Techniques and Methods*, RCS Publishing, 2005.

69 L. M. Lassen, S. K. Jørgensen and K. Nørgaard, 1871, 161–177.

70 United States Patent Office, 3,475,968, 1969.

71 United States Patent Office, 4,699,015, 1987.

72 United States Patent Office, 5,786,898, 1998.

73 J. L. R. Arrondo, A. Muga, J. Castresana and F. M. Goni, 1993, **59**, 23–56.

74 C. P. Shaw, D. A. Middleton, M. Volk and R. Lévy, *ACS Nano*, 2012, **6**, 1416–1426.

75 C. Krejtschi and K. Hauser, *Eur. Biophys. J.*, 2011, **40**, 673–85.

76 Y. Chirgadz and E. Bradzhnik, *Biopolymers*, 1973, **12**, 2185–2188.

77 E. Colangelo, Q. Chen, A. M. Davidson, D. Paramelle, M. B. Sullivan, M. Volk and R. Levy, *Langmuir*, 2017, **33**, 438–449.

78 L. de Broglie, *Found. Phys.*, 1970, **1**, 5–15.

79 R. E. Blankenship, *Photosynth. Res.*, 1992, **33**, 91–111.

80 A. Amunts, O. Drory and N. Nelson, *Nature*, 2007, **447**, 58–63.

81 S. G. Boxer, *Annu. Rev. Biophys. Biophys. Chem.*, 1990, **19**, 267–99.

82 I. Carmeli, M. Mangold, L. Frolov, B. Zebli, C. Carmeli, S. Richter and a. W. Holleitner, *Adv. Mater.*, 2007, **19**, 3901–3905.

83 L. Frolov, O. Wilner, C. Carmeli and I. Carmeli, *Adv. Mater.*, 2008, **20**, 263–266.

84 A. Aimable and P. Bowen, *Process. Appli. of Ceramics*, 2010, **4**, 157–166.

85 T. T. Ahner, F. Delissen and S. Sokolov, *J. Am. Chem. Soc*, 2010, **132**, 1296–1301.

86 P. N. Ciesielski, C. J. Faulkner, M. T. Irwin, J. M. Gregory, N. H. Tolk, D. E. Cliffel and G. K. Jennings, *Adv. Funct. Mater.*, 2010, **20**, 4048–4054.

87 P. N. Ciesielski, D. E. Cliffel and G. K. Jennings, *J. Phys. Chem. A*, 2011, 3326–3334.

88 J. D. J. Olmos and J. Kargul, *Acta Soc. Bot. Pol.*, 2014, **83**, 423–440.

89 G. LeBlanc, E. Gizzie, S. Yang, D. E. Cliffel and G. K. Jennings, *Langmuir*, 2014, **30**, 10990–11001.

90 G. LeBlanc, G. Chen, E. A Gizzie, G. K. Jennings and D. E. Cliffel, *Adv. Mater.*, 2012, **24**, 5959–62.

91 D. Yu, M. Wang, G. Zhu, B. Ge, S. Liu and F. Huang, *Sci. Rep.*, 2015, **5**, 9375.

92 N. Sekar and R. P. Ramasamy, *J. Photochem. Photobiol. C Photochem. Rev.*, 2014, **22**, 19–33.

93 N. Wangoo, K. K. Bhasin, R. Boro and C. R. Suri, *Anal. Chim. Acta*, 2008, **610**, 142–8.

94 a. Grimm, C. Nowak, J. Hoffmann and W. Schärtl, *Macromolecules*, 2009, **42**, 6231–6238.

95 S. S. Shankar, A. Ahmad, R. Pasricha and M. Sastry, *J. Mater. Chem.*, 2003, **13**, 1822.

96 E. Onelli, C. Prescianotto-Baschong, M. Caccianiga and A. Moscatelli, *J. Exp. Bot.*, 2008, **59**, 3051–3068.

97 J. L. Gardea-Torresdey, J. G. Parsons, E. Gomez, J. Peralta-Videa, H. E. Troiani, P. Santiago and M. J. Yacaman, *Nano Lett.*, 2002, **2**, 397–401.

98 D. Bagal-Kestwal, R. M. Kestwal and B.-H. Chiang, *J. Nanobiotechnology*,

2015, **13**, 30.

99 P. Jarvis and J. Soll, *Biochim. Biophys. Acta - Mol. Cell Res.*, 2001, **1541**, 64–79.

100 J. P. Danehy and K. N. Parameswaran, *J. Chem. Eng. Data*, 1968, **13**, 386–389.

101 A. M. Davidson, M. Brust, D. L. Cooper and M. Volk, *Anal. Chem.*, 2017, **89**, 6807–6814.

102 K. Bohinc, V. Kralj-iglic and Aleš Iglič, *Electrochimica Acta*, 2001, **46**, 3033–3040.

103 D. C. Henry, *Proc. R. Soc. A Math. Phys. Eng. Sci.*, 1931, **133**, 106–129.

104 G. H. Kelsall, S. Tang, S. Yurdakult and A. L. Smith, 1996, **92**, 3887–3893.

105 R. W. O'Brien and L. R. White, *J. Chem. Soc. Faraday Trans. 2*, 1978, **74**, 1607.

106 H. Ohshima, *J. Colloid Interface Sci.*, 1994, **168**, 269–271.

107 H. Ohshima, T. W. Healy and L. R. White, *J. Chem. Soc. Faraday Trans. 2*, 1983, **79**, 1613.

108 J. W. Swan and E. M. Furst, *J. Colloid Interface Sci.*, 2012, **388**, 92–4.

109 F. Strubbe, F. Beunis, T. Brans, M. Karvar, W. Woestenborghs and K. Neyts, *Phys. Rev. X*, 2013, **3**, 21001.

110 L. Duchesne, D. Gentili, M. Comes-Franchini and D. G. Fernig, *Langmuir*, 2008, **24**, 13572–80.

111 P. M. Donaldson and P. Hamm, 2013, 634–638.

112 D. Walczyk, F. B. Bombelli, M. P. Monopoli, I. Lynch and K. A. Dawson, J. Am.

Chem. Soc, 2010, **132**, 5761–5768.

113 M. Ammam, *RSC Adv.*, 2012, **2**, 7633.

114 M. Cui, R. Liu, Z. Deng, G. Ge, Y. Liu and L. Xie, *Nano Res.*, 2014, **7**, 345–352.

115 H. Xu, J. L. Kaar, A. J. Russell and W. R. Wagner, *Biomaterials*, 2006, **27**, 3125–3135.

116 B. Pelaz, P. Maffre, R. Hartmann, M. Gallego, J. M. De Fuente, G. U. Nienhaus, W. J. Parak and S. Rivera-ferna, *ACS Nano*, 2015, **9**, 6996–7008.

117 T. Peters, *Adv. Protein Chem.*, 1985, **35**, 167–245.

118 A. Michnik, K. Michalik and Z. Drzazga, *J. Thermal. Anal. Calorimetry*, 2005, **80**, 399–406.

119 L. R. S. Barbosa, M. G. Ortore, F. Spinozzi, P. Mariani and S. Bernstorff, *Biophys. j.* , 2010, **98**, 147–157.

120 C. de Roe, P. J. Courtoy and P. Baudhuin, *J. Histochem. Cytochem.*, 1987, **35**, 1191–1198.

121 C. C. Fleischer and C. K. Payne, *Acc. Chem. Res.*, 2014, **47**, 2651–2659.

122 S. Chakraborty, P. Joshi, V. Shanker, Z. A. Ansari, S. P. Singh and P. Chakrabarti, *Langmuir*, 2011, **27**, 7722–7731.

123 S. H. Brewer, W. R. Glomm, M. C. Johnson, M. K. Knag, S. Franzen and D. L. M. *Gold*, 2005, **62**, 9303–9307.

124 L. Frolov, Y. Rosenwaks, S. Richter, C. Carmeli and I. Carmeli, *J. Phys. Chem. C*, 2008, **112**, 13426–13430.

125 J. Nield, P. J. Rizkallah, J. Barber and N. E. Chayen, *J. Struct. Biol.*, 2003, **141**, 149–155.

126 A. Z. Nielsen, B. Ziersen, K. Jensen, L. M. Lassen, C. E. Olsen, B. L. Møller and P. E. Jensen, *ACS Synth. Biol.*, 2013, **2**, 308–315.

127 E. Lam, W. Ortiz and R. Malkin, *FEBS Lett.*, 1984, **168**, 10–14.

Appendix

Appendix 1 – List of Figures

Figure 1: Schematic of aggregation of atoms into bulk material to limit the number of high energy surface atoms[22]. 15

Figure 2: Schematic of the three forms of nanoparticle stabilisation: A Encapsulation stabilisation, B Steric/Ligand stabilisation, C Charge stabilisation. 17

Figure 3: Schematic of citrate stabilisation of gold nanoparticle. 18

Figure 4: Approximate gold reduction equation[34]. 19

Figure 5: Comparison of the double layer mathematical models with the experimental data (taken from Electrochemistry Principles, Methods and Applications by Brett.C.M.A & Brett.A.M pages 43-51)[42] 22

Figure 6: Schematic of Electrochemical Double Layer formation on a gold nanoparticle surface[20] 23

Figure 7: Electrophoretic effect[41] 24

Figure 8: Structure of Bovine Serum Albumin (created fromDOI: 10.2210/pdb4f5s/pdb, 4F5S PDB file using VMD software) with approximate measurements taken from the structure[47] 26

Figure 9: Schematic of corona formation in complex biological media. The biological medium is hypothesised to bind to GNPs in a random array of various proteins competing for adsorption sites[10,48,49]. 27

Figure 10:Schematic of surface plasmon's interaction of metal nanoparticle with an electromagnetic field.[43] 29
Figure 11: A representative spectra of citrate stabilised gold nanoparticles with an inset image of the sample (spectrum has been cropped to show the relevant data). The peak in the image being the SPR band in absorbance. 30
Figure 12: A representative UV-Vis spectrum showing the comparison of gold nanoparticles stabilised with citrate or with a short chain PEG OH (the PEG OH has 11 carbon units and 4 ethyl units, the spectrum has been cropped to show the relevant data). A clear shift can be seen with the two different capping ligands. 32
Figure 13: Image of the CPS machine. 34
Figure 14: Schematic of the CPS machine's internal structure[70–72]. 37
Figure 15: Schematic of particle separation and readout over time. 39
Figure 16: Example of different particle measurements and the shift values due to assumed density..... 42
Figure 17: Schematic of the recalculation of data to provide actual size of the functionalised GNP and its core size (values shown are approximate). 44
Figure 18: Schematic of protein structuring hierachy[40]..... 46
Figure 19: Schematic of the amide 1 band and the stretches and bends that contribute..... 47
Figure 20: Chloroplast image comparison for light vs electron microscopy. 52
Figure 21: Diagram showing the breakdown of plant cells, to chloroplasts and then the photosythetic apparatus. The Photosynthetic apparatus from left to right is; Photosystem 2 (PSII), Plasto-Quinone (PQ), Cytochrome b6-F complex (Cyt B6F),

Plastocyanin (PC), Photosystem 1 (PSI), Ferrodoxin (Fd), Ferrodoxin NADP redtuctase (FNR) and ATP synthase. 54
Figure 22: Electron energy diagram for the photosynthetic apparatus. Adapted from R. E. Blankenship 1992[79]. 55
Figure 23:Image showing the TIC TOC mechanism in detail adapted from Image taken from, Toc, Tic, and chloroplast protein import by P.Jarvis, Et.al. 2001[99]. 57
Figure 24: Ligands used in EDL experiments and the approximate pKa and pI[100]..... 98
Figure 25: Raw DCS results showing the shift of the initial particle tests when introduced into solutions with increasing concentration of electrolytes. 100
Figure 26: Graph showing the shift in size seen by the DCS measurements with increasing electrolyte concentration for both CALNN and PEG OH coated GNPs. All points are the average of at least three runs of the same experiment..... 101
Figure 27: Graph showing the shift in ligand shell thickness with increasing electrolyte concentration. All points are the average of at least three runs of the same experiment. 102
Figure 28: Henry plot of the change in ligand shell thickness. The black trend line aligns with all data points and the red trend line aligns with for the first 4 data points and excludes the two outlying data points at higher electrolyte concentrations. 106
Figure 29: Graph showing the shift in ligand shell thickness with increasing electrolyte concentration. All points are the average of at least three runs of the same experiment. 108

Figure 30: Graph showing the shift of the ligand shell thickness of PEG COOH GNPs with increasing electrolyte concentration. All points are the average of at least three runs of the same experiment. 109
Figure 31: Graphs showing the change in thickness for the PEG COOH particles when exposed to the different electrolyte solutions. Left, the change with lithium (red) and sodium perchlorate (black)with and right, the change with potassium (orange) and cesium chloride (green). All points are the average of at least three runs of the same experiment. 110
Figure 32: Graph showing the changes in thickness for the PEG COOH particles when exposed to different electrolyte solutions. All points are the average of at least three runs of the same experiment. 111
Figure 33: Graph showing the changes in thickness for the PEG COOH particles when exposed to the different electrolyte solutions. All points are the average of at least three runs of the same experiment. 112
Figure 34: FT-IR spectra of the amide 1 region of the CALNN peptide incubated with GNPs at high and low concentrations. The spectra were run with a D_2O background which had the background water vapour removed. 115
Figure 35: DCS results of GNPs incubated with high and low concentrations of CALNN peptide. Inset is an enlarged cross section of the graph, to highlight the shift in size. 118
Figure 36: DCS results for Citrate GNPs incubated in various BSA concentrations. The arrow indicates the increasing BSA incubation concentration; the legend is the concentration of the incubating BSA solution in µM. 121

Figure 37: Graphs showing the effect of a change in density on the deconvoluted ligand shell thickness plotted against the reported size. Left Citrate, Right PEG COOH, Black line shows the final measurement at 500µM BSA, 1.1 g/ml(red), 1.15 g/ml (orange) and 1.2 g/ml (green). 123

Figure 38: Graph showing the growth of the protein 'corona' with increasing BSA concentration. All points are the average of at least three runs of the same experiment. 124

Figure 39: Graph showing the protein 'corona' growth over an extended range of BSA concentrations. All points are the average of at least three runs of the same experiment. 125

Figure 40: DCS results comparing a sucrose gradient and a gradient containing BSA. The graph labelled chemisorbed is a sucrose only gradient whereas the one labelled chemisorbed + physisorbed is a sucrose and BSA gradient. 127

Figure 41: Graph showing the difference in shift for the three particle types in a sucrose gradient (solid line and filled points) and sucrose/BSA gradient (dashed line and hollow points). All points are the average of at least three runs of the same experiment. 128

Figure 42: Graph plotting deconvoluted layer thickness (nm) against incubation time (s). 130

Figure 43: Top graph shows the absorption isotherm of the separate chemisorbed and physisorbed layers, as well as them combined; the Hill model fits are presented as dashed lines. In the bottom graph the absorption isotherm of the chemisorbed and physisorbed layers as well as them both combined are shown, this time for PEG

COOH GNPs. In both graphs all points are the average of at least three runs of the same experiment. 134
Figure 44: The structure of BSA. The yellow sphere is enlarged to highlighted to indicate the presence of the surface available cysteine. 138
Figure 45: UV-Vis data showing the shift in Citrate GNPs SPR with increasing BSA concentration (µM 139
Figure 46: Cartoon of the hypothesised 'corona' formation around two different GNPs, Citrate on the right and PEG COOH on the left; both the chemisorbed (black dashed circle) and the physisorbed layer (red dashed circle) are included. 140
Figure 47: A. PS1 protein structure (image made in pymol, using PDB structural data 1JBO); B. Close-up of mutation site B; C. Close- up of mutation site C. Mutation C is highlight and circled in yellow in all images; mutation B is highlighted and circled in all images in purple[125]. 143
Figure 48: PS1 mutants appear to shift the SPR frequency of GNPs and hence, appear to bind. UV-Vis spectra comparing the initial GNP and PS1 binding experiments. Inset shows an enlarged y-axis cross section, showing the SPR band shift..... 145
Figure 49: Mixtures of GNP and mutated PS1 appear to precipitate over time and decrease the SPR absorbance of the sample. UV-Vis spectra showing a drop in absorbance of SPR and PS1 absorbance bands[127] as the system precipitates. Inset shows the sample when this precipitation has occurred and the precipitated layer and how the colour is retained. The system shown in the inset figure is GNP + PS1 B. 146

Figure 50: A UV-Vis graph comparing GNP + PS1 BC: the initial (black) spectra of the mixture; the eluent (blue) of the sample decanted of the precipitation; the eluent when added back to the sample and resdispersed (red) using sonication. Spike at ~730nm is a defect in the spectra. 147
Figure 51: A UV-Vis graph showing that after β-DM was added to the mixes the spectra no longer demonstrates a decrease in SPR absorbance. 149
Figure 52: Shown are the DCS measurements of the various GNP + PS1 systems with added beta-DM surfactant. 150
Figure 53: TEM images are shown of systems on holey carbon grid. A. Scale bar 200nm, post-stained photosystem 1. B. Scale bar 200nm, GNPs and PS1 with no post staining. C. Scale bar 200nm, post-stained GNPs and PS1 systems. D.Cryo-TEM on holey carbon grids of the same system Scale bar 100nm. 152
Figure 54: SEM images of citrate particles on gold slide. A. Scale bar 1µm, particles with no extra citrate addition. B. Scale bar 1µm, particles with extra citrate addition. 154
Figure 55: SEM images of citrate particles coated gold slide before and after incubation with PS1. A. Scale bar 1µm, slide before PS1 incubation. B. Scale bar 1µm, slide after PS1 incubation. 155
Figure 56: Ladder labels in relevant area are given in base pairs (bp). Image of agarose gel showing bands at approximately 200bp which confirms the presence of our transit peptide insert. (N.B. images were scanned from the lab book so sometimes the tape is present). 158
Figure 57: SDS-PAGE gel showing the protein fractions in the cell debris with each sample labelled above the gel. The faint bands where the transit peptide is present

are circled in the image. The last relevant band is labelled (10kDa) with the ladder being in kilo-daltons (kDa). 159
Figure 58: A SDS-PAGE of samples taken from the E.Coli culture at multiple time points after IPTG addition, the supernatant was run after redispersal in Bug Buster ® . The last relevant band from the DNA ladder is labelled (10kDa). 160
Figure 59: SDS-PAGE gel of the pellet (including the resuspended pellet) and the supernatant before purification, flow through, final wash and various fractions that had high O.D. values. The last relevant band on the DNA ladder is labelled (10kDa). 163
Figure 60: Western blot of the previous SDS-PAGE gel incubated with the anti-His antibody then visualised. Any his-tagged peptides present in the sample should appear very brightly (The bands in red are proteins that are over exposed)..... 164
Figure 61: Light Microscope image of intact chloroplast sample. 166
Figure 62: TEM images of post stained Chloroplasts slices 70 nm in thickness. A. scale bar 2000nm, shows a full slice of a chloroplast with other partial chloroplasts. B-D. are further magnifications of part of the same chloroplast. 168
Figure 63: TEM images of post stained chloroplasts incubated with citrate GNPs, slices 70nm in thickness. A. scale bar 5000nm, showing chloroplasts and a patch of nanoparticles. B. scale bar 2000nm, similar subject but further magnification. C-D. close-up of nanoparticle patches. 169
Figure 64: TEM images of post stained (1 minute) chloroplasts incubated with transit peptide coated GNPs, slices 70nm in thickness. A. scale bar 2000nm, showing chloroplasts with nanoparticles near and on the membrane. B. scale bar 1000nm,

similar subject but higher magnification. C-D. close-up of nanoparticle patches seen on the chloroplast membranes. 169
Figure 65: Thermolysin treatment appears to remove the GNP from the chloroplasts indicating that the GNPs are bound to the chloroplast membrane by the transit peptide. TEM images of post stained (1 minute) chloroplasts incubated with transit peptide coated GNPs, then thermolysin treated, slices 70nm in thickness, scale bar 2000nm in both. 171
Figure 66: UV-Vis spectra showing shifts for the different capping ligands used. On the left are the 3 nm GNP samples and on the right, are the 10 nm samples. Peaks were normalised 172
Figure 67: TEM images of post stained chloroplasts incubated with transit peptide coated GNPs, then thermolysin treated, slices 70nm in thickness. A-C. scale bar 500nm and D-H scale bar 1000nm. A. 3 nm GNPs 1% TP. B. 3 nm GNPs 5%TP. C. 3 nm GNPs CALNN. D. 3 nm GNPs CALNN-TAT. E. 3 nm GNPs PEG. F. 10 nm GNPs 5%TP. G. 10 nm GNPs CALNN-TAT. H. 10 nm GNPs PEG. 173

Appendix 2 – List of Equations

Equation 1: Coulomb's Law[41,42]..... 21

Equation 2: Debye length related to ionic strength formula[42,43]..... 23

Equation 3: Hill equation for modelling the dependence of N on [P][51,60–62] 28

Equation 4: Haiss formula for approximate diameter of particles from absorbance values.[64,65] 31

Equation 5: The Beer-Lambert law[66]..... 32

Equation 6: Condition for sedimentation stability..... 36

Equation 7: Stokes - Einstein equation arranged to solve for diameter[31,70–72]. 39

Equation 8: Geometric splitting of particle density into core and ligand density. 43

Equation 9: Maximum resolution of light microscopes depend on the wavelength of the photons used. 50

Equation 10: The de Broglie wavelength relationship between the wavelength of an electron and the kinetic energy of the same electron[78]..... 51

Equation 11: Formula relating momentum of particle to electric field/force applied[103]..... 104

Equation 12: Formula for calculating the electrophoretic mobility of a particle[103].105

Equation 13:A simple approximation of Henry's function[103]..... 105

Equation 14: Effective density component modified to include protein corona. ... 122

Appendix 3 – List of Tables

Table 1: Comparison of IR frequencies in different solvents. () are band descriptors, s is strong, w is weak, m is medium and br is broad[76]. 49

Table 2: Sucrose Gradient Injection Steps 71

Table 3: Table of control experiments, demonstrating the minimal deviation of the results before and after cleaning and therefore the rapid removal of physisorbed protein and the strength of the chemisorbed. PEG OH results not shown due negligible change. 132

Table 4: DLS results showing the shift of GNPs incubated in BSA with no cleaning. 137